FERRITE BASED NANOCOMPOSITES FOR SUPERCAPACITANCE APPLICATION

Dr. S. R. Gibin

Ferrite Based Nanocomposites for Supercapacitance Application

Dr. S. R. Gibin

Cape Comorin Publisher
Kanyakumari, Tamilnadu, India

TITLE : Ferrite Based Nanocomposites for Supercapacitance Application

ISBN : 978-93-88761-57-4

Author : Dr. S. R. Gibin

Price : 175/- INR

Published by : Cape Comorin Publisher
Kanyakumari, Tamilnadu, India

Website : www. Capecomorinpublisher.com

©. Cape Comorin Publisher, All rights Reserved 2020.

No part of this publication may be reproduced or transmitted in any form or by any means, electronic or mechanical, including photocopying, recording, or any other information storage and retrieved without prior permission in writing from the publishers.

Concerned author is solely responsible for his views, opinions, policies, copyright infringement, legal action, penalty or loss of any kind regarding his works.

CONTENTS

CHAPTER	TITLE	PAGE
	PREFACE	i-v
	LIST OF FIGURES	vi-xi
	LIST OF TABLES	xii
	LIST OF GRAPHS	xiii
	LIST OF SYMBOLS	xiv-xv
	LIST OF ABBREVIATIONS	xvi
I	INTRODUCTION	1
	1.1 INTRODUCTION OF NANOSCIENCE AND NANOMATERIALS	1
	1.2 METHODS INVOLVING IN PREPARATION OF NANOMATERIALS	2-3

CHAPTER	TITLE	PAGE
	1.3 MECHANISM OF GROWTH	3
	1.4 NANOSCIENCE AS A DRIVING FORCE FOR NANOTECHNOLOGY	4-5
	1.5. COMPOSITE NANOMATERIALS	5-6
	1.6 INTRODUCTION OF FERRITES	6
	1.7 NANO FERRITES	6-10
	1.8 INTRODUCTION OF NICKEL NANOPARTICLES	10
	1.9 INTRODUCTION OF COBALT NANOPARTICLES	10
	1.10 INTRODUCTION OF NICKEL FERRITES ($NiFe_2O_4$) NANO COMPOSITE	11
	1.11 INTRODUCTION OF COBALT FERRITES ($CoFe_2O_4$)	11-12
	1.12 INTRODUCTION OF NICKEL COBALT FERRITES ($Ni_{1-x}Co_xFe_2O_4$)	12

CHAPTER	TITLE	PAGE
	1.13 INTRODUCTION TO SUPERCAPACITOR	12-13
	1.14 SUPERCAPACITOR USED AS POWER SOURCES	13-15
	1.15 ELECTROCHEMICAL CAPACITOR	15-16
	1.16 HYBRID CAPACITOR	17
	1.17 APPLICATIONS OF SUPER CAPACITORS	17
	1.18 AIM AND SCOPE OF THE PRESENT WORK	17
II	REVIEW OF LITERATURE	18-37
III	MATERIALS AND METHODS	38-55
	3.1. CCHEMICALS	38
	3.2. SYNTHESIS of $NiFe_2O_4$ NANOPARTICLES	38
	3.3. SYNTHESIS of $CoFe_2O_4$ NANOPARTICLES	38-39
	3.4. SYNTHESIS of $Ni_{1-x}Co_xFe_2O_4$ NANOPARTICLES	39

CHAPTER	TITLE	PAGE
	3.5. MATERIALS CHARACTERIZATION	39
	3.5.1. *Thermo gravimetric Analysis (TGA)*	39
	3.5.1a. *Working Principle*	40
	3.5.1b *Instrumentation*	40
	3.5.1c *Analysis of TGA curve*	41
	3.5.2. *Differential Thermal Analysis (DTA)*	41
	3.5.2a. *Working Principle*	41-42
	3.5.2b. *Instrumentation*	42-44
	3.5.2d. *Instrument details*	44
	3.5.3. *Fourier Transform Infrared Spectroscopy (FTIR)*	44

CHAPTER	TITLE	PAGE
	3.5.3a. *Working Principle*	44
	3.5.3b. *Working*	45
	3.5.3c. *Recording of FTIR Spectra*	45
	3.5.3d. *Instrument Details*	46
	3.5.4. *X-Ray Diffraction (XRD)*	46-47
	3.5.4a. *Sample Preparation*	47
	3.5.4b. *Instrument Details*	47
	3.5.5. *Scanning Electron Microscope (SEM)*	47-49
	3.5.5a. *Energy-dispersive X-ray spectroscopy*	49-50
	3.5.5b. *Sample Preparation*	50
	3.5.5c. *Instrument Details*	50

CHAPTER	TITLE	PAGE
	3.5.6. *Field Emission-Transmission Electron Microscope (FETEM)*	50-51
	3.5.6a. *Sample Preparation*	51
	3.5.6b. *Instrument details*	52
	3.5.7. *Cyclic Voltammetry*	52-53
	3.5.7a. *Electrochemical performance investigation*	53
	3.5.7b. *Instrument details*	53
	3.5.8. *X-ray Photoelectron Spectroscopy (XPS)*	53-55
	3.5.8a. *Sample Preparation*	55
	3.5.8b.*Instrument Details*	55

CHAPTER	TITLE	PAGE
IV	**PREPARATION AND CHARACTERIZATION OF NICKEL FERRITE NANO PARTICLES BY CO-PRECIPITATION METHOD WITH CITRATE AS CHELATING AGENT**	56-69
	4.1. INTRODUCTION	56
	4.2. RESULTS AND DISCUSSION	57
	4.2.1. *Thermo gravimetric and differential Thermal analysis*	57-58
	4.2.2. *Functional Group Analysis*	58-59
	4.2.3. *Structural Analysis*	59-60
	4.2.4. *Field Emission Scanning Electron Microscope (FESEM) with EDAX*	61-62
	4.2.5: *Field Emission Transmission Electron Microscope (FETEM) with SAED*	62-63

CHAPTER	TITLE	PAGE
	4.2.6: Cyclic Voltammetry (CV)	63-65
	4.2.7: *Dynamic light scattering (DLS) and Zeta Potential*	65-67
	4.2.8: *X-ray photoelectron spectroscopy (XPS)*	67-69
	4.3. Conclusion	69
V	PREPARATION AND CHARACTERIZATION OF NANOSIZED COBALT FERRITE PARTICLES BY CO-PRECIPITATION METHOD WITH CITRATE AS CHELATING AGENT	70-85
	5.1. Introduction	70
	5.2. Results and Discussion	71
	5.2.1. *Thermo gravimetric and differential thermal analysis*	71-72

CHAPTER	TITLE	PAGE
	5.2.2. *Functional group analysis*	72-73
	5.2.3. *Structural Analysis*	71-72
	5.2.4. *Field Emission Scanning Electron Microscope (FESEM) with EDAX*	74-77
	5.2.5: *Field Emission Transmission Electron Microscope (FETEM) with SAED*	77-79
	5.2.6: *Cyclic Voltammetry (CV)*	79-82
	5.2.7: *Dynamic light scattering (DLS) and Zeta Potential*	82-83
	5.2.8: X-ray photoelectron spectroscopy (XPS)	83-85
	5.3. Conclusion	85

CHAPTER	TITLE	PAGE
VI	**SYNTHESIS AND CHARACTERIZATION OF NICKEL COBALT FERRITE (NI1-XCOXFE2O4) NANO PARTICLES BY CO-PRECIPITATION METHOD WITH CITRATE AS CHELATING AGENT**	**86-106**
	6.1. INTRODUCTION	**86**
	6.2. RESULTS AND DISCUSSION	**87**
	6.2.1. Thermo gravimetric and differential thermal analysis	**87-88**
	6.2.2. Functional group analysis	**88-89**
	6.2.3. Structural analysis	**89-92**
	6.2.4. Field Emission Scanning Electron Microscope (FESEM) with EDAX	**92-95**

CHAPTER	TITLE	PAGE
	6.2.5: Field Emission Transmission Electron Microscope (FETEM) with SAED	96-97
	6.2.6: Cyclic Voltammetry (CV)	97-101
	6.2.7: Dynamic light scattering (DLS) and Zeta Potential	101-102
	6.2.8: X-ray photoelectron spectroscopy (XPS)	102-105
	6.3. CONCLUSION	105-106
VII	SUMMARY AND CONCLUSION	107-109
	FUTURE PLAN	109

PREFACE

Ferrites in the form of MFe_2O_4 (M = Ni^{2+}, Co^{2+}, Cu^{2+}, etc.) have received great attention owing to their importance to electronic industries. The emerging markets are trending for portable electronic devices, such as notebook computers and mobile phones, and their development trend of being small, light-weight, and flexible have brought about an ever rising and urgent demand for eco-friendly electrochemical energy storage and conversion systems, including batteries, fuel cells, capacitors, and supercapacitors. In these ferrite based supercapacitors include nickel ferrite, cobalt ferrite and nickel cobalt ferrite found greater attraction because of their high specific capacitance, non-toxic, eco-friendly, cheap and better stability.

The aim of the present work is to prepare and characterization of nano composites involving nickel ferrite, cobalt ferrite and nickel cobalt ferrite using co-precipitation method. The entire study of the thesis has been divided into seven chapters. The introductory chapter focuses on the nanomaterials, various approaches in synthesizing nanomaterials, ferrites and the different types of spinel ferrites.

The second chapter makes a comprehensive review of the literature regarding the nanoferrites selected for the present investigation.

The third chapter deals with the principle and instrumentation of Thermo Gravimetric Differential Analysis (TG/DTA), Fourier Transform Infrared Spectroscopy (FTIR), X-Ray Diffraction (XRD), Field Emission Scanning Electron Microscope (FESEM), Energy-dispersive X-ray spectroscopy (EDX), Field Emission Transmission Electron Microscope (FETEM), Cyclic Voltammetry (CV) and X-ray Photoelectron Spectroscopy (XPS).

The fourth chapter discusses synthesize of $NiFe_2O_4$ nano particles by co-precipitation method with citrate as chelating agent. TG/DT analysis was carried out from 35 °C to 850 °C based on this, the synthesized materials were calcinated at different temperatures such as 400 °C, 600 °C and 800 °C and further characterized by using XRD and FTIR. The $NiFe_2O_4$ nano particles calcinated at 600 °C were characterized by using FESEM with EDAX, FETEM with SAED pattern, DLS zeta Potential, CV and XPS. The formation of single phase nanosized nickel ferrite was investigated by XRD and the particle size linearly increased with the temperatures was noticed. The functional groups present in the sample is identified by using FTIR analysis. The surface morphology of $NiFe_2O_4$ studied by FESEM was cubic spinel structure and it was confirmed by FETEM. The elements identified in the $NiFe_2O_4$ nanoparticles from EDAX analysis were Fe, Ni and O. Stability of the particle was analyzed through zeta potential study. XPS analysis reveals that the synthesized compound exist in multiple oxidation state. Capacitance value of 421 Fg^{-1} was observed from CV study and it was suitable for super capacitance application.

The fifth chapter details how Cobalt ferrite ($CoFe_2O_4$) nanoparticles were produced by a facile novel co-precipitation method with citrate as chelating agent. Based on TG/DT analysis the synthesized cobalt ferrite nanoparticles were calcinated at 400 °C, 600 °C and 800 °C and characterized by using XRD and FTIR. From XRD, it confirms that $CoFe_2O_4$ nano particles belongs to spinel type lattice having space group Fd3m. The $CoFe_2O_4$ nano particles calcinated at 600 °C were further characterized by using FESEM with EDAX, FETEM with SAED pattern, XPS, DLS Zeta Potential, CV and XPS. The functional groups present in the synthesized cobalt ferrite sample are identified by using FTIR analysis. The linear relationship between particle size and calcination temperatures of $CoFe_2O_4$ nanoparticles was observed. The surface morphology of $CoFe_2O_4$ studied through FESEM and FETEM specifies that the particles are found to be crystalline, and are in cubic shape. EDAX analysis revealed the presence of Co, Fe and O. XPS analysis confirms the synthesized nanoparticles exist in multiple oxidation states. Zeta potential exposes the good stability of the prepared $CoFe_2O_4$ nanoparticles. Capacitance value 609 Fg^{-1} was observed for the scanning rate of $2mVs^{-1}$ from the CV study and concluded that it is suitable for super capacitor application.

The sixth chapter deals with the synthesis and characterization of $Ni_{1-x}Co_xFe_2O_4$ (x = 0.3, 0.5, 0.7) by co-precipitation method using citrate as chelating agent. TG/DT analysis was done for the as-prepared sample, which shows the calcination is essential for the formation of pure nickel cobalt ferrite nanoparticles. The synthesized powders were calcinated at 400 °C, 600 °C and 800 °C for three hours in air and were further characterized by using XRD and FTIR. From XRD it is confirmed that the formation of cubic spinel structure with space group Fd3m. The linear relationship in between particle size and calcination temperatures of $Ni_{1-x}Co_xFe_2O_4$ nanoparticles was observed. The $Ni_{1-x}Co_xFe_2O_4$ nano particles calcinated at 600 °C were then characterized by using FESEM with EDAX, FETEM with SAED pattern, DLS Zeta Potential, CV and XPS. The surface morphology of $Ni_{1-x}Co_xFe_2O_4$ analyzed through FESEM and FETEM specify that the particles are found to be crystalline and are in cubic shape. EDAX analysis disclosed the presence of Ni, Co, Fe and O. Zeta potential depicts the good stability of the prepared $Ni_{1-x}Co_xFe_2O_4$ nanoparticles. Higher capacitance value of 865 Fg^{-1} was observed at the scanning rate 2 mVs^{-1} for the sample calcinated at 600 °C, from the CV study it is concluded that it can be used for super capacitor application. The presence of multiple oxidation state in the synthesized $Ni_{1-x}Co_xFe_2O_4$ nano particles is confirmed by XPS analysis.

The results obtained by all the techniques are summarized in chapter seven.

LIST OF FIGURES

FIGURE NO.	TITLE	PAGE NO.
1.1	Schematic diagram of top-down and bottom-up approach	2
1.2	Graphical representation of nanomaterials dimension	4
1.3	Nanoparticles of 0D, 1D, 2D and 3D	5
1.4	Structure of spinel	7
1.5	Normal spinel	8
1.6	Inverse spinel	9
1.7	Random spinel	9
1.8	Rangone plot for various energy storage and conversion devices	13
1.9	Schematic diagram of capacitor, supercapacitor (ultracapacitor) and normal batteries	14
1.10	schematic diagram of supercapacitors	16
3.1	An instrument for TGA (NETZSCH - STA 449 F3 JUPITER)	40
3.2	Experimental set up of a DTA cell	43
3.3	FTIR-Instrument	45

FIGURE NO.	TITLE	PAGE NO.
3.4	Bragg's scattering from lattice planes with spacing "d" with the same angle of incidence and the angle of reflection	46
3.5	Schematic diagram of scanning electron microscope (SEM)	48
3.6	Schematic diagram of the EDAX phenomenon	49
3.7	Schematic diagram of transmission electron microscope (TEM)	51
3.8	Cyclic voltammetry experiment setup	52
3.9	Schematic diagram of the photoelectric effect	54
3.10	XPS instrument setup	55
4.1	TGA/DT analysis of $NiFe_2O_4$ nano particles	57
4.2	FTIR spectra of $NiFe_2O_4$ nano particles calcinated at different temperatures 400 °C,600 °C and 800 °C	58
4.3	XRD spectra of $NiFe_2O_4$ nano particles as-synthesized and calcinated at different temperatures	59
4.4	FESEM image of $NiFe_2O_4$ nano particles calcinated at 600 °C with different magnifications (a), (b) and (c) Corresponding EDAX	61

FIGURE NO.	TITLE	PAGE NO.
4.5	(a), (b) FETEM of $NiFe_2O_4$ nano particles calcinated at 600 °C with different magnification and (c) Corresponding SAED. (d) Particle size measured using image j viewer software	62
4.6	CV patterns of $NiFe_2O_4$ nano particles (a) calcinated at 600 °C and (b) Different Scan rate and their Specific Capacitance values	63, 64
4.7	(a) zeta sizer and (b) zeta potential of $NiFe_2O_4$ nano particles calcinated at 600 °C	66
4.8	XPS spectra of Fe, Ni and O for $NiFe_2O_4$ nano particles calcinated at 600 °C (a),(b) and (c)	67, 68,68
5.1	TGA/DTA analysis of $CoFe_2O_4$ nano particles	71
5.2	FTIR spectra of $CoFe_2O_4$ nano particles calcinated at different temperatures	72
5.3	XRD spectra of $CoFe_2O_4$ nano particles as-synthesized and calcinated at different temperatures	73
5.4	(a), (b) FESEM image of $CoFe_2O_4$ nano particles calcinated at 600 °C with different magnifications and (c). quantitative result (d) and (e) corresponding EDAX	75, 76

FIGURE NO.	TITLE	PAGE NO.
5.5	(a), (b) (c) and (d) FETEM of $CoFe_2O_4$ nano particles calcinated at 600 °C with different magnification (e) particle size measured using image j viewer software also (f) corresponding SAED.	77, 78
5.6	(a) CV patterns of $CoFe_2O_4$ nano particles calcinated at 600 °C for different scan rates and (b) different Scan rate and their specific capacitance values	80, 81
5.7	(b) Different Scan rate and their specific capacitance values (a) zeta sizer and (b) zeta potential of $CoFe_2O_4$ nano particles calcinated at 600 °C	82
5.8	(a), (b), (c) XPS spectra of Fe, Co and O for $CoFe_2O_4$ nano particles calcinated at 600 °C	83, 84
6.1	TG/DT analysis of $Ni_{1-x}Co_xFe_2O_4$ (x=0.5) nano particles	87
6.2	FTIR spectra of $Ni_{1-x}Co_xFe_2O_4$ (x = 0.3, 0.5, 0.7) nano particles calcinated at different temperatures 400 °C, 600 °C and 800 °C	89
6.3	XRD spectra of $Ni_{1-x}Co_xFe_2O_4$ (a),(b) and (c) (x = 0.3, 0.5 and 0.7 respectively) nano particles as-synthesized and calcinated at different temperatures	90

FIGURE NO.	TITLE	PAGE NO.
6.4	(a), (b), (c) FESEM image of $Ni_{1-x}Co_xFe_2O_4$ (x = 0.3) nano particles calcinated at 600 °C with different magnifications also (d) quantitative results and (e) Corresponding EDAX. (f), (g), (h) FESEM image of $Ni_{1-x}Co_xFe_2O_4$ (x = 0.5) nano particles calcinated at 600 °C with different magnifications also (i) quantitative results and (j) Corresponding EDAX. (k), (l), (m) FESEM image of $Ni_{1-x}Co_xFe_2O_4$ (x = 0.7) nano particles calcinated at 600 °C with different magnifications also (n) quantitative results and (o) Corresponding EDAX.	92-95
6.5	(a), (b), (c), (d) FETEM image of $Ni_{1-x}Co_xFe_2O_4$ (x = 0.5) nano particles calcinated at 600 °C with different magnifications also (e) particle size using image j viewer software and (f) Corresponding SAED pattern	96
6.6	CV pattern of $Ni_{1-x}Co_xFe_2O_4$ (a), (b) and (c) (x = 0.3, 0.5 and 0.7 respectively) nano particles calcinated at 600 °C.	98

FIGURE NO.	TITLE	PAGE NO.
6.7	The spcific capacitance of the $Ni_{1-x}Co_xFe_2O_4$ (a)-(i) (x = 0.3, 0.5 and 0.7 respectively) nano particles calcinated at 600 °C Vs different scan rate	100
6.8	Zeta sizer and Zeta potential (a),(b) of $Ni_5Co_5Fe_2O_4$ nano particles calcinated at 600 °C	102
6.9	XPS spectra of Fe, Ni, Co and O for $Ni_{1-x}Co_xFe_2O_4$ (x = 0.5) nano particles calcinated at 600 °C (a),(b),(c),(d)	103

LIST OF TABLES

Table No.	Title	Page No.
1	NANOMATERIALS DIMENSION AND NANOMATERIALS TYPES	4
2	COMPARISON OF PROPERTIES OF NORMAL BATTERIES AND ELECTROCHEMICAL CAPACITORS	14
3	COMPARISON SOME IMPORTANT CHARACTERISTIC STATE OF BATTERIES, SUPERCAPACITOR AND NORMAL CAPACITOR	15
4	MAIN ADVANTAGE AND DISADVANTAGES OF ELECTROCHEMICAL DOUBLE LAYER CAPACITOR AND PSEUDO CAPACITORS	16
5	PARTICLE SIZE AND LATTICE PARAMETER OF $NiFe_2O_4$ NANO PARTICLES	60
6	THE SPECIFIC CAPACITANCE OF THE $NiFe_2O_4$ NANO PARTICLES CALCINATED AT 600 °C Vs DIFFERENT SCAN RATES	64
7	PARTICLE SIZE AND LATTICE PARAMETER OF $CoFe_2O_4$ NANO PARTICLES	74
8	THE SPECIFIC CAPACITANCE OF THE $CoFe_2O_4$ NANO PARTICLES CALCINATED AT 600 °C FOR DIFFERENT SCAN RATES	81
9	PARTICLE SIZE AND LATTICE PARAMETER OF $Ni_{1-x}Co_xFe_2O_4$ ($x = 0.3, 0.5$ and 0.7) NANO PARTICLES CALCINATED AT DIFFERENT TEMPERATURES	91
10	THE SPECIFIC CAPACITANCE OF THE $Ni_{1-x}Co_xFe_2O_4$ ($x = 0.3, 0.5$ and 0.7 RESPECTIVELY) NANO PARTICLES CALCINATED AT 600 °C FOR DIFFERENT SCAN RATES	100

LIST OF GRAPHS

GRAPH NO.	TITLE	PAGE NO.
1	Average Particle size $NiFe_2O_4$ nanoparticles using image j viewer software from FETEM	63
2	Average Particle size $CoFe_2O_4$ nanoparticles using image j viewer software from FETEM	79
3	Average Particle size $Ni_5Co_5Fe_2O_4$ nanoparticles using image j viewer software from FETEM	97

LIST OF SYMBOLS

Ni - Nickel

Co - Cobalt

Fe - Ferrite

h - Planck’s constant

D - Diameter

θ - Diffraction angle

ν - Frequency

λ - Wavelength

β - Full width at half maximum

eV - Electron Volt

M - Molar concentration

°C - Degree Celsius

d - interplanar distance

Å - Angstrom

KBr - Potassium bromide

nm - Nanometre

A - Ampere

LIST OF SYMBOLS

F - Farad

g - Gram

V - Volt

LIST OF ABBREVIATIONS

CV – Cyclic voltammetry

DLS – Dynamic Light Scattering

EDAX – Energy dispersive X-ray analysis

FESEM – Field emission scanning electron microscope

FETEM – Field emission transmission electron microscope

SAED – Selected Area Electron Diffraction

FTIR – Fourier transform infra-red

FWHM – Full width at half maximum

JCPDS – Joint committee on powder diffraction standards

TG/DTA – Thermogravimetric / differential thermal analysis

XRD – X-ray diffraction

XPS – X-ray Photoelectron Spectroscopy

CHAPTER – I

INTRODUCTION

1.1 INTRODUCTION OF NANOSCIENCE AND NANOMATERIALS

Nanoscience research is the study of materials which disclose the remarkable properties and functionality owing to the influence of small dimension. Nanoscience majorly deals with synthesis of nanoparticles, characterization, exploration, and exploitation of nanostructured materials. These materials can be generally characterized by at least one dimension in the nanometer range. Nanomaterials are explained as materials having primary particle.

The nanoparticles are of various shapes such as spheres, rods, whiskers, or have any variety of irregular shape. The structure and properties of materials vary with the grain size of nanometer range are research areas of considerable interest over the past few decades. Revolution in materials science and engineering is taking place for discovering approaches to pattern and characterize the materials at the nanometer length scale. Development of new materials having better electrical, optical, magnetic and mechanical properties are rapidly being developed for use in information technology, bio-engineering, and energy and some environmental applications. On nanoscale, the electrical, optical and magnetic properties can differ significantly from those of the bulk counterparts.

Nanomaterials are of having size dependent properties which results unique behavior relative to the materials which are composed of larger particles. Nanomaterials can retain its size dependent properties even the primary particles get agglomerate or aggregate. Agglomerate as a group of particles which are held together because of weak force which may get break into smaller particles while processing. Aggregate has explained as a group of particles that are bound together on behave of strong forces or bonds which are not easily breakable. As per the scientific knowledge the material composed of larger size particles cannot be applied to nanomaterials and it is insufficient to predict the nature of nanomaterials. Moreover, as the particle size gets decreased the surface to volume ratio of the material gets increased. Which means nanomaterials can have high surface to volume ratios, with a large percent of total atoms present on the surface. The applications of the nanomaterials become tremendous for high surface to volume ratio.

1.2 METHODS INVOLVING IN PREPARATION OF NANOMATERIALS

The greater challenge for the researchers in preparation of nanomaterials is well-defined with size and shape. There were enormous techniques have been employed to achieve this. In general there were two approaches for the nanomaterials synthesis, one is top-down approach and other is bottom-up approach. The schematic diagram of both approaches is shown in Fig. 1.1.

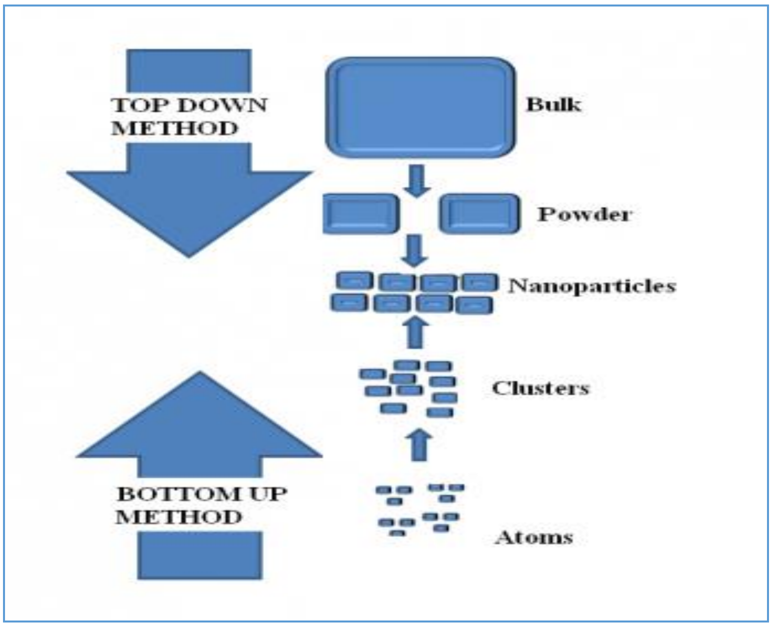

Fig. 1.1. SCHEMATIC DIAGRAM OF TOP-DOWN AND BOTTOM-UP METHOD

Attrition or milling is a typical top-down method in synthesizing nanoparticles, whereas the colloidal dispersion is typical example for bottom-up method. Top-down approach is mainly generated from the macro-scale to the nanoscale. They mostly rely on physical attributes in processing the combination of chemical, electrical or thermal treatment. Top-down approach mainly includes the methods such as milling, lithography, laser ablation, sputtering etc. On the other hand, the bottom-up approaches are generally synthesized and processed from atomic or molecular state to the nanoscale range. For which a thorough understanding is necessary regarding the individual molecular structure, their assemblies and their dynamic behavior [Palaniappan *et al.,* (2009)]. Lithography might be considered as a hybrid approach, because the growth of thin films is bottom-up however etching is top-down, although nanolithography and nano-manipulation are commonly a bottom-up approach. Both approaches play very important roles in modern era and most likely in nanotechnology as well. Sol-gel, co-precipitation, electrical deposition, self-alignment, chemical vapor deposition, atomic layer deposition etc., [Gleick, (2002)] which comes under bottom-up approach. New trend in researchers is combining both top-down and bottom-up approach for developing a new hybrid technique for innovative applications.

1.3 MECHANISM OF GROWTH

Nucleation generally occurs over sometime with constant monomer concentration. Ultimately the surface growth of clusters initiates to occur which depletes the monomer supply. The nucleation will end when the monomer concentration falls below the critical level of nucleation. A greater understating regarding the growth process of nanocrystal is essential. Since the greater surface to volume ratio in nanoparticles, it is observed that surface extra energy becomes more important in very small particles, constituting a non-negligible percentage of the total energy. Therefore for a solution which is initially not in thermodynamic equilibrium, a mechanism that allows the formation of large particles at the cost of smaller particles reduces the surface energy and hence plays a vital role in the formation of nanocrystals. Ostwald ripening process is the coarsening effect controlled by either mass transport or diffusion. In which diffusion limited Ostwald ripening process is the most predominant growth mechanism [Lifshitz *et al*., 1961; Wagner *et al*., 1961].

Normally the diffusion process will dominate the surface energy of the nanoparticles. Another driving force in formation is interfacial energy which is the energy associated with an interface due to differences between the chemical potential of atoms in an interfacial region and atoms in neighboring bulk phases. For a solid species existing at a solid-liquid interface, the chemical potential of a particle increases with decreasing particle size whereas the equilibrium solute concentration for a small particle is much larger than for a large particle, as defined by the Gibbs-Thompson equation [Jackson *et al*., 1990]. The subsequent concentration gradients prime to the transport of the solute from the smaller particles into larger particles. The equilibrium concentration of the nanocrystal in the liquid phase is reliant on the local curvature of the solid phase. Alterations in the local equilibrium concentrations, due to variations in curvature, set up concentration gradients and provide the driving force for the growth of larger particles at the expense of smaller particles (Sugimoto, 1987; Rao *et al*., 2007).

1.4 NANOSCIENCE AS A DRIVING FORCE FOR NANOTECHNOLOGY

The word nano becomes common in between researchers for exploring new materials having size in the range between 1-100 nm at least in one dimension. One nanometer (nm) is one billionth of a meter, or 10^{-9}m. One nanometer is approximately the length corresponding to 10 hydrogen or 5 silicon atoms aligned in a line. In nanoscale range the nanomaterials will exhibit different physical and chemical properties when compared to its bulk nature this is due to its specific particle size. For example the quantum dots which are of size 5-10nm will exhibit different colours while altering its size. The nanomaterials are categorized according to their dimensions as shown in Table 1 and Fig.1.2.

Table 1: Nanomaterial Dimension and Nanomaterial Types

Nanomaterial Dimension	Nanomaterial Type
All the 3 dimensions < 100 nm	Nanoshells, nanorings, microcapsules
Two dimensions < 100 nm	Nanotubes, fibres, nanowires
One dimension< 100 nm	Thin films, layers and coatings
Zero dimension 2-10 nm	Quantum dots

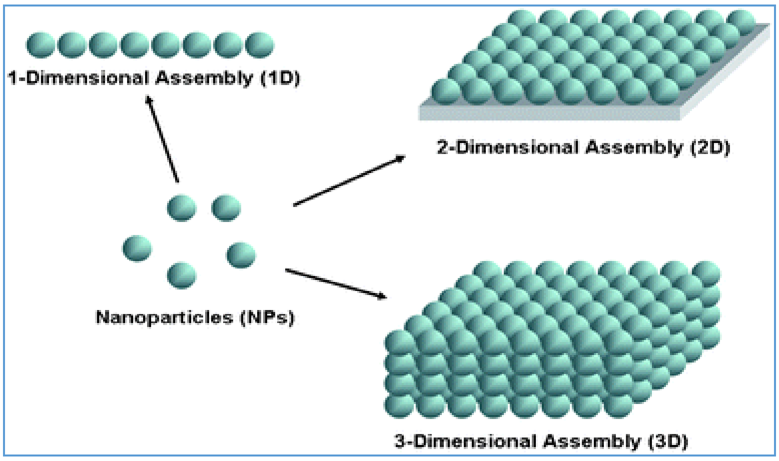
1-Dimensional Assembly (1D)
2-Dimensional Assembly (2D)
Nanoparticles (NPs)
3-Dimensional Assembly (3D)

Fig. 1.2. GRAPHICAL REPRESENTATION OF NANOMATERIAL DIMENSION

Zero dimensional (0-D) nanomaterials have nano-dimensions in all the three directions. The metallic nanoparticles including gold and silver nanoparticles and semiconductor such as quantam dots are the perfect example of this kind [Wang *et al.,* (2008)]. Most of these 0-D nanoparticles are spherical in size and the diameter of these particles will be within the range of 2-10 nm. The term "cluster" used to designate small nanoparticles with sizes less than 1 nm which comes under 0-D nanoparticles. Clusters have sizes of less than 1nm, and spherical form and have particular applicability in the field of semiconductors, catalysis, capacitance and electro-catalysis [Gleiter, (1995)].

One dimension (1-D) of the nanostructure is of outside the nanometer range in length wise. These include nanowires, nanorods, and nanotubes [Geim, (2009)]. These materials are of several micrometers in length and its diameter of only a few nanometers. Nanowire and nanotubes of metaloxides and other materials are few examples of this one dimension material. Two dimensions (2-D) are nanomaterials are of outside the nanometer range. It includes different kind of nano film such as coatings and thin-film-multilayers, nano sheets or nano-walls. In which the area of the nano films can be large i.e., several square micrometer whereas the thickness is always in nano scale range. In three dimensions (3-D) nanomaterial all dimensions of these are outside the nano meter range. These include bulk materials composed of the individual blocks which are in the nanometer scale (1-100 nm)[Khan *et al*., (2012)] and nanodandelion [Chen *et al*., (2010)]. The schematic diagram of clusters, 1D, 2D and 3D is shown in Fig. 3 below.

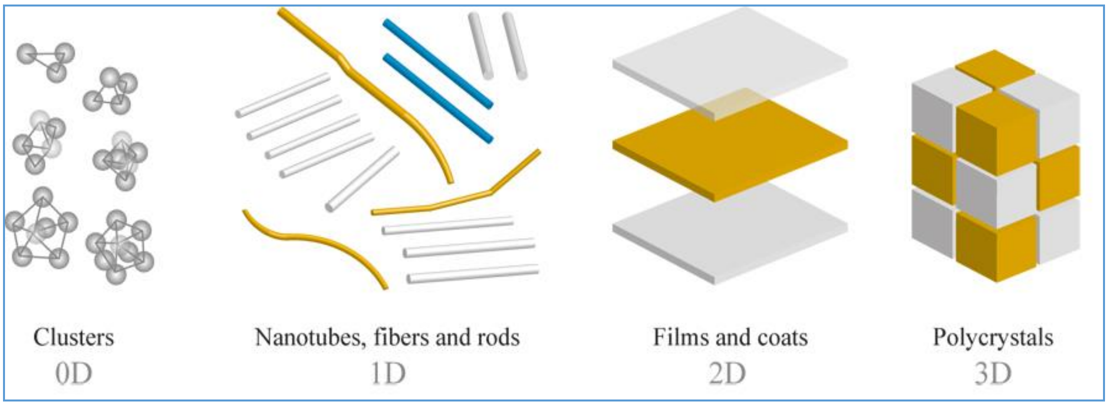

Fig. 1.3. NANOPARTICLE OF 0D, 1D, 2D AND 3D

1.5. COMPOSITE NANOMATERIALS

Nanocomposite is a multiphase solid material in which one of the phases has one, two or three dimensions of <100 nanometers (nm), or structures having nano-scale repeat distances between the different phases that make up the material. In a nutshell this means which can include porous media, colloids, gels and copolymers, but is more usually taken to mean the solid combination of a bulk matrix and nano-dimensional phases differing in properties due to variation in structure. Compartmentalization of different nanoparticles which allow multiple components to be combined within one particle by providing suitable environments for each and every individual component [Janczak and Aspinwall, (2012)]. The mechanical, electrical, thermal, optical, electrochemical, catalytic properties of the nanocomposite will vary distinctly from that of the component materials [Novoselova, (2012)]. Preparing ferrite based nanocomposite is greater task for attaining numerous applications.

1.6 INTRODUCTION OF FERRITES

Ferrites are magnetic materials which have combined electrical and magnetic properties. The main constituents of the ferrites are iron oxide and metal oxides. The necessary of ferrite material has been known to mankind for several centuries prior. For navigation in early twelfth centuries the Chinese use lodestones (Fe_3O_4) in compasses [Smith and Wijin, (1959)]. Later after 1930's the practical use of ferrites in both electrical and magnetic have started. Afterwards it became a passion in researchers in finding ferrite based materials with greater applications.

The crystal structure of spinel ferrite is depends on the cubic close packed oxygen and ions. The crystal structure of spinel ferrite has two interstitial sites namely tetrahedral (A) and octahedral [B] site in which cations with different valence and ionic radii can be incorporated [Smit and Wijin, (1959)].

1.7 NANO FERRITES

Nano ferrites are highly sensitive to synthesize method, sintering condition, amount of constituent metal oxides, various additives include in dopants and impurities [Gadkari *et al.,* (2009); Gama *et al.,* (2006); Jcoba *et al.,* (2004)]. It can be used in preparation of transformer cores, antenna rods, memory chips, high density magnetic recording media, permanent magnets, capacitor, transducers, activators, microwave and computer technology etc [Verma *et al.,* (1999); Nakamura *et al.,* (2003); Waqus *et al.,* (2009)]. In latest fields like drug delivery, magnetic resonance imaging (MRI), catalyst, humidity and gas sensors etc., [Rezlescu *et .al.,* (2004); Xing Liu *et al.,* (2008); Raj *et al.,* (1995)] the ferrites in nanocrystalline form found greater applications.

The handling of ferrite materials is important in altering the properties as per the desired applications [Melagiriyappa and Jayanan, (2009)]. The porosity is most attracted phenomena in ferrites which is completely insignificant in metals. This helps us to explain why ferrites have been used and studied for several decades. The increasing trends in ferrites technology will improve the properties of ferrites and it promises a bright future for ferrite technology [Spaldin and Fiebig, (2005)].

Generally ferrites are classified into three types

- Spinel Ferrite (Cubic Ferrite)
- Hexagonal Ferrite
- Garnet

(I) SPINEL FERRITE (CUBIC FERRITE)

The mostly used ferrites in the ferrite family are spinel ferrites [Valenzuela (2005); Murdock *et al.,* (1992)]. In general the chemical composition of spinel ferrite can be written as MFe_2O_4 where M is a divalent metal ion such as Co^{2+}, Zn^{2+}, Fe^{2+}, Mg^{2+}, Ni^{2+}, Cd^{2+}, Cu^{2+} or a combination of these ions such. The unit cell of spinel ferrite is FCC having eight formula units per unit cell. The formula can be rewritten as $M_8Fe_{16}O_{32}$. The anions are the ultimate and they form an FCC lattice. Among these lattices two types of interstitial positions occur and these are occupied by the metallic cations. There are 96 interstitial sites in the unit cell, 64 tetrahedral (A) and 32 octahedral (B) sites. It is shown in Fig.1.4.

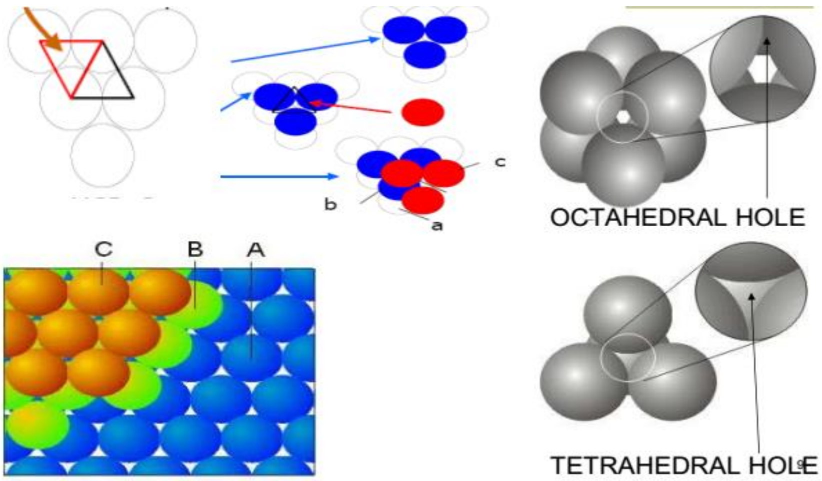

Fig.1.4. STRUCTURE OF SPINEL

The spinel ferrite has been further classified into three categories due to the distribution of cations on tetrahedral (A) and octahedral (B) sites. (a) Normal spinel ferrite (b) Inverse spinel ferrite (c) Intermediate spinel ferrite.

(a): NORMAL SPINEL

Only one kind of cations *i.e.*, Octahedral [B] site then the spinel is normal. In these types of ferrites the divalent cations will occupy tetrahedral (A) sites while the trivalent cations are on octahedral [B] site. Square brackets are normally used to indicate the ionic distribution of the octahedral [B] sites. Normal spinel have been denoted by the formula $[(M^{2+})_A\ [Me^{3+}]_BO_4$. Where M signify divalent ions and me for trivalent ions. A typical example for normal spinel ferrite is $NiFe_2O_4$. Fig.1.5 depicts the schematic diagram of normal spinel.

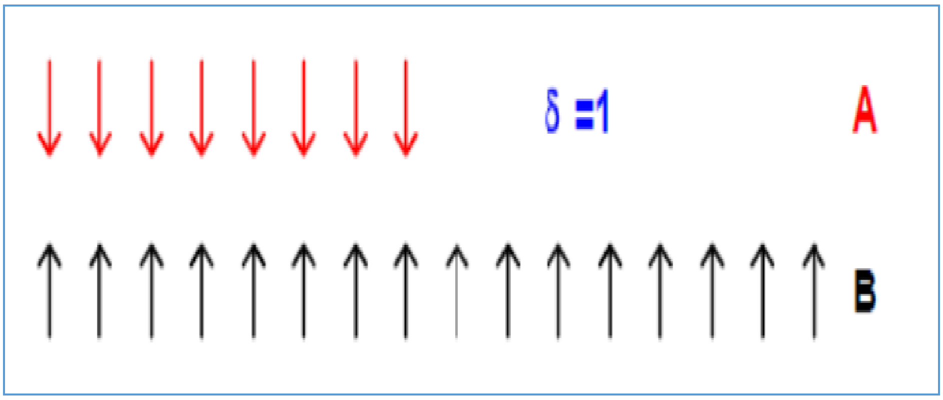

Fig.1.5. NORMAL SPINEL

(b): INVERSE SPINEL

In this inverse spinel structure half of the trivalent ions occupy tetrahedral (A) sites and half octahedral [B] sites, the remaining cations being randomly distributed among the octahedral [B] sites. These ferrites are represented by the formula $(Me^{3+})_A\ [M^{2+}Me^{3+}]_BO_4$. One of the typical examples of inverse spinel ferrite is Fe_3O_4 in which divalent cations of Fe occupy the octahedral [B] sites [Li *et al.,* (2004)]. Fig.1.6 depicts the schematic diagram of inverse spinel.

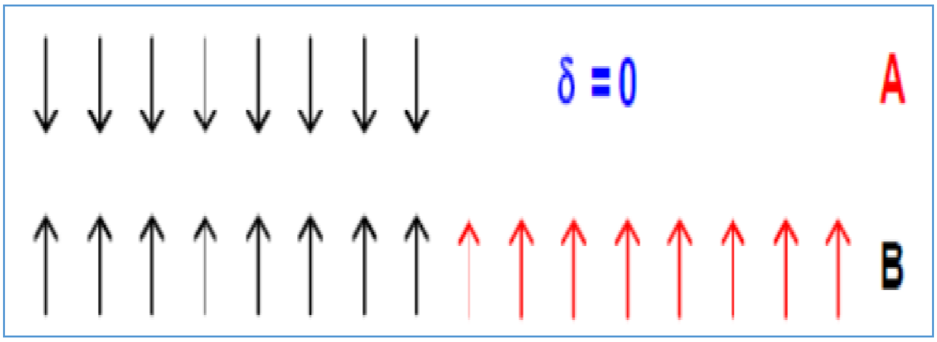

Fig. 1.6. Inverse spinel

(c) Random Spinel

Spinel with ionic distribution, intermediate between normal and inverse are known as mixed spinel e.g. $(M_{\delta}^{2+}Me_{1-\delta}^{2+})_A\ [M_{1-\delta}^{2+}\ Me_{1+\delta}^{3+}]_BO_4$), where, δ is inversion parameter. Where quantity δ depends on the method of preparation and the nature of constituents of ferrites. For complete normal spinel ferrite δ = 1, for complete inverse spinel ferrite δ =0, for mixed spinel ferrite, δ ranges in between these two extreme values. For completely mixed ferrite δ = 1/3. If there is unequal number of each kind of cations on octahedral sites, then the spinel is called mixed. Typical example of mixed spinel ferrites are $MgFe_2O_4$ and $MnFe_2O_4$. Fig.1.7 depicts the schematic diagram of random spinel.

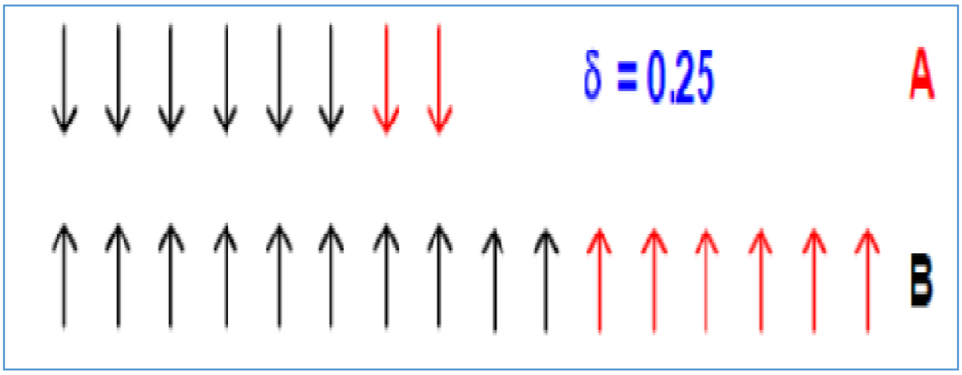

Fig.1.7. Random Spinel

(II) Hexagonal Ferrite

Hexa ferrites are hexagonal or rhombohedral ferromagnetic oxides with formula $MFe_{12}O_{19}$, in which M is an element like barium, lead or strontium. In random ferrites, oxygen ions have closed packed in hexagonal crystal structure. They are broadly used as permanent magnets and have high coercivity and are used at very high frequency. Their hexagonal ferrite lattice is related to the spinel structure with closely packed oxygen ions, but there are also metal ions at some layers with the same ionic radii as that of oxygen ions. The hexagonal ferrites have larger ions than that of garnet ferrite and are formed by the replacement of oxygen ions. Most of these larger ions are barium, strontium or lead.

(III) GARNETS

The general formulas for the unit cell of a pure iron garnet have eight formula units of $M_3Fe_5O_{12}$, in which M is the trivalent rare earth ions (Y, Gd, Dy) [Gatelytė *et al.*, (2011), Srivastava *et al.*, (1997) and Kambale *et al.*, (2011)] In which their cell shape is cubic and the edge length is about 12.5 Å and they have complex crystal structure. They are important owing to their applications in memory structure.

1.8 INTRODUCTION OF NICKEL NANOPARTICLES

Nickel is generally found in ores and sometimes found free in nature. It can be alloyed with tungsten, molybdenum, chromium, iron and other metals without much effort. The electronic configuration of nickel is given as [Ar] $3d^8$ $4s^2$. The synthesis of nickel nanoparticles has received considerable attention because of their extremely applications such as electrical, magnetic, thermal, sensor devices, biological and chemical properties, catalytic, [Byung keun oh *et al.*, (2006);] especially supercapacitor [Baiju Vidhyadharan *et al.*, (2014); Vijayakumar *et al.*, (2013)] properties which did not achieve from those of the bulk materials [Dominguez - Crespo *et al.*, (2009); Wang *et al.*, (2012); Cordente *et al.*, (2001)].

1.9 INTRODUCTION OF COBALT NANOPARTICLES

Cobalt is a Block D, Period 4 element. The morphology of cobalt nanoparticles is spherical, and their appearance is a grey or black powder. Cobalt nanoparticles possess electric and magnetic properties. The electronic configuration of cobalt is given as [Ar] $4s^2 3d^7$. Cobalt nanoparticles found numerous applications in various fields such as micro-electronics, microbatteries, nanowires, catalysis, superconductors, electronic ceramics, electrode active materials, enamels, grinding wheels, solar energy absorbers, super capacitors etc., [Papis *et al.*, (2009); Zhang *et al.*, (2010); Zhao *et al.*, (2015)].

1.10 INTRODUCTION OF NICKEL FERRITES ($NiFe_2O_4$) NANO COMPOSITE

Metal nanoparticles (Ni,Fe,etc.,) have received considerable attention due to their interesting size-dependent optical, electronic, magnetic [Willard *et al.,* 2004], thermal [Jiang *et al.,* 2003], and catalytic properties. Making composite of these materials i.e., nickel and ferrite to form nickel ferrite nanocomposite has yield much better application rather than individual nanoparticles. The ionic radii of Fe^{3+} is 0.64Å and for the Ni^{2+} is 0.74 Å so replacing by one another is simpler task. Nickel ferrite ($NiFe_2O_4$) is one of the most prominent spinel ferrite which finds applications in the fabrication of soft magnets, super capacitor and low loss materials at high frequencies [Mathew *et al.,* (2007) and Fan *et al*., (2009)]. It is known that the interesting electrical and magnetic properties of ferrites depend upon the nature of the ions, charges and its distribution among tetrahedral (A) and octahedral (B) sites. Nickel ferrite is a typical soft ferromagnetic material crystallizing in an entirely inverse and cubic spinel structure having all nickel ions located in the B-sites and ferric ions occupying both A-sites and B-sites [Salavati Niasari *et al*., 2009]. The compound, thus can be denoted by the formula $(Fe^{3+})_A[Ni^{2+}Fe^{3+}]_BO_4^{2-}$.

1.11 INTRODUCTION OF COBALT FERRITES ($CoFe_2O_4$)

Nanosized cobalt has been proposed as an alternative to platinum in recent years and might allow the manufacturing of cheaper and more durable fuel cells. Cobalt is considered to be the first catalyst made from nonprecious metal having properties closely match with those of platinum [Yu *et al.,* (2013)]. Cobalt is one of the most important ferromagnetic metals owing to its three meta-stable phases with different crystallographic structures, namely, the hexagonal closed packed (hcp) phase, the face-centered cubic (fcc) phase, and the epsilon phase [Pandey *et al.,* (2012); Lu *et al.,* (2007)]. The ionic radii of Fe^{3+} is 0.64 Å and for the Co^{2+} is 0.78 Å making composite of cobalt ferrite nanoparticle is a greater task for better applications. Cobalt ferrite ($CoFe_2O_4$) has an inverse spinel magnetic material, with a moderate saturation magnetization, high coercivity, large magneto-crystalline anisotropy, important electrical properties and good mechanical hardness [Chandramohan *et al.,* (2011); Pan *et al.,* (2011)]. In the inverse spinel structure, all the Co^{2+} ions occupy the octahedral sites of lattice structure, half of the Fe^{3+} ions also occupy the same sites and the rest of the Fe^{3+} ions stay in tetrahedral sites [Goldman, (2006)]. Also, Co_3O_4 is a significant p-type semiconductor material with spinel structure applied in different applications such as gas sensors, electrochemical devices, supercapacitors, heterogeneous catalysts, lithium-ion batteries, magnetic materials and photo-catalysts [Yan *et al.,* (2012)]. $CoFe_2O_4$ has rarely been explored as a pseudocapacitor. Deng *et al.,* (2012) have reported the preparation and electrochemical properties of $CoFe_2O_4$nanorods and nanorings.

1.12 INTRODUCTION OF NICKEL COBALT FERRITES ($Ni_{1-x}Co_xFe_2O_4$)

As it have gained thorough knowledge regarding nickel ferrite composite and cobalt ferrite composite making a composite with these combination made nickel cobalt ferrites which give drastic applications when compared to the individual one. Even though, nickel-cobalt ferrite system is one of the important materials for technological application but it is less studied among the whole class of spinel ferrites [Tang *et al.,* (2012)]. Spinel ferrite ($Ni_{1-x}Co_xFe_2O_4$) is the class of oxide materials with remarkable electrical and magnetic properties, which have been investigated and applied during the past few years. Among all inverse spinel ferrites, the nickel substituted cobalt ferrite has been extensively studied in view of their good chemical and thermal stability, capacitance, magnetic anisotropy, high coercivity and various exchange interactions etc. It has various applications in numerous fields including microwave devices [Ashiq *et al.,* (2009)], recording media [Jung and Kang (2009)], magnetic fluids [Huo and Wei, (2009)], gas sensors [Chen *et al.,* (2010)], high density information storage [Koseoglu *et al.,* (2009)], supercapacitor [Bhujun (2016)], ferro-fluids [Sousa *et al.,* (2002)] and catalysts [Ramankutty *et al.,* (2001)].

1.13 INTRODUCTION TO SUPERCAPACITOR

In recent years owing to climate changes and rising depletion of fossil fuel which results in much concentration on investigation and development of the alternative and renewable sources. When compared to other sustainable resources such as sun, wind, water etc., electrical energy storage system have played vital role in our daily life because of its availability and demand. In which the electrical energy storage systems are electrochemical capacitors (ECs) and are capable of delivering a large amount of energy in very short response [Conway, (1999)]. ECs have many advantages like high power density, high cycle efficiency, fast charge/discharge response and long cycle life when compared to normal batteries. Therefore ECs has been regarded as the solution to the mismatch between the fast growth for power requirement of the device and disability of normal batteries to discharge efficiency at higher rates.

1.14 SUPERCAPACITOR USED AS POWER SOURCES

Supercapacitors have found an increasing number of applications that require a ready source of backup energy that can be called on to provide short-term power when regular input power is lost. In these applications, supercapacitors have several advantages over traditional energy storage devices such as batteries, including low maintenance requirements, virtually unlimited cycle life, and low effective series resistance. For energy storage devices, energy density and power density are the two main parameters plays vital role in characterizing the performance of the device. The energy density specifies the amount of energy stored in a given volume or weight of the material. The power density specifies the total energy per second which can be stored in the device. The ideal storage device must be characterized by both high energy density and high power density. Whereas the normal batteries have high energy density but it has poor power density. On the other hand the normal capacitors have low energy density but it has high power density. Any how the supercapacitors of today's innovation can have greater power density with significant high energy density. The Fig.1.8 depicts the Rangone plot of various energy storage devices.

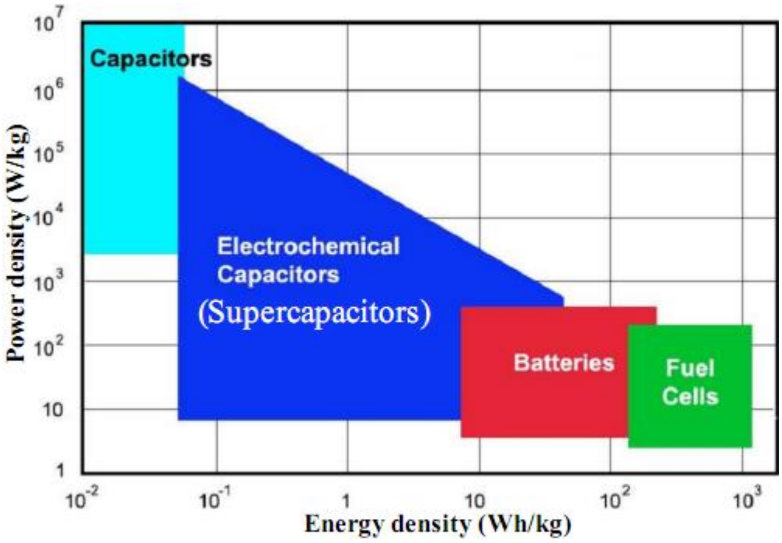

Fig.1.8.RANGONE PLOT FOR VARIOUS ENERGY STORAGE AND CONVERSION DEVICES

The Rangone plots graphically demonstrate the typical specific energy and specific power of energy storage devices and the intermediary characteristics of supercapacitors. Supercapacitors are seen as essential components for the realization of electric values and similar high power electrochemical systems. The schematic diagram Fig.1.9 depicts the working principle of capacitor, supercapacitor (ultracapacitor) and normal batteries. Comparison of properties of normal batteries and electrochemical capacitors is shown in table 2 and some important characteristic state of comparison of batteries, supercapacitor and normal capacitor is shown in table 3.

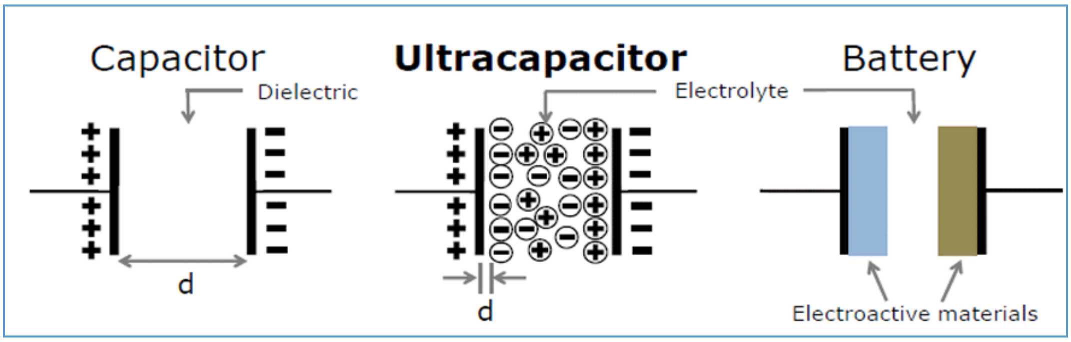

Fig.1.9. SCHEMATIC DIAGRAM OF CAPACITOR, SUPERCAPACITOR (ULTRACAPACITOR) AND NORMAL BATTERIES

TABLE 2: COMPARISON OF PROPERTIES OF NORMAL BATTERIES AND ELECTROCHEMICAL CAPACITORS

Property	**Battery**	**Electrochemical Capacitor**
Storage mechanism	Chemical	Physical
Power limitation	Electrochemical reaction kinetics, active materials conductivity, mass transport	Electrolyte conductivity in separator and electrode pores
Energy limitation	Electrode mass (bulk)	Electrode surface area
Output voltage	Approximate constant value	Sloping value - state of charge known precisely
Charge rate	Reaction kinetics, mass transport	Very high, same as discharge rate
Cycle life limitations	Mechanical stability, chemical reversibility	Side reactions

Life limitation	Thermodynamic stability	Side reactions

TABLE 3: COMPARISON OF SOME IMPORTANT CHARACTERISTIC STATE OF BATTERIES, SUPERCAPACITOR AND NORMAL CAPACITOR

Parameters charge time	**Capacitor $10^{-6} – 10^{-3}$ (F)**	**Super-capacitor 1 – 30 Sec**	**Battery 0.3 – 3 hrs**	**Comparisons of moderate charging time**
Discharge time	$10^{-6} – 10^{-3}$	1 – 30	1 - 4	Moderate discharging time
Energy density (Wh/Kg)	<0.12	1 – 10	20 - 10	High energy density
Power density W/Kg	10,000	1000-2000	50 – 200	Moderate power density
Cycle Life	>500,000	>100,000	500 - 2000	Reasonable good cycle life
Charge/discharge efficiency	~ 1.0	0.9 – 0.96	0.7 – 0.84	High efficiency

1.15 ELECTROCHEMICAL CAPACITOR

On the basis of charge storage mechanisms, the electrochemical capacitors (ECs) can be categorized into two main types (i) Electrochemical double layer capacitor and (ii) Pseudo capacitors. In electrochemical double layer capacitors the capacitance evolves from the charge separation at the electrode and electrolyte interface whereas in pseudo capacitors the charge transfer arising from reversible faradaic reaction occurring in the electrode surface. Therefore the electrode material is much important in the capacitive behavior of electrochemical capacitors (ECs). The main advantage and disadvantages of electrochemical double layer capacitor and pseudo capacitors is shown in Fig.1.10 and table 4 represents the schematic diagram of supercapacitors.

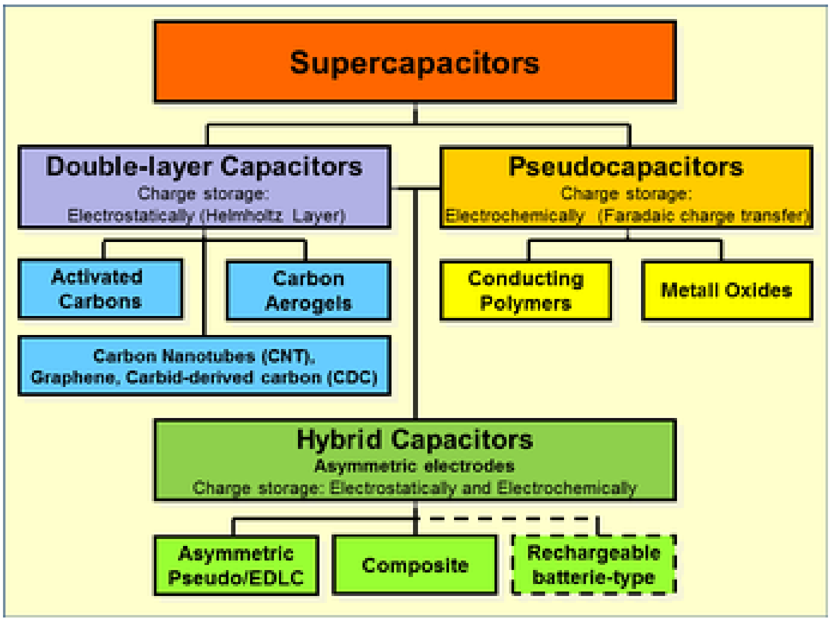
Supercapacitors
Double-layer Capacitors
Charge storage:
Electrostatically (Helmholtz Layer)
Pseudocapacitors
Charge storage:
Electrochemically (Faradaic charge transfer)
Activated Carbons
Carbon Aerogels
Carbon Nanotubes (CNT), Graphene, Carbid-derived carbon (CDC)
Conducting Polymers
Metall Oxides
Hybrid Capacitors
Asymmetric electrodes
Charge storage: Electrostatically and Electrochemically
Asymmetric Pseudo/EDLC
Composite
Rechargeable batterie-type

Fig.1.10. SCHEMATIC DIAGRAM OF SUPERCAPACITORS

TABLE 4: MAIN ADVANTAGE AND DISADVANTAGES OF ELECTROCHEMICAL DOUBLE LAYER CAPACITOR AND PSEUDO CAPACITORS

Electrochemical Double layer capacitor	**Pseudo Capacitor**	**Difference**
Phase angle 90°	Phase angle 45°	More transmission like behavior
Low specific energy density	High specific energy density	Good capacity of charge storage
High reversibility	Moderate reversibility	Reasonably good cycle life
Capacitance remains constant with voltage	Capacitance changes with voltage	Small leakage effect
Narrow potential window (1-3V)	large potential window (1-5V)	Broad range of applications
High power due to good diffusion	Low power due to kinetic limitations	High diffusion resistance

1.16 HYBRID CAPACITOR

In order to attain the full advantage of EDLCs and Pseudo capacitors improvements in the overall performance of a device, the third type of capacitor was attempted which are called as hybrid capacitors. In the hybrid system it renders high power and energy density without sacrificing the cycle stability. The energy storage mechanism in hybrid systems depends on both faradaic and non-faradaic process. In a hybrid system, the electrode configuration are mainly based on either composite electrodes or metal oxide materials lead to the benefit of physical and chemical charge storage mechanisms together in a single electrode [Liu *et al.,* (2010)]. The coupling of ferrite based material electrodes with pseudo capacitors electrodes has gained an immense importance owing to substantial enhancement in total capacitance of the device.

1.17 APPLICATIONS OF SUPER CAPACITORS

With the emerging of latest technologies and applications having challenging power requirements, there is increase interest in supercapacitors, either as stand-alone energy-storage devices for high power needs or for hybrid supercapacitor-battery systems that simultaneously address both power and energy requirements.

1.18 AIM AND SCOPE OF THE PRESENT WORK

- To prepare and characterize nickel ferrite, cobalt ferrite and nickel cobalt ferrite nanoparticles via co-precipitation method using citrate as chelating agent.
- TG/DT analysis is carried out to find optimum calcination temperature.
- XRD, XPS, FTIR and EDAX have been used to study the characterization of prepared nanoferrites.
- To study the morphology of the nanoferrites, FESEM and FETEM have been employed.
- To study the electrochemical properties of the prepared sample by CV method.

CHAPTER – II

LITERATURE REVIEW

2.1. NICKEL FERRITE NANOPARTICLES

Nickel ferrite nano particles have synthesized by **Prasad *and Gajbhiye* (1998)** using citrate precursor technique and control of solid state reactivity. For which nickel nitrate, nitric acid and ferric nitrate is taken as precursor. The crystallization of $NiFe_2O_4$ takes place above 553 K which is evident from a broad exothermic peak around 553 K in TG/DT analysis. XRD patterns of the heat treated samples at various temperatures clearly indicate the single phase, amorphous spinel ferrite formed around 473 K and crystallize completely above 553 K. The crystallite size has been determined from the width of the (311) line using Scherrer method. The crystallite size varies from 6.72 nm to 29.2 nm with heat treatment temperature of 523 K to 973 K. The lattice param*et*er has been found to be a=b=c=8.4372Å.The amorphous $NiFe_2O_4$ consists of spherical particles with a mean size of 45.5 nm and after crystallization the particle size of 36.55 nm which is comparatively smaller and shows the uniform distribution. The samples heat treated at higher temperature (673 K) show bigger particles having mean size 50 nm and the existence of chain like clusters of magnetic single domain particles. The reduction in the BET surface area is observed after the crystallization above 553K. The magnetic and Mossbauer analysis is also carried out which represents single domain particles were found to form the linear chain like clusters because of strong magnetic dipolar interactions.

Kim *et al.*, (2000) have studied $NiFe_2O_4$ using Mossbauer spectroscopy and X-ray diffraction. The crystal was found to have an inverse cubic spinel structure. From the X-ray diffraction pattern of $NiFe_2O_4$ it could not find any other single diffraction peak of Fe_2O_3, NiO, and Fe other than $NiFe_2O_4$. The lattice constant at room temperature was a_o=8.326±0.003 Å which was determined by using the Nelson-Riley function. Mossbauer spectra of $NiFe_2O_4$ was obtained at various absorber temperatures from 13 K to the Neel temperature. The Mossbauer spectra consisted of two sets of six lines corresponding to Fe^{+3} at the tetrahedral (A) and the octahedral (B) sites. The temperature dependence of the magnetic hyperfine fields at Fe nuclei at the tetrahedral (A) and the octahedral (B) sites was analyzed by the Neel theory of ferrimagnetism.

Fang *et al*., (2003) have reported $NiFe_2O_4$ ultrafine powder with high crystallinity has been prepared through a reverse micro emulsion route. TGA curve indicate that $NiFe_2O_4$ could be formed above 550 °C only. The XRD pattern recorded at room temperature from the precursor prepared using above composition (x=0.12) and calcined at 600 °C for 3 h. These peaks are indexed to the cubic $NiFe_2O_4$ phase according to the standard ICDD PDF (Card No. 10-0325). From the XRD line broadening of the (311) peak using the Scherrer equation the crystalline sizes were estimated as 11.2 nm, 16.9 nm, and 28.8 nm for the specimens calcined for 3h at 600 °C, 700 °C, and 800 °C, respectively. The TEM image of powder calcined at 600 °C for 3 h reveals that the discrete particles exist in polyhedron and average crystallite size ranges around 10–15 nm in diam*et*er with high crystallinity. For the magnetic study it is observed that when increasing the particle size by elevating the calcinations temperature, the magnetic phenomenon becomes unapparent and even vanished.

Yang *et al*., (2005) have reported $NiFe_2O_4$ nanopaticles were prepared by inverse titrating chemical co-precipitation using ferric sulphate and nickel chloride as precursor. From TG/DT analysis the pure $NiFe_2O_4$ phase was obtained by calcining the dried precipitate above 350 °C. From the XRD analysis using Scherrer's equation, the crystallite size of the sample calcined at 350, 400, 500, 600, and 700 °C are found to be 9.30, 11.81, 16.90, 23.57, and 39.32 nm respectively. The TEM figures indicate that most of them are fine particles. When calcined at 500 °C for 1 h, the crystalline oxide particles remain well dispersed. It was also found that the particle size increases with increase in sintering temperature. The gas sensing property was carried out in which the sensitivity increases with increasing calcining temperature in the range of 350–400 °C, and then decreases with increasing calcining temperature.

Zhao *et al*., (2007) have synthesized nano-sized nickel ferrite ($NiFe_2O_4$) by hydrothermal method at low temperature using nickel nitrate and ferric nitrate as precursor. From the XRD study it is evident that the products are pure $NiFe_2O$ because all the diffraction peaks can be indexed to $NiFe_2O_4$ and matched well with a cubic crystal structure (JCPDS file No. 86-2267) with space group Fd3m. No peaks of any other phases or impurities can be observed, confirming the purity of the nanoparticles. Using Scherrer's equation the average size of the $NiFe_2O_4$ particles was 12 nm. From TEM analysis $NiFe_2O_4$ nano particles in the size of 5–15 nm can be clearly identified. The electrochemical performance of $NiFe_2O_4$ nanoparticles as the anodic material in lithium ion batteries was tested. It was found that the first discharge capacity of the anode made from $NiFe_2O_4$ nanoparticles could reach a very high value of 1314 $mAhg^{-1}$, while the discharge capacity decreased to 790.8 $mAhg^{-1}$ and 709.0 $mAhg^{-1}$ at a current density of 0.2 $mAcm^{-2}$ after 2 and 3 cycles, respectively.

Jiang *et al.*, (2008) have synthesized nanostructured $NiFe_2O_4$ by a simple refluxing route using urea as precipitator, sodium dodecyl benzene sulfonate (SDBS) as surfactant template. The phase identification of the as-prepared sample was examined by XRD. All of the d*et*ectable peaks can be readily indexed as $NiFe_2O_4$ with an inverse spinel structure, as shown in the standard data (JCPDS card no. 86-2267), and no characteristic peaks of impurities are detected.

The broadening nature of the diffraction peaks suggests that the as-prepared sample is very small in dimension. Using Debye–Scherrer formula the average size of particles is estimated to be about 18.5 nm. The morphology and particle sizes of the as-prepared sample were determined by SEM and TEM. The SEM micrograph indicates that sphere-like $NiFe_2O_4$ nanostructures obtained by this method are uniform in both morphology and particle size. The typical TEM image indicates that the $NiFe_2O_4$ is spherical with the particle sizes in the range of 15–20 nm.

The electron diffraction rings corresponding to $NiFe_2O_4$ are indexed as cubic spinel structure, which is consistent with the results of XRD. In order to investigate the effects of surfactant on the structure and morphology of $NiFe_2O_4$ nanoparticles, a contrast experiment was carried out in the absence of sodium dodecyl benzene sulfonate (SDBS). The resulted sample show irregular morphology with size distribution from 10 to 30 nm. The magnetic properties of the sample were also measured by using a superconducting quantum interference device (SQUID) magnetometer.

Maaz *et al.*, (2009) have reported nickel ferrite ($NiFe_2O_4$) nanoparticles have been synthesized by co-precipitation route using stable ferric and nickel salts with sodium hydroxide as the precipitating agent and oleic acid as the surfactant. The X-ray diffraction pattern of the sample annealed at 1000 °C shows that the final product is cubic $NiFe_2O_4$ with average crystallite size of ~28nm. The XRD peaks were compared to the standard PDF card number 742081 for inverse cubic nickel ferrite. The average sizes of the particles annealed at 600, 700, 800, 900 and 1000 °C for 10h were found to be 8, 11, 18, 24 and 28±3nm using the standard Debye–Scherrer formula. The high- resolution TEM images of the same sample annealed at 1000 °C for 10h reveals that most of the particles appear spherical in shape. The selected area electron diffraction (SAED) analysis of the sample indicating that the nanoparticles prepared are crystalline. Magnetic characterization of the particles was performed by vibrating sample magnetometer (VSM).

Srivastava *et al.*, (2009) have reported nickel ferrite ($NiFe_2O_4$) nanostructures have been synthesized by sol–gel method using glycolic acid as a chelating agent. Glycolic acid acts as a fuel, which decomposes the m*et*al complexes at low temperature and yields impurity free $NiFe_2O_4$ nanocrystalline structures. From TG/DT analysis it has been observed that $NiFe_2O_4$ synthesized by citric acid as the chelating agent the compl*et*e thermal decomposition of the gel take place over 600 °C. The bands occurred at 717 and 593cm^{-1} corresponds to Ni–O and Fe–O bonds respectively and the wide band around 3430cm^{-1} is corresponds to the hydroxyl group from the FTIR analysis confirms the presence of $NiFe_2O_4$ nanoparticles. The structural characterization of calcined powder was performed by XRD analysis. All the diffraction peaks of the synthesized particles match well with the reported values in standard JCPDS file no.:10-325. The particle size of $NiFe_2O_4$ nanoparticles was calculated using the Scherrer's relation and it was found to be 16–32nm. The lattice param*et*er of $NiFe_2O_4$ are calculated to be, a=b=c=0.84172±0.00261. The XRD result also reveals that the nanocrystal contains single phase spinel structure with Fd3m space group. FESEM images shows that the prepared samples were uniform and almost spherical structural morphology with a narrow size distribution. The energy band gap of the synthesized $NiFe_2O_4$ nanocrystalline structure was calculated to be~5eV. The optical studies show a direct allowed transition in $NiFe_2O_4$ nanostructures.

Jacob and Khadar (2010) have reported the single crystalline nickel ferrite $NiFe_2O_4$ which has an inverse spinel structure is reported to exhibit a mixed spinel structure when its grain size is reduced to nanom*et*er range. Nanoparticles of $NiFe_2O_4$ were synthesized by a co-precipitation method, nickel nitrate and ferric nitrate as precursor. XRD patterns of the nanostructured samples show broad peaks indicating the fine grain size of the samples. The peaks observed in the spectra agreed closely with the data in the International Center for Diffraction Data (card number 10–325) for $NiFe_2O_4$ indicating that the samples synthesized were nanoparticles of pure $NiFe_2O_4$. Room temperature Mössbauer spectra of the nanostructured $NiFe_2O_4$ samples are found to be average grain sizes of 13 and 51 nm. Mössbauer study of the smallest and largest grain-sized samples revealed surface spin canting and change in coordination of the iron ions at tetrahedral and octahedral sites with reduction in grain size. FTIR and micro-Raman spectroscopic studies also yielded convincing evidence for a transformation of the structure. The results of the present study lead to the inference that the properties of nanosized $NiFe_2O_4$particle emerged from a transformation of their structure from inverse spinel structure to mixed spinel.

The $NiFe_2O_4$ ceramic powders prepared by combustion synthesis and sol-gel methods by **Anwar *et al.*, (2011)** using ferric nitrate and nickel nitrate as precursor**.** The TG/DT analysis reveals the optimum temperature as 400 °C since there is no considerable weight loss beyond that indicating the formation of nickel ferrite. The powder XRD patterns of $NiFe_2O_4$ matched well with the standard pattern available in the data base of joint committee on powder diffraction standards (JCPDS 10-0325). The calculated cubic lattice param*et*er values in the synthesized samples are almost same [8.340(1) Å] which are in good agreement with the value of the standard $NiFe_2O_4$ (8.339 Å).SEM images show that the ferrite powders contain uneven morphology consisting of a large smooth area with no evidence of any intergranular phase.

Electrochemical performance of these electrode materials as investigated by cyclic voltammetry (CV) and the corresponding specific capacitance (SC) values were also reported. Further they observed specific capacitance value of $NiFe_2O_4$ depends on the morphology which can be controlled by the synthesis method adopted. In addition $NiFe_2O_4$ synthesized by sol-gel method exhibited a specific capacitance of 97.5 Fg^{-1} which is higher than that of the $NiFe_2O_4$ obtained through other synthesis methods.

Senthilkumar *et al.*, (2011) have reported the submicron-sized $NiFe_2O_4$ particles were synthesized by the molten salt method at 900 °C using binary melts of a NaCl and KCl mixture that acts as a flux. The X-ray diffraction pattern confirmed the single phase, high crystalline and cubic structure of $NiFe_2O_4$ with Fd3m space group. The diffraction peak obtained are in very good agreement with the reported values (JCPDS card No. 44-1485). In FTIR study the high frequency absorption band ν_1, is at 552.3 cm^{-1}, and a lower frequency absorption band ν_2 is in the range of 400–415 cm^{-1}. The high frequency absorption band ν_1 is assigned to the str*et*ching vibration of the t*et*rahedral m*et*al oxygen bond while the lower frequency absorption band ν_2 is attributed to the m*et*al oxygen vibrations in the octahedral sites. The FTIR spectra reveal the str*et*ching vibration of octahedral complexes of Fe^{3+} to O^{2-} through the observed band around 552.3 cm^{-1}.The SEM and TEM image had indicated the formation of submicron-sized $NiFe_2O_4$ particles. The electrical conductivity of 1.42×10^{-4} S cm^{-1} was observed at 873 K. The $NiFe_2O_4$ showed a pseudocapacitive

property in 1 M of a $LiClO_4$ electrolyte and exhibited a specific capacitance of 18.5 Fg^{-1} at
10 mVs^{-1}.

Anju Ahlawat *et al.*, (2011) have reported super-paramagnetic nickel ferrite single phase nanoparticles by the sol–gel auto-combustion method using nickel nitrate, ferric nitrate and citric acid as precursor. As prepared powder was further calcined at different temperatures for 4 h, resulting in nanoparticles of bigger size. The XRD analysis reveals that the sample having space group Fd3m and of inverse spinel structure. The average crystallite size of ~9nm have been synthesized at a low temperature 220 °C. The nanoparticles exhibited super-paramagnetic behavior and changes in cation distribution as revealed by the Mossbauer, Raman and X-ray diffraction studies. The Mossbauer spectra collected at 5 K and under 5T applied magnetic field showed mixed spinel structure and canted spin order for the nanoparticles, whereas there is collinear spin order with inverse spinel structure for larger particles. The vibrational spectra of the nanoparticles showed a redshift and broadening in the Raman line shape due to confinement effects.

Al-Hoshan *et al.*, (2012) have reported that the electro catalysis of oxygen evolution reaction (OER) has been studied at the face centered cubic (FCC) $Ni_xFe_{3-x}O_4$ ($0 \leq x \leq 1.0$) anodes in 1M KOH solutions at 25 °C. These oxides were synthesized by the hydrothermal method and reproduced in the form of film on a nickel support by an oxide-slurry painting technique. The effect of Ni substitution in the base oxide (Fe_3O_4) was investigated with regards to morphology, structure and catalytic performance by some sophisticated techniques. SEM micrographs of $NiFe_2O_4$ oxide powders, sintered at 400 °C for 8 h revealed that oxide particles have an octahedron shape with conspicuous crystal faces and inhomogeneous grain size. From IR spectra the frequency bands ν_1 at 577 cm^{-1} and ν_2 at 457 cm^{-1} revealed the formation of pure spinel ferrites phase with two sub-lattices t*et*rahedral (A-site) and octahedral (B-site) sites. The diffractograms exhibited X-ray lines corresponding to the spinel phase. The XRD patterns showed cubic lattice with a space group of Fd3m. The obtained diffraction peaks well matched with the standard data (JCPDS No. 44-1485; a = 0.8339 nm) confirmed the formed product is pure $NiFe_2O_4$. The crystallite size was found to be 13 nm using standard scherrer formula.

Liu *et al.*, (2013) have synthesized nanocrystalline spinel $NiFe_2O_4$ nanoparticles by a novel low temperature route using nickel chloride and ferric chloride as precursor. From TG/DT analysis it reveals that when the temperature is raised up to 350 °C, the weight of the sample is constant, which indicates the precursor burned completely and forming the final product. $NiFe_2O_4$ was obtained by burning the precursor after 350 °C. The XRD patterns of the powders calcined for 8 h at different temperatures were carried out. The main peaks of $NiFe_2O_4$ powder start to appear after calcination at 350 °C. This is in agreement with the TGA data. With the increase of the synthesis temperature, the diffraction peaks become sharper and narrower, indicating the increased crystallinity. The diffraction peaks can be indexed to $NiFe_2O_4$ (JCPDS Card # 10-0325). The average particle size of the sample was obtained by using Scherrer formula. FTIR bands of solid are generally assigned to clarify vibration of ions of tetrahedral and octahedral complexes of spinel structures. The absorption band at 596.8 cm^{-1} corresponds to stretching vibration of tetrahedral groups Fe–O. The absorption band at 400.0 cm^{-1} is attributed to the vibrations of octahedral groups Fe–O. The last two strong absorption bands are characteristic of inverse spinel ferrites. The different values are due to the different distances of Fe^{3+}-O^{2-} for octahedral and tetrahedral sites. TEM image reveals that the particles are spherical in shape. The chemical composition and states of the $NiFe_2O_4$ calcined at 700 °C was found by using XPS analysis and it confirms that the sample consists only of nickel, iron, carbon and oxygen elements. The electrochemical reaction mechanism and charge–discharge mechanism of the nanocrystalline $NiFe_2O_4$ were proposed based on thermo gravimetric analysis (TGA) and cyclic Voltammetry study. The charge–discharge tests indicated that the sample calcined at 700 °C shows the highest initial discharge capacity is 1400 $mAhg^{-1}$ attributed to the nanometer size and the better crystallinity of the powder. A discharge capacity stabilizes at about 600 $mAhg^{-1}$ after 10 cycles. The columbic efficiency is improved. The synthesis method is relatively low cost and convenient for large- scale production.

Khosravi sand Eftekhar (2013) have reported that the spinel-type $NiFe_2O_4$ nanoparticles have been fabricated by sol–gel method using nickel nitrate, ferric nitrate and ethylene glycol as precursor. From DTA analysis no obvious change was observed above 700 °C. Hence, it is possible to conclude that the calcination temperature is about 700 °C. All the diffraction peaks obtained in XRD analysis matched well with the standard JCPDS data (Card No.10-0325) confirms the formation of cubic (a=3.2499 Å) spinel structure of the $NiFe_2O_4$. The particle sizes of $NiFe_2O_4$ nanoparticles calcinated at 700°C are found to be 17nm using the standard Scherrer formula. Two main broad metal–oxygen bands are seen in the

Far-IR spectra of all spinels and ferrites in particular the highest one, ν_1, generally observed in 510 cm^{-1}corresponds to intrinsic stretching vibrations of the metal at the tetrahedral site whereas the ν_2, lowest band usually observed in 338 cm^{-1} which is assigned to octahedral metal stretching. From TEM image, the morphology of nanoparticles is found to be homogeneous and the spinel nanoparticles consist of uniform quasi spherical crystallites with an average size of 17 nm. Moreover the $NiFe_2O_4$ can be a promising surface material to remove azo dye from water over a wide range of dye concentrations is studied.

Thakur *et al.*, (2015) have reported the synthesis of $NiFe_2O_4$ by co-precipitation method using nickel chloride and ferric chloride as precursor. The XRD pattern confirms the formation of spinel cubic structure, which is consistent with the powder diffraction file of JCPDS#742081. The different reflection lines in XRD pattern were used for obtaining the average particle size using the Debye–Scherrer equation and it was found to be ~15nm. The particle size decreased with variation of iron content, while the lattice parameter increased with the increase in Fe content. By using VSM technique, a significant change in the magnetic properties was observed in $NiFe_2O_4$ system.

2.2.COBALT FERRITE NANOPARTICLES

Cobalt ferrite nanoparticles have synthesized by **Pillai and Shah (1996)** using water-in-oil micro emulsions consisting of water, cetyl tri-methyl ammonium bromide (surfactant), n-butanol (co-surfactant), and n-octane (oil). Precursor hydroxides were precipitated in the aqueous cores of water-in-oil micro emulsions and these were then separated and calcined to give the $CoFe_2O_4$ nanoparticles. The X-ray diffractogram of the calcined powder shows all the peaks for $CoFe_2O_4$ marked by their indices. No other peaks or impurities are detected. Therefore, X-ray diffraction confirmed the formation of phase pure cobalt ferrite. TEM of the calcined particles showed agglomerates of particles and the particle was less than 50 nm in size. It is evident that growth of particles has taken place during calcination to obtain cobalt ferrite. Magnetic measurements were done at room temperature by VSM instrument.

Experimental investigation is to describe the stability of cobalt ferrite colloidal spheres, by analyzing the time variation of the optical absorbance of the suspensions as a function of pH and magnetic field strength by **de Vicente *et al.*, (2000)**. TEM micrographs demonstrate that the synthesized particles are in spherical in shape. Structural and chemical analysis of the particles suggests that they are composed of a mixed cobalt-iron ferrite and magnetite. In order to consider all possible particle-particle interactions that might be responsible for the observed behavior, the classical DLVO theory was extended to include magnetic dipole attractions. The electric double layer of the particles was characterized by electrophoresis, and it was found that the ferrite colloids have an isoelectric point (pH_{iep}, or pH of zero zeta potential, ζ) of ~6.5. This is confirmed by stability measurements: the absolute value of the initial slope of the absorbance-time curves shows a pronounced maximum around pH 7.

Silva *et al.*, (2004) have synthesized nanocrystalline $CoFe_2O_4$ powders using metallic nitrates dispersed in aqueous media precipitated by stoichiometric amount of NH_4OH. In TG analysis above 600 °C no weight loss was observed and the crystallization process was finished. XRF analyses showed that cobalt ferrites prepared in molar ratio of Fe: Co: NH_4OH:H_2O = 2:1:11:11 approached the stoichiometric desired $CoFe_2O_4$. In FTIR analysis it is able to found the high-frequency band to the tetrahedral group (575 cm^{-1} region) and the low frequency band to octahedral group (374 cm^{-1}) and it confirmed that the synthesized sample as cobalt ferrite. XRD diffractograms reflects the cubic spinel structure and the absence of extra peaks evidence the phase purity. The magnetic characteristics of $CoFe_2O_4$ powders thermally treated at various temperatures were also carried out using VSM.

XiaohongYang *et al.*, (2005) have prepared the mixed transition-metal spinel oxide $CoFe_2O_4$ through a co-precipitation method using ferric chloride and cobalt chloride as precursor. All diffraction peaks can XRD indexed to a pure cubic phase having space group Fd3m with lattice parameter a=8:384 Å which matches well with the reported value (JCPDS#22-1086).No foreign phase was detected, ensuring the phase purity.

The SEM analysis reveals that the obtained product is even with a particle size of 180 nm. The XPS analysis confirms that the synthesized sample only contains core spectra of Co and Fe. The electrochemical performances of $CoFe_2O_4$ as active material for lithium ion battery were tested in the Teflon cells. It is found that the first discharge capacity is close to 882 $mAhg^{-1}$ at a current density of 0.2$mAcm^{-2}$, corresponding to the reaction of 7.7 Li^+ per $CoFe_2O_4$. And the mechanism of the reaction of lithium with cobalt ferrite spinel was discussed.

Qu *et al.*, (2006) have synthesized cobalt ferrite nanoparticles at different temperatures without any subsequent heat treatment using cobalt chloride and ferric chloride as precursor. The XRD patterns reveal that all peaks correspond to the characteristic peaks of cubic spinel type lattice of $CoFe_2O_4$ (JCPDS file No# 22-1086).The average crystallite sizes of the cobalt ferrite particles were determined from the full-width at half maximum of the (311) peak using the well-known Scherrer equation as 2.4 nm at 40 °C to 47.4 nm at 100 °C. The morphologies and particle size of as-prepared $CoFe_2O_4$ particles synthesized at different reaction temperatures were examined by using FESEM and TEM and it was confirmed the formation of equiaxial shaped single-phase cubic spinel structure and the increase of particle size with the increasing reaction temperature. Raman spectra of the samples confirmed the formation of $CoFe_2O_4$ nanoparticles. The magnetic measurement also been carried out by using VSM.

Xiao *et al.*, (2007) have prepared cobalt ferrite ($CoFe_2O_4$) nanopowder by a low-temperature, auto-combustion method using cobalt nitrate, ferric nitrate and citric acid as precursor. The autocatalytic nature of the combustion process of nitrate–citrate gel was investigated by TG/DTA measurements. It was observed that no significant weight loss beyond 441 °C implies the formation of cobalt ferrite. The metal oxygen vibration of the sample was identified by using FTIR analysis. From XRD analysis the lattice constant of $CoFe_2O_4$ was calculated from the strongest diffraction peak of (311) of as-burnt powder as 8.381 Å. The average size of as-prepared $CoFe_2O_4$ crystallites was evaluated according to Scherrer's formula based on the obtained XRD data. The calculated average crystallite sizes corresponding to as-burnt powder and the samples annealed at 400, 600, 800 and 900 °C for 2 h are 22.7, 25.1, 25.2, 41.2 and 43.1 nm respectively shows the increase of particle size with the increase of annealing temperature was noticed. From TEM analysis it could be found that all $CoFe_2O_4$ nanoparticles are in square shape and almost with an identical size. The average particle size estimated by statistical method is ~21.3 nm. By using VSM the magnetic properties was also carried out.

Lavela and Tirado (2007) have prepared $CoFe_2O_4$ nanoparticles by a sol–gel process based on vacuum sublimation with citrate precursor. This route of synthesis has demonstrated to be effective for the preparation of pure phases with a tunable morphology by modifying composition, param*et*ers of the precursor synthesis and annealing conditions. Aggregated of primary particles were observed for iron containing samples annealed over 600 °C. The XRD patterns of $CoFe_2O_4$

oxides obtained from different precursors and annealed at 900 °C for 6 h shows the presence of $CoFe_2O_4$ nanoparticles. The morphology of the $CoFe_2O_4$ nanoparticle were obtained by SEM analysis. $CoFe_2O_4$ obtained from a precursor with a M: Cit 1:1 ratio, 0.3M metal concentration and a final pH solution equal to seven demonstrated to be able of sustaining capacities in an extended cycling. The corresponding oxide annealed at 1000 °C for 24 h led to a notorious improvement of the cycling performance. Values as high as 739 $mAhg^{-1}$ were achieved after 75 cycles. Morphological and magnetic characteristics of cobalt ferrite nanoparticles synthesized by **Toksha *et al.*, (2008)** using sol–gel auto combustion method using nitrates of respective m*et*al ions have studied. The analysis of X-ray diffraction pattern of the calcined powder synthesized using this route shows that the final product is $CoFe_2O_4$ with the expected inverse spinel structure. The value of lattice constant is found to be 8.3731 Å ± 0.004 Å. The size of the particles was determined by Scherrer formula using most incense (311) peak. The average sizes of the particles calcined at 570 °C were found to be 15 nm. By annealing 15 nm particles at 800 °C and 900 °C for 10 h, particle sizes of 24 and 28 ± 2 nm were obtained. Finally, on further annealing, at 1000 °C for 8 and 12 h, respectively, 32 and 40 ± 2 nm particles were obtained. A Transmission Electron Microscope (TEM) confirmed the formation of single phase cobalt ferrite nanoparticles in the range 11 to 40 nm.

A facile synth*et*ic route of cobalt ferrite nano particles with narrow size distribution was reported by **Gu *et al.*, (2008)**. The key feature of this method involved a very rapid mixing of reducible metal cations with sodium borohydride and simultaneous reduction in a colloid mill, which is followed by a slow oxidation in a separate hydrothermal treatment. From XRD all diffraction peaks can be indexed in a simple cubic lattice, and the positions along with relative intensity of peaks match well with standard $CoFe_2O_4$ powder diffraction data (JCPDS 22-1086), indicating that the obtained products have an Fd3m cubic spinel structure. EDAX analysis confirmed that the sample only contains cobalt and ferrite. SEM photographs of $CoFe_2O_4$ samples reveal that all samples exhibit a compact arrangement of homogeneous nanoparticles with roughly spherical shape. In addition, TEM micrographs confirm the nature of uniform particle size. A typical HRTEM image of an individual $CoFe_2O_4$ nanocrystal indicates inter planar distances of 0.253 nm that are characteristic of (311) spinel planes. The above results support the nanocrystalline and monodisperse nature of the $CoFe_2O_4$ samples. XPS analysis is carried out and this route only should be considered representative of the surface or external layers composition of the synthesized ferrite samples. Magnetic measurement was carried out by using vibrating sample magnetometer.

$CoFe_2O_4$ nanoparticles have prepared by **Wang *et al.*, (2008)** by co-precipitation method in 60 °C homogeneous aqueous solution. XRD pattern confirmed the presence of cobalt ferrite nanoparticle and it has a cubic structure. The lattice parameter "a" had been estimated as 8.381. The morphology of the sample was analyzed through SEM analysis which confirmed the decreasing of particle size and aggregation increasing of the particles is also observed with the increasing of Fe^{3+} in starting solution.
Effects of calcination temperatures varying from 400 to 1000 °C on structural and magnetic properties of nano-composites formed by cobalt ferrite dispersed in the sol-gel silica matrix using tetrakis (2-hydroxy*et*hyl) orthosilicate (THEOS) as water-soluble silica precursor have been investigated by **Gharagozlou (2011)**. The XRD patterns of the samples calcined at different temperatures varying from 400 to 1000 °C suggesting that the particles of $CoFe_2O_4$ had been nucleated in the silica matrix. X-ray diffraction patterns showed poor crystallinity up to calcination temperature of 600 °C. Further the intensity of peaks increases and the diffraction peaks become sharper and narrower. This indicates the enhancement of the crystallinity which originated from the increment of the crystalline volume ratio due to the size enlargement of the nuclei. All the diffraction peaks confirmed the formation of the pure single-phase cobalt ferrite with the face-centered cubic spinel phase and Fd3m space group. The crystallite size of all samples prepared at different calcination temperatures estimated from XRD peak broadening using Scherrer's formula. From FTIR the broad band at 1630 cm^{-1} of the alcogel precursor ascribed to the H-O-H bending vibration of the free or absorbed water. The band at 1384 cm^{-1} is associated with the antisymmetric NO_3 str*et*ching vibration arising from the residual nitrate groups in the alcogel. TG/DT analysis confirmed that above 300 °C the weight loss is almost negligible showing that the majority of the mass loss occurs under 300 °C which allows for optimization of the calcination temperature. TEM images and selected area electron diffraction (SAED) pattern of the nanocomposites calcined at 600 °C and 800 °C indicate that almost spherical cobalt ferrite nanoparticles were embedded in the silica network. The average particle sizes of the nanocomposites calcined at 600 °C and 800 °C were about 10 nm and 27 nm, respectively. The magnetic measurement also carried out by using vibrating sample magnetometer.

Jagminas *et al.*, (2013) have reported that the peculiarities of the synthesis of cobalt ferrite nanoparticles by complex assisted co-precipitation route under ambient pressure in argon atmosphere and under increased pressure conditions. $Co_xFe_{3-x}O_4$ nanoparticles with “x” from 0.3 to 1.0 in size of 1–20 nm were fabricated. The impact of the solution composition and reaction conditions on the size and stoichiometry of cobalt ferrite nanoparticles obtained were evaluated. AFM and TEM observations of the obtained ferrites indicated that the particles made in all investigated solutions are spherical. In XRD, all diffraction peaks matched well with the standard data International Centre Diffraction Data card number 04-005-7078 and confirmed the presence of cobalt ferrite nanoparticles. Hydrodynamic size of cobalt ferrite nanoparticles in water upon the rinsing, centrifugation and neutralization steps is discussed. Also it was found that ultrafine cobalt ferrite nanoparticles are especially stable during storage in water for months and can be successfully applied for magnetic resonance imagining.

Nanocrystalline cobalt ferrite powder has been synthesized by **Kumar *et al.*, (2013)** employing co-precipitation methods using cobalt nitrate, ferric nitrate and citric acid as precursor. Typical FESEM image of the sample annealed at 800 °C shows that the particles have an almost homogeneous distribution, and some of them are in agglomerated form. The EDAX patterns revealed the presence of Co, Fe, Au, and O elements in the sample. All of the diffraction peaks confirmed the formation of the pure single-phase cobalt ferrite with the face-centered cubic spinel phase and Fd3m space group. Crystallite sizes calculated by Scherrer's formula and it revealed that the particle size get increases with increase of annealing temperature. From FTIR analysis the higher frequency absorption band (ν_1) lies in the range 500 to 600 cm^{-1} and is assigned to vibration of the tetrahedral m*et*al complex which consists of a bond between m*et*al ion ($O\text{-}M_{Oct}$) oxygen ion and the tetrahedral site, and the lower frequency absorption band (ν_2) lies in the range of 400 to 490 cm^{-1} and is assigned to vibration of the octahedral m*et*al complex which consists of a bond between metal ion ($O\text{-}M_{Tet}$) oxygen ion and the octahedral site.

Houshiar *et al.*, (2014) have synthesized cobalt ferrite ($CoFe_2O_4$) nanoparticles using three different methods; combustion, co-precipitation, and precipitation using cobalt nitrate and ferric nitrate as precursor. XRD patterns of $CoFe_2O_4$ samples, prepared by combustion, co-precipitation and precipitation methods were carried out and by using Sherrer’s equation, the average sizes of the crystals were estimated to be 69.5, 49.5 and 34.7 nm respectively. XRD pattern is in accordance with inverse cubic spinel structure with space group Fd3m which is in agreement with JCPDS standard cards no. 01-077-0426 with no extra phases. The lattice constants in three methods are almost equal and which is good agreement with the reported in literatures for cobalt ferrite (a=8.39 Å). The morphology of the sample was carried out by SEM and TEM analysis. VSM data of samples showed a saturation point in the magnetic field of less than 15 kOe.

Shanmugavani *et al.*, (2015) have synthesized cobalt ferrite nanoparticles by facile combustion method using aspartic acid and glycine as fuels. From XRD analysis it confirmed that the $CoFe_2O_4$ particles exhibits expected phase formation with cubic crystal structure. The necessary structural (XRD and FTIR), morphological (FESEM and TEM) electrical (Cole–Cole plot and Conductance spectra) and magnetic (VSM) properties were analyzed. XPS analysis confirmed that the present sample as cobalt ferrite. For all the three different pH conditions (5, 7 and 10) $CoFe_2O_4$ nanoparticles employed as a negative electrode for supercapacitors. For positive electrodes, $Co(OH)_2$ and $Co_2Fe(CN)_6$ particles are prepared by w*et* chemical method and studied its structural and morphological features. The electrochemical properties revealed that the aspartic acid assisted $CoFe_2O_4$ (CA7) negative electrode exhibits an enhanced specific capacitance of 758 Fg^{-1} at 2 mVs^{-1} in 1 M KOH. Similarly, the galvanostatic charge–discharge analysis (GCD) shows a specific capacitance of 356 F g^{-1} at 1 mA cm^{-2}. On the other hand, $Co(OH)_2$ and $Co_2Fe(CN)_6$ shows the specific capacitance of 932 and 817 Fg^{-1} at 2 mVs^{-1}, respectively. Interestingly, the fabricated asymmetric supercapacitors, $CoFe_2O_4\|AC$, $CoFe_2O_4\|Co(OH)_2$ and $CoFe_2O_4\|Co_2Fe(CN)_6$ provides the specific capacitance of 339, 127 and 125 Fg^{-1} at 1 mVs^{-1} in 1 M KOH, respectively.

Hao *et al.*, (2015) have reported a facile hydrothermal method combined with a post solution reaction is developed to synthesize interconnected three-dimension (3D) hierarchical $Co_{3-x}Fe_xO_4$ ferrite (CF) on nickel foam. By controlling the experimental param*et*ers, the structures of the products are tailored from nanoflowers to microflowers with different sized void interiors. The obtained 3D hierarchical flower-like CF are characterized by field emission scanning electron microscopy, X-ray diffraction, and inductively coupled plasma mass spectrom*et*er analysis. The 3D hierarchical flower-like CF-nickel foam with the rational structural feature could be used as binder and conductive agent-free supercapacitor electrodes directly. Such integrated electrodes exhibit a high specific capacitance and well cycling stability when the charge-discharge current density is high. Remarkably, the 3D hierarchical CF microflowers exhibit specific capacitance values of 768Fg^{-1} at a constant current density of 6 Ag^{-1}. The CF microflowers also show high charge-discharge reversibility with an efficiency of 79.2% after 5000 cycles.

NICKEL COBALT FERRITE NANOPARTICLES: Nickel cobalt ferrite nanoparticles have prepared using aerosol route by **Singhal *et al.*, (2005)**. The TEM micrograph of $Co_{0.6}Ni_{0.4}Fe_2O_4$ are spherical particles consist of a large numbers of small particles held together by interfacial forces which are responsible for the spherical shape of larger (agglomerate) particles. The diffraction pattern of as-prepared and annealed samples of $Co_{0.2}Ni_{0.8}Fe_2O_4$ are initially amorphous nature and further on increasing the annealing temperature, the diffraction peaks become narrower and sharper, suggesting the increase in particle size and crystallinity. The particle size was calculated from most intense peak (311) using Sherrer formula. All the samples were found to be face centered cubic (fcc) with Fd3m space group. Lattice param*et*er 'a' was found to decrease linearly with nickel concentration. Magnetic measurement using VSM was also carried out for the sample.

Nermin Kasapoglu *et al.*, (2007) reported a series of Ni doped cobalt ferrite compounds with the formula $Ni_xCo_{1-x}Fe_2O_4$ where x=0, 0.2, 0.4, 0.6, 0.8, and 1.0 were prepared by hydrothermal method and subsequently sintered/annealed at 600 °C for 3 h. X-ray powder diffraction (XRD) patterns of $Ni_xCo_{1-x}Fe_2O_4$ (x=0, 0.2, 0.4, 0.6, 0.8, and 1.0) match well with the both standard data of pure $CoFe_2O_4$ JCPDS file No: 22-1086 (x = 0), and pure $NiFe_2O_4$ JCPDS file No: 10-325 (x = 1).The values of the lattice param*et*ers found for $NiFe_2O_4$ (a = 8.339 Å) and for $CoFe_2O_4$ (a = 8.381Å) agree with those reported in JCPDS card numbers 10-325 and 22-1086, respectively. From FTIR study the band ν_1 generally observed in the range 600–550 cm^{-1} corresponds to an intrinsic stretching vibrations of the metal at the tetrahedral site, whereas the ν_2 lowest band, usually observed in the range 450–385cm^{-1}, is assigned to octahedral-metal stretching. SEM micrographs show a broad size distribution is observed which consists of octahedral nano particle with sizes ranging from 30 to 35 nm. ESR signals show that when the concentration of Ni^{2+} increases, the peak to peak line width decreases, but the resonance field increases. Based on ESR results, a core-shell type of formation was proposed where the core is made up of undoped $CoFe_2O_4$ and the shell is Ni^{2+} doped $CoFe_2O_4$.

Maaz *et al.*, (2009) have reported Ni-doped cobalt ferrite [$Co_{1-x}Ni_xFe_2O_4$ ($0 \leq x \leq 1$)] synthesized by coprecipitation route have been studied as a function of doping concentration (x) and particle size. The X-ray diffraction patterns of $NiFe_2O_4$, $Ni_{0.5}Co_{0.5}Fe_2O_4$ and $CoFe_2O_4$ annealed at 600 °C for 6h match well with the standard JCPDS cards (742081 for $NiFe_2O_4$ and 791744 for $CoFe_2O_4$). Using Scherrer's formula for prominent (311) peak, the crystallite sizes of all the prepared samples were obtained in the range (18–28±4nm). TEM images it is seen that the nanoparticles are composed of different nanograins separated from each other. It is also seen that most of the particles appear spherical in shape however few elongated particles. The SAED patterns indicate that Co-ferrite, Ni-doped cobalt and Ni-ferrite nanoparticles were found in well-crystalline nature. By using VSM the magnetic measurements also carried out.

Binghai Liu *et al.*, (2008) have reported a detailed study on the various magnetic $Ni_xCo_{1-x}Fe_2O_4$ prepared by using a mechano-chemical process. Both XRD and TEM analysis indicate that the $Ni_xCo_{1-x}Fe_2O_4$ samples annealed at 1000 °C were all well crystalline single spinal phase. The particle size get increases with the increase of annealing temperature was confirmed by both studies of XRD and TEM. The microstructure and magnetic studies indicated that the milling induced high coercivity could be ascribed to milling induced stress anisotropy and to the pinning effect.

A series of cobalt-doped nickel ferrite with composition of $Ni_{(1-x)}CoxFe_2O_4$ with "x" ranges from 0.0 to 0.8 (in steps of 0.2) have prepared by **Kambale *et al.*, (2009)** using standard ceramic technique. The confirmation of single-phase formation and structural analysis were carried out by employing X-ray diffraction technique. The microstructural features were observed by scanning electron microscopy. An infrared spectroscopy study shows the presence of absorption bands in the higher frequency range around 578 cm^{-1} (ν_1) and in the lower frequency range around 396 cm^{-1} (ν_2). These observed peaks indicate the presence of t*et*rahedral and octahedral group complexes, respectively, within the spinel phase. In an effort to understand the conduction mechanism, complex impedance measurements were carried out. The results of complex impedance measurements show that as the cobalt concentration increases, the total impedances (Z' and Z'') decrease. Dielectric measurement was also carried out.

Almeida *et al.*, (2012) have reported briefly regarding the hydrothermal synthesis of $Co_xNi_{1-x}Fe_2O_4$ nanoparticles (NPs) from mixed $FeCl_3$ / $CoCl_2$ / $NiCl_2$ precursor solution has been investigated as a function of reaction temperature. The diffraction peaks obtained from the XRD analysis matches well with the both $NiFe_2O_4$, (JCPDS 10-325) and $CoFe_2O_4$ (JCPDS 1-1121), are assigned to the development of crystalline $Ni_xCo_{1-x}Fe_2O_4$. TEM analysis revealed the morphology of the sample as spherical in shape. The EDX confirmed that the synthesized sample only contain Ni, Co and Fe.

Derakhshi *et al.*, (2012) have reported nickel doped cobalt ferrite magnetic nanoparticles were synthesized in a homogeneous aqueous solution in presence of surfactant by co-precipitation route. The particle size was estimated by the full width half maximum (FWHM) of the strongest X-ray diffraction (XRD) peak. The average particle size varied in the range of 19-32 nm; the particle size was controlled via controlling calcination temperature which was in the range of 600 to 900 °C. The results showed that a well crystalline single cubic structure of nickel doped $CoFe_2O_4$ phase was formed through precipitation precursors at pH value of 11. The pH was adjusted by the use of ammonium hydroxide solution. The morphology and particle sized of the nickel doped cobalt ferrite nanopowders were determined by SEM. It indicate that sphere like nickel doped cobalt ferrite nanostructures obtained by co-precipitation method are uniform in both morphology and particle size at various temperature.

Gonsalves *et al.*, (2012) have reported nanoparticles of the spinel ferrite, $Co_{1x}Ni_xFe_2O_4$ (x = 0, 0.2, 0.3) have been synthesized by the precursor combustion technique. Novel precursors of m*et*al fumarato - hydrazinate have been employed to yield the nanosized spinel ferrite. This synth*et*ic strategy can be applied to synthesize different ferrites though the precursor may need to be chemically modified as per the desired end product. The precursor forms nanosize ferrite by way of autocatalytic decomposition after its ignition. The chemical analysis, total mass loss, and infrared spectral analysis confirms the formation of the complex and the formula $Co_{1-x}Ni_xFe_2O_4$ $(C_4H_2O_4)_3.6N_2H_4$ (x = 0, 0.2, 0.3) has been accordingly fixed. The TG/DSC studies of the complex show two-step dehydrazination followed by two-step decarboxylation to form single phase $Co_{1x}Ni_xFe_2O_4$ nanoparticles. This has been confirmed by XRD and IR. In FTIR analysis show three absorption bands in the region 3,185-3,350 cm^{-1} due to the N–H str*et*ching frequencies. The N–N stretching frequency at ~974 cm^{-1} proves the bidentate bridging nature of the hydrazine ligand. The asymmetric and symmetric str*et*ching frequencies of the carboxylate ions are seen at ~1,585 and 1,383 cm^{-1}, respectively, with the Dm $(\nu_{asy}-\nu_{sym})$ separation of 202 cm^{-1}, which indicate the monodentate linkage of both carboxylate groups in the dianion. The IR data confirms the formation of cobalt nickel ferrous fumarato-hydrazinate in all of the complexes. The Curie temperature of the samples was found to be comparable with the reported values.

Sontu *et al.*, (2014) have synthesized nickel-substituted cobalt ferrite nano-particles by self-combustion method using citric acid, nickel nitrate, cobalt nitrate and ferric nitrate as precursor. Spinel structure of annealed powders of nickel-substituted cobalt ferrite has been confirmed by the XRD. All the diffraction peaks of ferrite samples are indexed on the basis of the face centered cubic unit cell (JCPDS no. 00-022-1086 for $CoFe_2O_4$ and JCPDS no. 00-044-1485 for $NiFe_2O_4$). All the samples are found to have Fd3m space group symmetry. The cubic lattice param*et*er 'a' is calculated. The particle sizes of the samples fall in a very small range from 38 nm to 50 nm. To study the temperature dependent DC conductivity the samples are silver coated for a good m*et*allic contact. The conductivity study is performed in the temperature range of 300– 600 K. Using VSM the magnetic property has been studied. It is shown here that the magnetic and electrical properties can be tuned by varying the nickel concentration.

Abdul Gaffoor and Ravinder 2014) have synthesized nano-ferrites of the composition $Ni_{1-x}Co_xFe_2O_4$ (where x=0.0, 0.2, 0.4, 0.6, 0.80 and 1.0) at a very low temperature (180 °C) by citrate-gel auto combustion method The synthesized powders were sintered at 500 °C for four hours in an air. XRD patterns and the crystalline phases were identified by comparison with reference data from the JCPDS card No. 742081 for Nickel ferrites ($NiFe_2O_4$) and JCPDS card no. 791744 for Cobalt ferrites ($CoFe_2O_4$). The XRD patterns of all the cobalt substituted nickel ferrites showed a homogeneous single phased cubic spinel belonging to the space group Fd3m. All the Braggs reflections have been indexed, which confirmed the formation of a well-defined single phase cubic spinel structure without any impurity. The strongest reflection has come from (311) plane that indicates spinel phase. The lattice parameter was found to increases linearly with increasing Co concentration. This linear variation indicates that the Ni-Co ferrite system obeys Vegard's law. The SEM images show that the particles have an almost homogeneous distribution, and some of them are in agglomerated form. It is evidenced by SEM images that the aggregation of particles lies in nano- metric region. The particles were observed as uniform grains (in different SEM images) confirming the crystalline structure of Ni-Co nanoferrites which were detected by XRD study. The elemental analysis of all the Ni-Co nano ferrite samples with different compositions was analyzed by Energy Dispersive Spectrometer which indicates the elemental and atomic composition in the sample. The compounds show the presence of Ni, Co, Fe and O without precipitating cations.

Velhal *et al.*, (2015) have reported nickel substituted cobalt ferrite nanoparticles with composition $Co_{1-x}Ni_xFe_2O_4$ ($0 \leq x \leq 1$) was synthesized using simple, low temperature auto combustion method. For which nickel nitrate, cobalt nitrate and ferric nitrate is used as precursor. The X-ray diffraction patterns reveal the formation of cubic phase spinel structure. All the reflections are in good agreement with the JCPDS card no.22-1086 and 10-0325.The crystallite size varies from 30-44 nm with the nickel content. Porous and agglomerated morphology of the bulk sample was displayed in the scanning electron microscopy. All the Raman bands are consistent with those reported for other cubic inverse spinel ferrite structures, which belong to the Fd3m space group. Micro Raman spectroscopy reveals continuous shift of E_g and $E_g(2)$ stokes line up to 0.8 Ni substitution. The dielectric constant and loss tangent decreases with frequency, whereas conductivity increases with increase in frequency was reported.

Nirmalesh Naveen and Subramanian Selladurai (2016) have reported highly porous nickel cobaltite nanoparticles were synthesized by micro combustion technique. X-ray diffraction study reveals the changes in phase, crystallinity, and particle size of the prepared samples with respect to calcination temperature. Typical porous 3D foam like morphology of the materials was identified from the FESEM and HRTEM images. BET measurement further confirms the mesoporous nature of the samples with high-surface area. Mixed valence state of ions was identified from XPS measurements. Electrochemical studies disclose the impact of calcination temperature on the electrodes capacitive performance. 3D porous morphology of the material allows the complete utilization of active material available for the electrolyte ions. $NiCo_2O_4$ calcined at 400 °C exhibited the maximum specific capacitance of 908 Fg^{-1} at 5 mV/s scan rate among the prepared samples and 90 % capacitance retention at the end of 1000 cycles. Impedance study demonstrates the low resistance and facile diffusion of electrolyte ions within the material.

Bhujun *et al.*, (2016) have reported that the nanocrystallites of three mixed ternary transition metal ferrite were prepared by a facile sol gel method and adopted as electrode material for super capacitors. The phase development of the samples was determined using Fourier transform infrared (FTIR) and thermal gravimetric analysis (TG). X-ray diffraction (XRD) analysis revealed the formation of a single-phase spinel ferrite in $CuCoFe_2O_4$, $NiCoFe_2O_4$ and $NiCuFe_2O_4$. The surface characteristics and elemental composition of the nanocomposites have been studied by means of FESEM as well as EDS. The electrochemical performance of the nano- materials was evaluated using a two-electrode configuration by cyclic voltammetry, electrochemical impedance spectroscopy and galvanostatic technique in 1 M KOH electrolyte and was found to be in the order of: CuCoF>NiCoF>NiCuF. A maximum specific capacitance of 221 Fg^{-1} was obtained with CuCoF at a scan rate of 5 mVs^{-1}. In addition to an excellent cycling stability, an energy density of 7.9 $kWkg^{-1}$ was obtained at a current density of 1 Ag^{-1}. The high electrochemical performance of nanocomposites obtained indicates that these materials are promising electrodes for supercapacitors.

CHAPTER – III

MATERIALS AND METHODS

3.1. CHEMICALS

Nickel nitrate hexa hydrate [Ni $(NO_3)_2.6H_2O$], cobalt nitrate hexa hydrate [Co $(NO_3)_2.6H_2O$], ferric nitrate nono hydrate [Fe $(NO_3)_2.9H_2O$], citric acid [$C_6H_8O_7$] and sodium hydroxide [NaOH] were purchased from Merck AR grade and used without any further purification. Sample preparation and dilutions were made up of ultrapure double distilled water.

3.2. SYNTHESIS of $NiFe_2O_4$ NANOPARTICLES

For the synthesis of $NiFe_2O_4$ nanoparticles 0.1M Ni $(NO_3)_2{\cdot}6H_2O$, 0.2M Fe $(NO_3)_2{\cdot}9H_2O$ and 0.29M of citric acid ($C_6H_8O_7.H_2O$) were dissolved in 20 ml of deionized water individually. Afterwards the solution was added one by one respectively with stirring at 650 rpm. Appropriate amount of sodium hydroxide (NaOH) was added as precipitating agent to preserve the pH value around 9. Then, the dissolved solution was kept stirrer for 3h at 80 °C. A dark brown colour precipitate was formed and it was thoroughly washed several times using deionized water and acetone. Then the precipitate was dried in the oven to form the $NiFe_2O_4$ powder at 100 °C for 2 hours and then it was calcinated at different temperatures such as 400 °C, 600 °C and 800 °C.

3.3. SYNTHESIS of $CoFe_2O_4$ NANOPARTICLES

The synthesis of $CoFe_2O_4$ nanoparticles, 0.1M Co $(NO_3)_2{\cdot}6H_2O$, 0.2 M Fe $(NO_3)_3{\cdot}9H_2O$ and 0.29 M of citric acid ($C_6H_8O_7$) were dissolved in 20 ml of deionized water independently. Further the solution was added one by one respectively with continuous stirring 650 rpm at 80 °C. Appropriate amount of sodium hydroxide (NaOH) is added as precipitating agent and it is found that the pH value sustains around 9. The stirred solution was retained in for 3 h at 80 °C. Dark brown colour precipitate was obtained and it was systematically washed numerous times using de-ionized water and acetone. Afterwards the precipitate was dried in the oven to form the $CoFe_2O_4$ powder at 100 °C for 2 hours and then it was calcinated for different temperatures namely 400 °C, 600 °C and 800 °C.

3.4. SYNTHESIS of $Ni_{1-x}Co_xFe_2O_4$ NANOPARTICLES

The preparation of $Ni_{1-x}Co_xFe_2O_4$nanoparticles, Co $(NO_3)_2 \cdot 6H_2O$, Ni $(NO_3)_2 \cdot 6H_2O$, Fe $(NO_3)_3 \cdot 9H_2O$ and citric acid ($C_6H_8O_7$) were taken as precursor. The value “x” has been changed from 0.3, 0.5 and 0.7 to achieve different concentrations of nickel and cobalt in nickel cobalt ferrite. Desired stoichiometric proportions of all metal nitrates and citric acid were weighed and it is dissolved independently each minimum amount 20 ml of deionized water. Later the whole dissolution, the metal nitrates were mixed together to maintain the Ni+Co/Fe ratio of 1:2. Then, the aqueous solution of metal nitrate and citric acid was mixed together in the molar ratio of 1:3. Subsequently, the entire solution was kept with constant stirring for 650 rpm at 80°C on a hot plate included magnetic stirrer. Proper amount of sodium hydroxide (NaOH) is added as precipitating agent and it is found that the pH value bears around 9. Further, the stirred solution was kept in continues stirrer for 3 h at 80 °C. Finally a dark brown colour precipitate was obtained. Acetone and de-ionized water was used to wash the attained precipitate numerous times systematically. Afterwards, the precipitate was dried in the hot air oven for 2 hours at 100 °C to form the $NiCoFe_2O_4$ powder and the samples are calcinated at different temperatures such as 400 °C, 600 °C and 800 °C.

3.5. MATERIALS CHARACTERIZATION

3.5.1. *Thermo gravimetric Analysis (TGA)*

The thermal properties like heat capacities, the glass transition temperature, melting and degradation of macromolecules can be analyzed by using thermogravimetry and differential thermal analysis along with differential scanning calorimetric (DSC). Thermo gravimetric Analysis (TGA) continuously monitors the weight of a sample during isothermal or dynamic temperature scans over the range from 30 °C to 1000 °C in an air, nitrogen, oxygen, or specialty atmosphere.

3.5.1a. *Working Principle*

Thermo Gravimetric analysis (TGA) technique uses heat to force reactions and subsequent physical changes in materials [Liufang Yang *et al.*, (2005)]. TGA provides quantitative measurement of mass change in materials associated with transition and thermal degradation. TGA records change in mass from dehydration, decomposition, and oxidation of a sample with time and temperature. Characteristic thermo-gravimetric curves are given for specific materials and chemical compounds due to unique sequence from physicochemical reactions occurring over specific temperature ranges and heating rates. These unique characteristics are related to the molecular structure of the sample.

3.5.1b *Instrumentation*

TGA analyzer consists of a high-precision balance with a pan loaded with the sample. The pan is placed in a small electrically heated oven with a thermocouple to accurately measure the temperature. The atmosphere may be purged with an inert gas to prevent oxidation or other undesired reactions. A computer is used to control the instrument. Fig.3.1 shows the instrument for TGA.

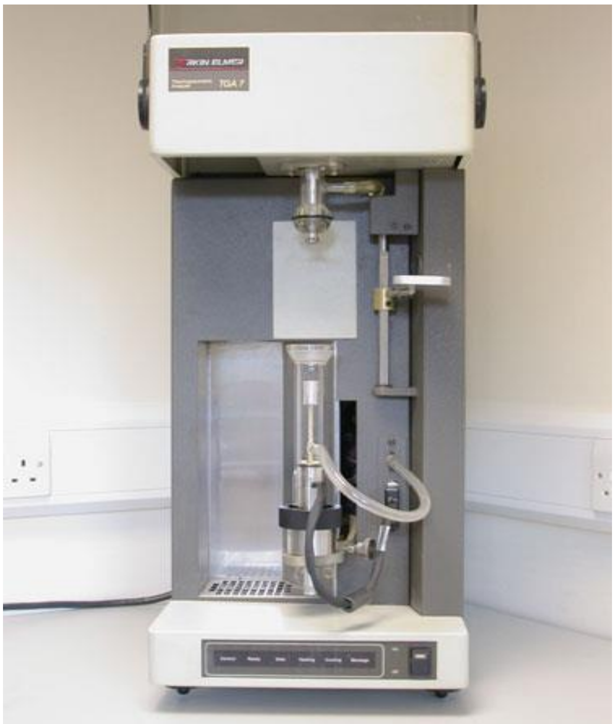

Fig. 3.1. AN INSTRUMENT FOR TGA (NETZSCH - STA 449 F3 JUPITER)

3.5.1c *Analysis of TGA curve*

TG analysis can be carried out by raising the temperature gradually and plotting weight (percentage) against temperature. The temperature in many testing methods routinely reaches 1000 °C or greater, but the oven is greatly insulated from the instrument. After the data are obtained, curve smoothing and other operations may be done such as to find the exact points of inflection. Simultaneous TGA-DTA/DSC measures both heat flow and weight changes (TGA) in a material as a function of temperature or time in a controlled atmosphere. Simultaneous measurement of these two material properties not only improves productivity but also simplifies interpretation of the results. The complementary information obtained allows differentiation between endothermic and exothermic events which have no associated weight loss (e.g., melting and crystallization) and those which involve a weight loss (e.g., degradation). Hi-resolution TGA technique is often employed to obtain greater accuracy in areas where the derivative curve peaks. This is done so that the exact temperature at which a peak occurs can be more accurately identified. As many weight loss curves look similar, the weight loss curve may require transformation before results may be interpreted. A derivative weight loss curve can be used to tell the point at which weight loss is most apparent. Again, interpretation is limited without further modifications and deconvolution of the overlapping peaks may be required.

3.5.2. DIFFERENTIAL THERMAL ANALYSIS (DTA)

Differential thermal analysis (DTA) is a thermo analytic technique. The method has been used predominantly for the determination of inorganic systems.

3.5.2a. *Working Principle*

In DTA, the material under study and an inert reference (which does not go through phase transition in the temperature range of interest) are heated (or cooled) under identical conditions, while recording any temperature difference between sample and reference. This differential temperature is then plotted against time, or against temperature (DTA curve or thermo-gram). Changes in the sample, either exothermic or endothermic, can be detected relative to the inert reference. Thus, a DTA curve provides data on the transformations that have occurred, such as glass-transitions, crystallization, melting and sublimation. Differential temperatures can arise between two inert samples when their response to the applied heat-treatment may not be identical. So DTA can also be used to study thermal properties and phase changes which do not lead to a change in enthalpy.

3.5.2b. *Instrumentation*

Apparatus

The DTA cell consists of mainly four parts:

i. Sample holder comprising thermocouples, sample containers, and a ceramic or metallic block
ii. Furnace
iii. Temperature programmer
iv. Recording system

The essential requirements of the furnace are that it should provide a stable and sufficiently large hot-zone and must be able to respond rapidly to commands from the temperature programmer. A temperature programmer is essential in order to obtain constant heating rates. The recording system must have a low inertia to faithfully reproduce variations in the experimental set up. Fig.3.2 shows the experimental set up of a DTA cell.

The sample holder assembly consists of a thermocouple each for the sample and reference, surrounded by a block to ensure an even heat distribution. The sample is contained in a small crucible designed with an indentation on the base to ensure a snug fit over the thermocouple bead. The crucible may be made of materials such as pyrex, silica, nickel or platinum, depending on the temperature and nature of the tests involved. The thermocouples should not be placed in direct contact with the sample to avoid contamination and degradation. Metallic blocks are less prone to base-line drift when compared with ceramics which contain porosity. On the other hand, their high thermal conductivity leads to smaller DTA peaks. The sample assembly is isolated against electrical interference from the furnace wiring with an earthed sheath, often made of platinum-coated ceramic material. The sheath can also be used to contain the sample region within a controlled atmosphere or a vacuum. During experiments at temperatures in the range 200 to 400 °C, problems are encountered in transferring heat uniformly away from the specimen.

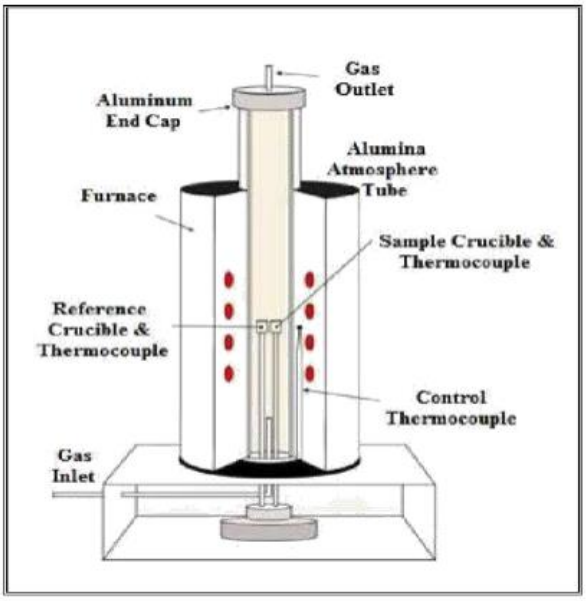

Fig. 3.2. EXPERIMENTAL SET UP OF A DTA CELL

These may be mitigated by using thermocouples in the form of flat discs to ensure optimum thermal contact with the now flat- bottomed sample container, made of aluminium or platinum foil. To ensure reproducibility, it is then necessary to ensure that the thermocouple and container are consistently located with respect to each other. The effects of specimen environment, composition, size and surface-to-volume ratio all affect powder decomposition reactions, whereas these particular variables may not affect solid-state phase changes. Experiments are frequently performed on powders so the resulting data may not be representative of bulk samples, where transformations may be controlled by the buildup of strain energy. The packing state of any powder sample becomes important in decomposition reactions and can lead to large variations between apparently identical samples. In some circumstances, the rate of heat evolution may be high enough to saturate the response capability of the measuring system; it is better than to dilute the test sample with inert material. For the measurement of phase transformation temperatures, it is advisable to ensure that the peak temperature does not vary with sample size. The shape of a DTA peak does depend on sample weight and the heating rate used. Lowering the heating rate is roughly equivalent to reducing the sample weight; both lead to sharper peaks with improved resolution, although this is only useful if the signal to noise ratio is not compromised. The influence of heating rate on the peak shape and nature can be used to advantage in the study of decomposition reactions, but for kinetic analysis it is important to minimize thermal gradients by reducing specimen size or heating rate. (ii) Interpretation and presentation of data a simple DTA curve may consist of linear portions displaced from the abscissa because the heat capacities and thermal conductivities of the test and reference samples are not identical, and of peaks corresponding to the evolution or absorption of heat following physical or chemical changes in the test sample. The test results are a graph of the DTA signal (micro-volts) on the Y-axis plotted versus the sample temperature in °C on the X-axis.

3.5.2d. *Instrument details*

Thermo gravimetric analysis (TGA) and differential thermal analysis (DTA) studies have been performed using Thermal analyzer (NETZSCH-STA 449F3-JUPITER) at a heating rate of 20 °C/min in N_2 gas atmosphere. This is available at Centralized Instrumentation and Service Laboratory (CISL), Department of Physics, Annamalai University, Tamilnadu, India.

3.5.3. FOURIER TRANSFORM INFRARED SPECTROSCOPY (FTIR)

3.5.3a. *Working Principle*

When infrared light is passed through the sample of a compound, some of the frequencies are absorbed while others are transmitted. The variation of IR absorbance against frequency gives the IR spectrum. The IR spectrum of a compound is essentially the superposition of absorption bands of specific functional groups. One of the best features regions can be correlated with specific stretching and bending modes of these functional groups. Thus, by interpreting the spectrum, it is possible to state that whether certain functional groups are present or not. The essential features of conventional infrared spectrometer are a source of infrared light, a monochromator and a detector. Different radiation sources, optical systems and detectors are needed for different regions.

Grating instrument offer high resolution that permits separation of closely spaced absorption band positions, intensities and high scanning speeds for a given resolution and noise level. Modern spectrometers have attachments that permit speed suppression, scale expansion, repetitive scanning and automatic control of slit width and gain which are controlled by a microprocessor.

3.5.3b. *Working*

The typical FTIR instrument is shown in Fig.3.3. This consists of a moving mirror (B), a fixed mirror (A) and a beam splitter. Radiation from IR source after collimation is divided into two beams at the beam splitter; half of it moving to a fixed mirror and other half to a moving mirror. The sample cell is placed in between the interferometer and the detector. After reflection the two beams recombined at the beam splitter. For any particular wavelength, the beam constructively or destructively interferes depending on the difference in optical paths between the two mirrors. This signal is amplified at very precise intervals through the mirror scan. The resulting signal comprises all the information required to reconstruct the spectrum through a mathematical process known as Fourier Transform.

FTIR spectrometer has numerous distinct advantages over conventional depressive spectrometers. There is only one moving part involved (rotation mirror), which is fixed on a frictionless air bearing, in which depression or filtering is not mandatory, since all wavelengths are detected throughout the scan. This has the identical signal to noise to ratio, as a depressive instrument.

3.5.3c. *Recording of FTIR spectra*

In the present work the FTIR spectra of all the samples were recorded using PerkinElmer Spectrum RX 1. The standard resolution in the range 4000 to 400 cm^{-1} is ± 1 cm^{-1}. The spectrometer possesses auto-align energy optimization and dynamically associated interferometer. It is built-in with a KBr beam splitter, a detector and a mid-IR source. It possesses a wavelength precision of 0.01 cm^{-1} and a signal to noise ratio 20,000:1.

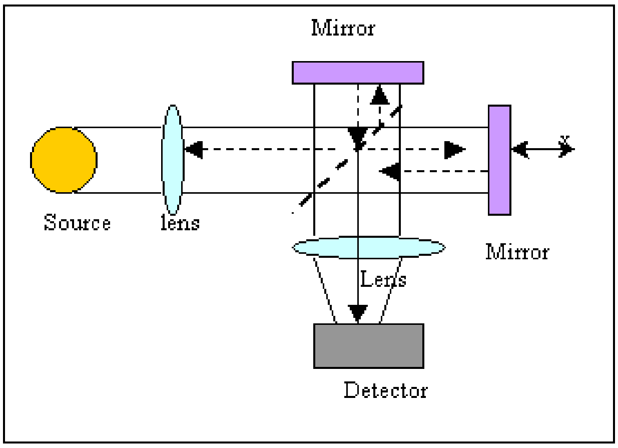

Fig. 3.3. FTIR-INSTRUMENT

3.5.3d. *Instrument Details*

The FTIR spectra were recorded by using the instrument PerkinElmer Spectrum RX 1 from Instrumentation Centre, St. Joseph's College, Tiruchirapalli, and Tamilnadu, India.

3.5.4. X-RAY DIFFRACTION (XRD)

The crystal lattice is a three dimensional array of atoms in space with the lattice planes separated by a distance d. When a monochromatic X-rays fall on the crystalline surface they are scattered and gives rise to interference phenomenon. The diffracted X-rays from various planes with integral multiple (n) of wavelength (λ) will interfere constructively and results in a large output signal at the corresponding angles in the spectrum. The diffraction with half integral multiple of wavelength will interfere destructively and will cancel each other's effect. By changing the angle (θ) the lattice spacing (d) varies to satisfy the Bragg's law, as shown schematically in Fig.3.4.

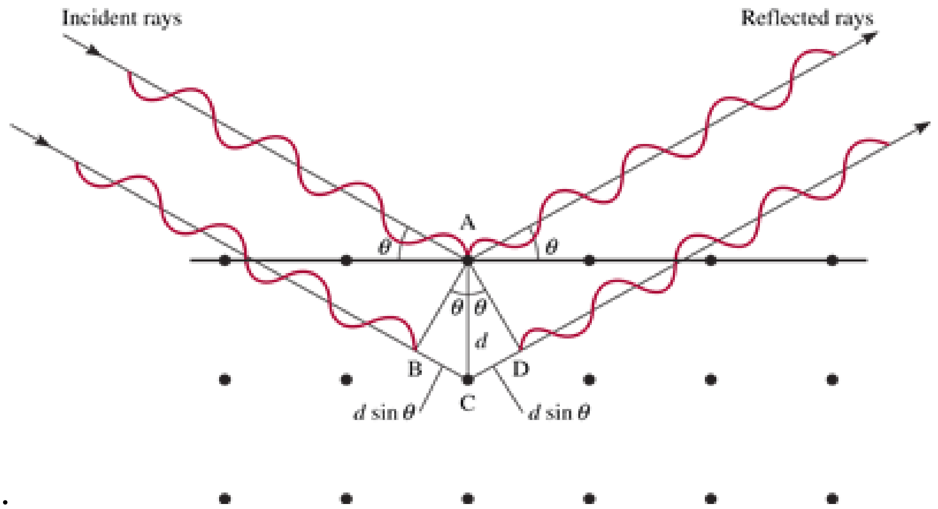

Fig. 3.4. BRAGG'S SCATTERING FROM LATTICE PLANES WITH SPACING "D" WITH THE SAME ANGLE OF INCIDENCE AND THE ANGLE OF REFLECTION.

XRD pattern plays an important role in determining the lattice parameter and the number of planes with various orientations for powder samples. The grains in the powder samples are randomly oriented and the peak positions are used to identify the planes. The wave length of an X-ray source is known and the angle (θ) can be estimated from the XRD spectra and hence the lattice spacing (d) can be calculated using Bragg‟s law (3.1).

$$n\lambda = 2d \sin\theta \qquad \rightarrow (3.1)$$

Since the powder samples used in this study are pure nickel ferrite, cobalt ferrite and nickel cobalt ferrite nanoparticles, therefore the lattice parameter can be calculated from equation (3.2). The lattice spacing (d) can be calculated by using Miller Indices that describes the orientation of planes with respect to different crystal axis and the lattice spacing $d_{hkl}$for synthesized sample is given by the equation

$$a= d_{hkl} (h^2+k^2+l^2)^{1/2} \rightarrow (3.2)$$

Where "a" is the lattice constant and h, k, l are the Miller indices along x, y, and z-axis respectively.

3.5.4a. *Sample Preparation*

For recording XRD, the samples were coated on the glass substrates. The coated samples were allowed to dry and then measured in reflection geometry. During the recording of the diffractogram, a narrow slit 0.1 mm was used with a scanning speed of 0.02/sec. The sample was firmly pressed into aluminum holder, with an area of 10 nm. The diffraction patterns were obtained over the 2θ value in the region of 10 ° to 80 ° at a scan step time of 10 seconds. The estimated error in the lattice parameters are of the order of 0.005Å.The experimental pattern was compared with patterns obtained from JCPDS database. The average grain size of the film can be calculated using the Scherrer‟s formula

$$D = \frac{K\lambda}{\beta \, Cos\, \theta} \rightarrow (3.3)$$

Where,D represents the crystallite size, K (= 0.9) is a constant associated to the shape of the crystal, λ is the incident wavelength of Cu-Kα radiation of the XRD, β indicates the peak width at mid-height and h is the considered angle in radians, and θ is the Bragg diffraction angle.

3.5.4b. *Instrument Details*

The X-ray diffraction (XRD) patterns of the powdered samples were recorded from Allagappa University, Karaikudi, Tamil Nadu using X‟PERT PRO (Model no: PW3040/60) diffractometer with Cu-Kα radiation (k = 1.5406 Å).

3.5.5. SCANNING ELECTRON MICROSCOPE (SEM)

It is high magnification electron microscope where a focused electron beam is used to image a specimen. SEM has higher depth of field, higher resolution and larger magnification. The beam of electrons is produced by an electron source that can be made of many different materials depend upon the nature of the source (like thermo-ionic or field emission source). The beam of electrons is then attracted by the anode, which is put at higher positive potential. In the case of thermionic source there is a cloud of electrons in the vacuum because the electrons are given high energy to overcome the work function of material and then accelerated by the anode, while for field emission (FE) source the electrons are extracted from the material through a high electric field and the tunneled electrons are then accelerated by the anode. This beam is then passed through a condenser lens to magnify the beam and then to make the beam smooth and parallel. The highly scattered electrons from the beam are removed through the condenser aperture. The beam is then passed through a set of coils that is used for scanning the beam. The scanning beam is then passed through the objective lens, which focuses the beam further and then the beam is finally passed through the objective aperture to remove the high angle scattered electrons as shown in Fig.3.5. When the beam hits the sample, it gives rise to electrons (secondary, backscattered and Auger electrons) and X-rays and is detected by various detectors. All these electrons and X-rays collect different information from the sample underneath. For example the secondary electrons are used for surface topography; back scattered electrons (BSE) have the information about the atomic number and surface topology because they interact with the nucleus of the atom. The atoms with larger nuclei will yield high BSE.

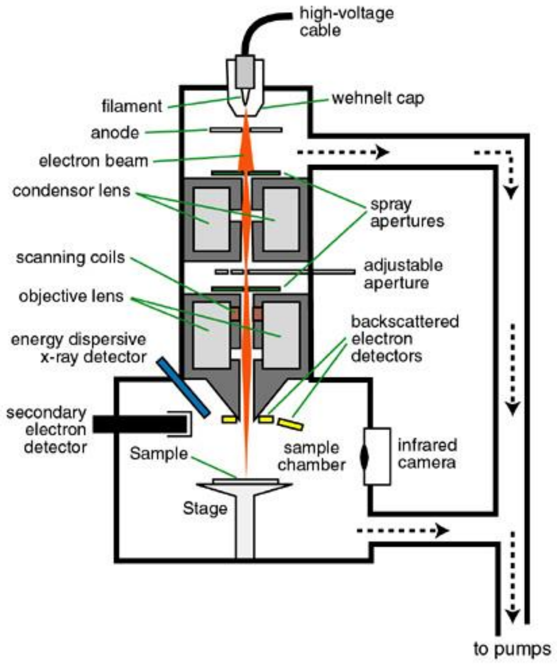

Fig. 3.5: SCHEMATIC DIAGRAM OF SCANNING ELECTRON MICROSCOPE (SEM)

When the beam hits the sample, it gives rise to electrons (secondary, backscattered and Auger electrons) and X-rays and is detected by various detectors. All these electrons and X-rays collect different information from the sample. For example the secondary electrons are used for surface topography, backscattered electrons (BSE) have the information about the atomic number and surface topology because they interact with the nucleus of the atom. The atoms with larger nuclei will yield high BSE. Auger electrons are used for surface elemental composition and the X-rays have information about the elemental composition of the bulk of the sample. The SE and BSE are used to image the sample and the X-rays and Auger are normally used for spectroscopy.

3.5.5a. *Energy-dispersive X-ray spectroscopy*

It is a technique used for the elemental composition of materials. It is based on the principle that when an inner core electron is knocked out by electron beam interaction with the sample, an electron from the higher energy level jumps to the lower level to occupy the inner shell electron space and releases energy, which corresponds to the energy difference between the two energy levels. The characteristics X-rays of the element is also a form of this energy and is shown schematically in Fig.3.6. Every element emits a specific characteristic X-rays and can be used to identify which specific element is actually present in the specimen. A particular area or spot of a specimen is selected for EDAX analysis.

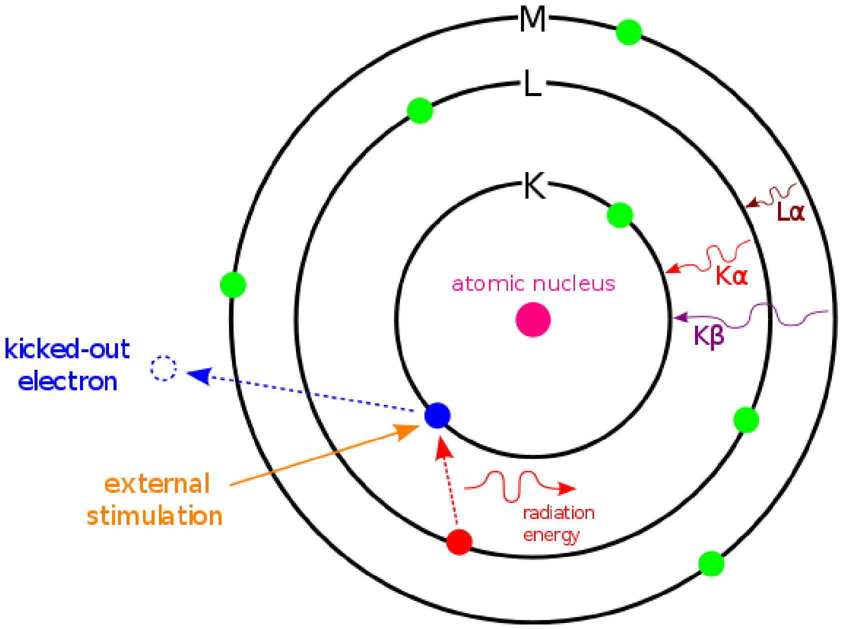

Fig. 3.6. SCHEMATIC DIAGRAM OF THE EDAX PHENOMENON.

The X-rays emitted from the selected area are analyzed through energy dispersive spectrometer for different energies. When an X-ray photon strikes the lithium-drifted silicon detector it generates photoelectrons. This causes an electron hole pair in the reverse biased diode and is converted to voltage pulse by a charge sensing amplifier. The pulse is then analyzed through a multichannel analyzer and is sent to the computer. The software then displays the peak after identification and quantifications.

3.5.5b. *Sample Preparation*

Powder samples of nanoparticles are studied by FESEM. The surface of the samples has been stubbed using the double-side adhesive carbon tape. Samples are coated with the help of good coater (HITACHI S-4700 with resolution 3.5 nm) and deposited with thin layer gold (heavy metal) on the sample. The specimen is now ready for SEM+EDAX observation.

3.5.5c. *Instrument Details*

The morphological studies of the products were recorded from Sastra University, Thanjavur, Tamil Nadu, India, using JSM-6701F field emission scanning electron microscope and FESEM instrument model number ZEISS SUPRA 40 VP SEM from Sathyabama University, Chennai, Tamil Nadu, India. Also the EDAX analysis was done from the same instrument respectively.

3.5.6. FIELD EMISSION-TRANSMISSION ELECTRON MICROSCOPE (FETEM)

The principle of operation of transmission electron microscope is the same as that of the optical microscope, but here a beam of electrons is used instead of light. Electron microscope has a very high resolution than the optical microscope, because of the very short wave length of electrons. Resolution of a microscope is different from the magnification in a sense that it the beam property, while magnification corresponds to the power of lens. It is based on de Broglie’s hypothesis, which states that the wavelength is inversely proportional to momentum. For higher resolution the wavelength needs to be very short. Resolution is the power of microscope that enables an operator to see the fine details separately. The resolution of an optical microscope estimated from Abbe's equation,

$$d = \frac{0.62\lambda}{2n \operatorname{Sin} \theta} \qquad \rightarrow (3.4)$$

Where d is the separation between two different objects, n is the refractive index of the medium, λ is the wavelength and θ is the half angle of the cone of light from specimen plane accepted by the objective. Equation (3.4) can be extended for TEM using de Broglie's hypothesis as,

$$\lambda = \frac{h}{mv} \qquad \rightarrow (3.5)$$

Where, h is the Plank's constant, m is the mass of an electron and v is the velocity of an electron. The schematic diagram of FETEM is shown in Fig.3.7.

3.5.6a. *Sample Preparation*

Samples for FETEM were prepared by making a clear dispersion of the nanocrystals in water and patting a drop of the solution on a carbon-coated copper grid. The solution was allowed to evaporate leaving behind the nanocrystals on the carbon grid.

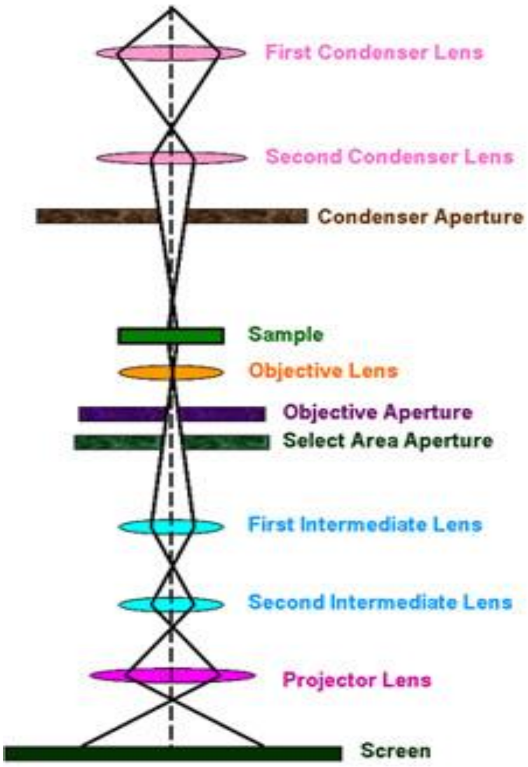

Fig. 3.7. **SCHEMATIC DIAGRAM OF TRANSMISSION ELECTRON MICROSCOPE (TEM)**

3.5.6 b.*Instrument details*

The morphological studies of the products were recorded from Sastra University, Thanjavur, Tamil Nadu, India, using JSM-2100F JEOI field emission transmission electron microscope (FETEM).

3.5.7. CYCLIC VOLTAMMETRY

Voltammetric measurements are carried out using an electrochemical cell made up of three electrodes immersed in a solution containing the analytical and an excess of a nonreactive electrolyte called the supporting electrolyte. One of the three electrodes is the working electrode, which is typically made of platinum, gold, silver, glassy carbon, nickel, or palladium. The redox process occurs at this electrode. Its dimensions are kept small in order to enhance its tendency to become polarized. The second electrode is the reference electrode, which provides calibration for the applied potential. Examples of commonly used references are the normal hydrogen electrode, Ag/AgCl electrode, and calomel electrode (i.e., Hg/Hg_2C_{l2}). The third electrode is the counter electrode, which is often a platinum wire that simply serves to conduct electricity from the signal source through the solution to the other electrodes. An example of a voltammetry setup is shown in Fig.3.8.

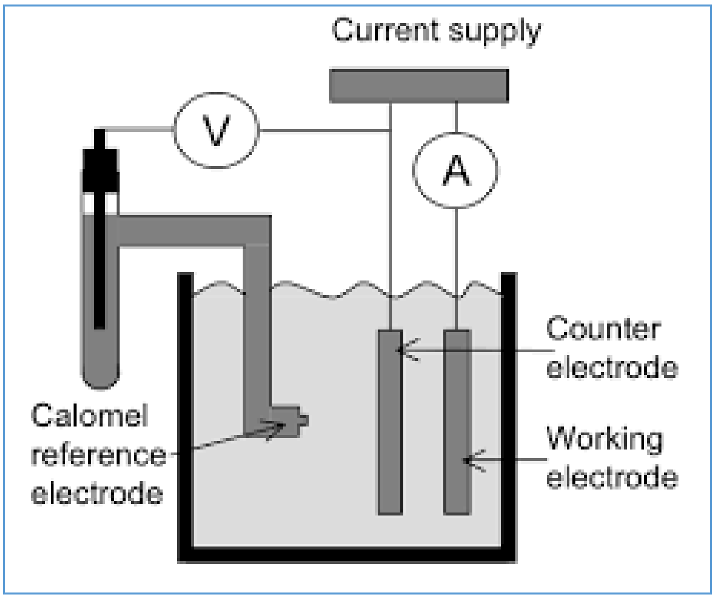

Fig. 3.8. CYCLIC VOLTAMMETRY EXPERIMENT SETUP

Note that in absence of any redox processes, the electrodes behave like capacitor plates, which polarize the ions in the solution. This results in a small, but measurable, capacitive current in the system.

3.5.7a.*Electrochemical performance investigation*

Electrochemical measurements were carried out in 0.2 M tetra butyl ammonium per chlorate aqueous electrolyte using a three electrode system. The NiO was employed as the working electrode (WE), a platinum wire counter electrode (CE), and an Ag/AgCl reference electrode (RE). Cyclic voltammetry (CV) measurements were performed within a potential range of - 0.6 to + 1.8 V versus Ag/AgCl at a scan rate from 10 to 50 mV/s on the Versa STAT MC electrochemical workstation.

The specific capacitance (Cs, Fg^{-1}) was calculated from the cyclic voltammograms according to the following equation

$$Cs = \frac{Q}{\Delta v.m} \quad \rightarrow (3.6)$$

Where, Cs denotes the specific capacitance, Q represents the anodic and cathodic charges on each scanning, m is the mass of the electrode material (mg) and Δv is the scan rate (mVs^{-1}).

3.5.7b. *Instrument details*

The cyclic voltammetry curves of the samples were recorded with a VersaSTAT MC, which is available at Instrumentation Centre, St. Joseeph‟s College, Tiruchirapalli, Tamilnadu, India.

3.5.8. X-RAY PHOTOELECTRON SPECTROSCOPY (XPS)

XPS is a spectroscopic technique that is used to measure the elemental composition and chemical state of elements. The working principle of this technique is based on the principle of photoelectric effect. A material is irradiated by a beam of X-rays, which causes to eject a core electron from the sample atom. The energy of a core level electron is a function of its binding energy which is different for different elements and helps identify the elemental composition in a sample up to the depth of 1 to 10 nm. The binding energy of an atom depends upon the formal oxidation state and the chemical environment. The higher oxidation state of an atom will shift the photoemission peak towards a higher binding energy side because of the smaller ionic radii, which gives rise to a higher coulomb attraction between the nucleus and the surrounding electrons.

The binding energy of a photo emitted electron can be represented mathematically as,

E_B=hυ-$E_{k.E}$-Φ → (3.7)

Φ= E_f - E_v → (3.8)

Where, E_B is the binding energy of a photoelectron, hυ is the energy of the incident X-ray beam, E_{kE} is the kinetic energy of the photo emitted electron and ϕ is the work function of the spectrometer. The core level photoemission peak corresponding to certain element can be grouped into three categories.

i): the peak corresponding to the core level,

ii): the Augur transition and

iii): the valance level transition at low energies.

The emission of photoelectron is shown schematically as in Fig.3.9.

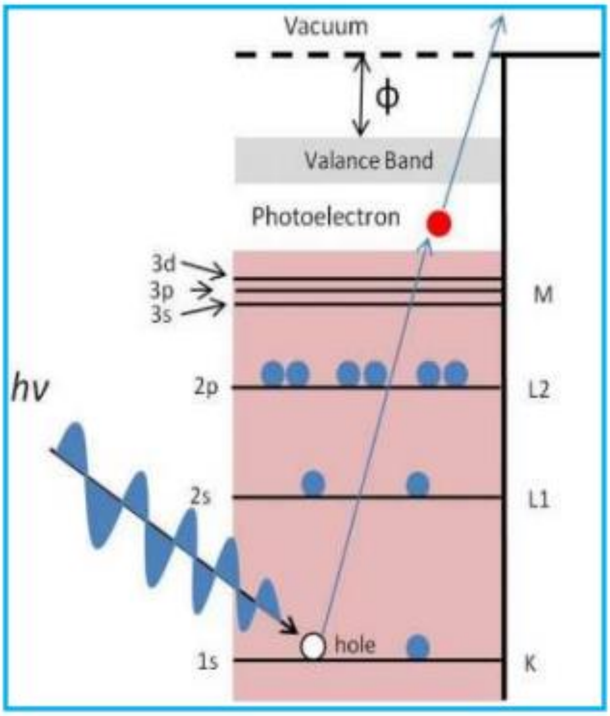

Fig. 3.9.SCHEMATIC DIAGRAM OF THE PHOTOELECTRIC EFFECT

The XPS system consists of a vacuum chamber with a sample stage, electron energy analyzer and X-ray source. The X-ray source used in this study is the AlKα. XPS is operated in ultra-high vacuum (UHV) of the order of 10^{-8} to 10^{-10} mbar to obtain high signal to noise ratio. Additionally a low vacuum also causes a monolayer deposition on the surface of the sample. The fact that XPS is a surface technique with a depth resolution of up to 10 nm for AlKα source clearly requires a UHV system. To characterize a sample through XPS the sample is first cleaned through Ar ions sputtering to remove the adsorbents like amorphous carbon from the sample surface. After proper cleaning, the sample is further characterized in two steps. First a broad survey spectrum is taken and then the detected desired elements are characterized through the core level spectra. All the spectra are scanned from 30 to 50 times to improve the signal to noise ratio. After that the peaks are corrected with respect to the carbon peak at 284.6 eV. The schematic diagram of XPS instrument is shown in Fig.3.10.

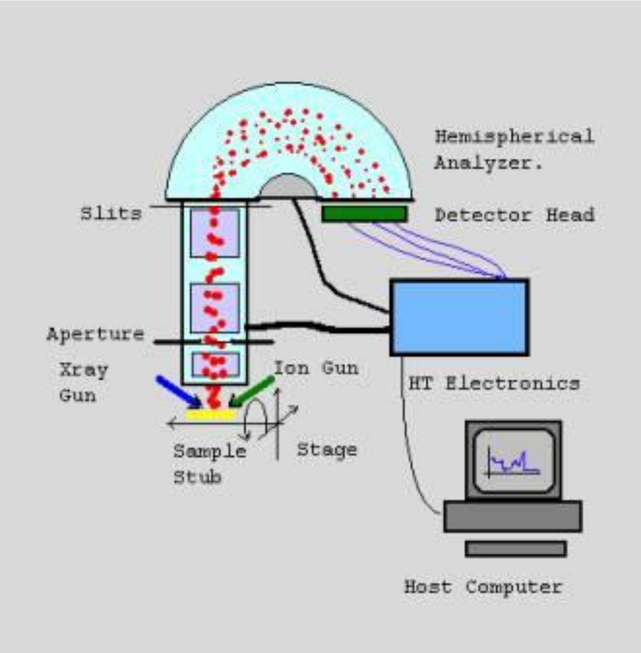

Fig. 3.10. XPS INSTRUMENT SETUP

3.5.8a. *Sample Preparation*

Approximately 50 mm x 50 mm squares of indium were pressed onto a metal slide. Around 10 μg of each synthesized sample powder was pressed down into the indium substrate and the excess powder was dusted off. The slide was then placed into the sample chamber.

3.5.8b. *Instrument details*

The elemental composition and chemical state of elements of the products were recorded from Sastra University, Thanjavur, Tamil Nadu, India, using ESCLAB MKII, Thermo Fisher Scientific Inc., K-Alpha, USA.

CHAPTER – IV

Preparation and Characterization of Nickel Ferrite Nano Particles by Co-Precipitation Method with Citrate as Chelating Agent

4.1. Introduction

The materials in nanoscale range are of great importance in the areas of both fundamental and advanced research because of their outstanding physical and chemical applications. In which ferrite nanoparticles have found major attention because of their excellent electrical, magnetic, microwave devices, drug delivery systems and gas sensors [Han *et al.*, (1996); Goldman *et al.*, (2006); Pileni, (2001); Maqusood ahameda *et al.*, (2011)]. In recent days energy shortages increase several fold resulting in the need for suitable storage materials to fulfil future requirement. To overcome this supercapacitors found major attraction for the researchers. Supercapacitor are being used well in various electrical devices such as electrical vehicles, backup power systems, electronic equipment's etc., because of their unique energy storing capacity [Kotz and Carlen, (2000); Liu, (2007); Xu *et al.*, (2010); Toupins *et al.*, (2005); Saliger *et al.*, (1998); Liu *et al.*, (2010); Lao *et al.*, (2006); Xu *et al.*, (2008)]. Nickel ferrite is very attractive in recent research works because of its higher electromagnetic performance, excellent chemical stability, mechanical hardness, high coercivity, and moderate saturation magnetization [Fan *et al.*, (2009); Godman *et al.*, (1995)]. $NiFe_2O_4$ is an inverse spinal ferrite and it can be described as cubic, closely packed arrangement of oxygen atoms with Ni^{2+} and Fe^{3+} ions locating in octahedral and tetrahedral sites respectively [Kooti and Afshari (2013)]. $NiFe_2O_4$ nanoparticles can be synthesized by different wet chemical methods, such as co-precipitation [Joshi *et al.*, (2014)], hydrothermal [Nejati and Zabihi, (2012)], sol gel [Penchalreddy *et al.*, (2014)], micro-emulsion [Zaki *et al.*, (2013)] spray pyrolysis [Deschanres *et al.*, (1990)], reverse micelles [Kale *et al.*, (2004)] and sono-chemical technique [Kurikka *et al.*, (1998)]. Apart from the above methods, co-precipitation method can produce ultrafine, high purity and crystalline nano particles in shortest duration [Niasari *et al.*, (2009); Maaz *et al.*, (2009); Ati *et al.*, (2013)]. In this present work nickel ferrite nano particles has been synthesised and characterized of by using simple co-precipitation method along with citric acid as a chelating agent.

4.2. RESULTS AND DISCUSSION

4.2.1. THERMO GRAVIMETRIC AND DIFFERENTIAL THERMAL ANALYSIS

To analyse the thermal behaviour of $NiFe_2O_4$ nanoparticles, TG/DTA curves has been recorded for the as-synthesized products in the temperature range of 35 °C to 850 °C were performed with an increment of 20 °C/min in the nitrogen atmosphere. Fig.4.1 depicts the TG/DT analysis of $NiFe_2O_4$ nanoparticles.

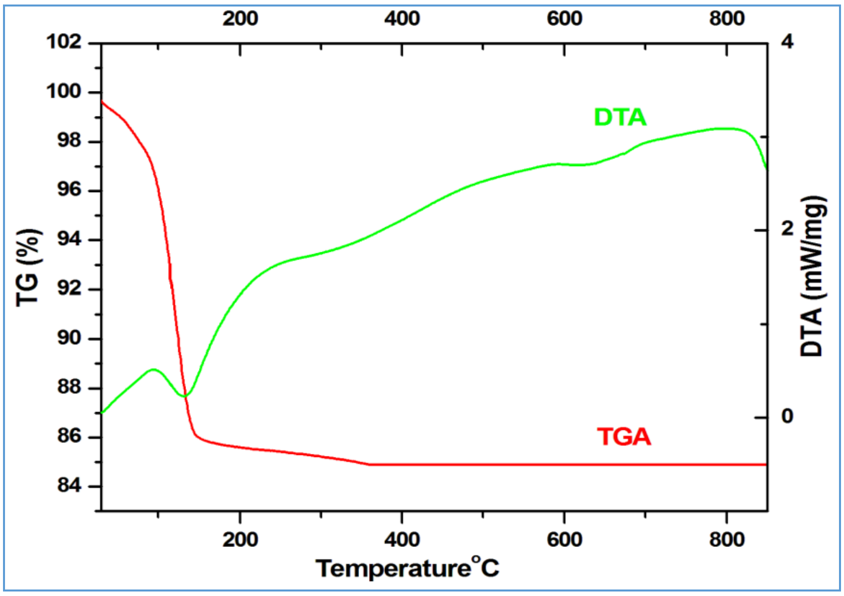

Fig. 4.1. TG/DT ANALYSIS OF $NiFe_2O_4$ NANO PARTICLES

Three major weight losses have been observed from the TG analysis in the range from 35 °C to 850 °C. The first stage of weight loss is observed at a temperature below 77 °C is 2% due to desorption of water. The second weight loss is predicted in the range from 77 °C to 144 °C is 12% as a result of decomposition of organic templates. The final weight loss of 1% is observed between 144 °C and 362 °C due to crystallization of the final product. No weight loss is found beyond 362 °C indicating the formation of $NiFe_2O_4$ nano particles. Liu *et al.*, (2013) have reported that no considerable weight loss has been noticed beyond 350 °C indicating the formation of pure $NiFe_2O_4$ nano particles.The DTA curve shows a broad endothermic peak at 129 °C due to dehydration. After dehydration, three stages of the decomposition of anhydrous precursor are observed i.e., evolution of CO occurs up to 228 °C resulting in the formation of the acetone di-carboxylate complex $Ni_3Fe_6O_4$ $(C_5H_6O_6)_8$. The next stage resembles to the evolution of acetone, CO_2 and it takes place up to 295 °C.

The residue at this step possibly has a structure related to the nickel ferrite with trapped CO_2, $Ni_3Fe_6O_{12}$ $(CO_2)_3$. Similar result was reported by Nikolic *et al.*, (2013) for the synthesis of nickel ferrite nanoparticles. Decomposition of the $Ni_3Fe_6O_{12}$ $(CO_2)_3$ up to 360°C exposes the formation of the $NiFe_2O_4$. The exothermic peak at 357 °C in DTA curve corresponding to TGA curve at 362 °C confirms the formation $NiFe_2O_4$ nanoparticles**.** Dongen Zhang *et al.*, (2009) have reported that the pure nickel ferrite nano particles formed above 385 °C which is in line with our obtained result.

4.2.2. FUNCTIONAL GROUP ANALYSIS

FTIR spectra of $NiFe_2O_4$ nanoparticles at 400 °C, 600 °C and 800 °C were recorded in the range of 4000 cm^{-1} to 400 cm^{-1} and presented in the Fig.4.2.

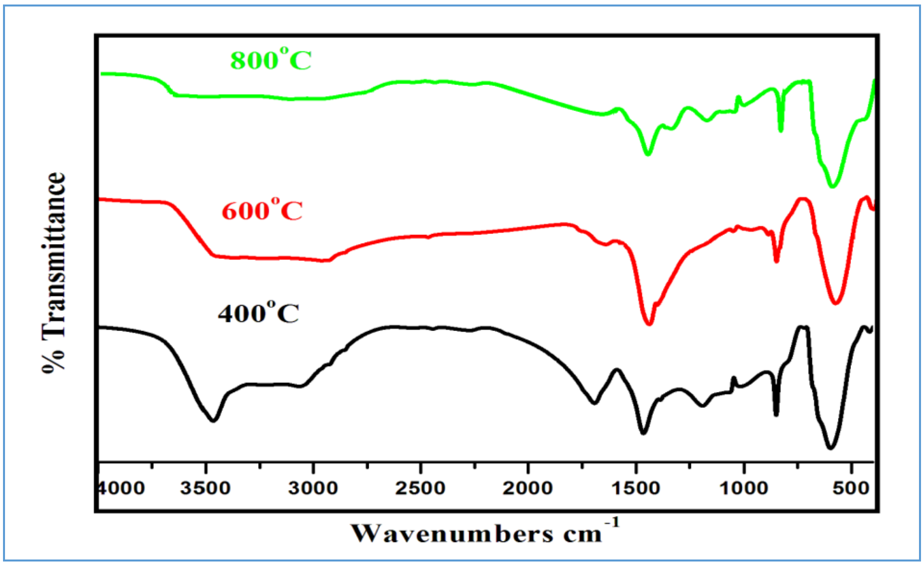

Fig.4.2. FTIR SPECTRA of $NiFe_2O_4$ NANO PARTICLES CALCINATED AT DIFFERENT TEMPERATURES 400 °C, 600 °C AND 800 °C

There are two main broad metal-oxygen bands are seen mainly in the FTIR spectra of all spinels, and ferrites in particular. FTIR spectra have two absorption bands between the region 400–600 cm^{-1}, which corresponds to the octahedral and tetrahedral sites of $NiFe_2O_4$, respectively [Gotic *et al.*, (1998)]. In which the higher absorption band around 590 cm^{-1} corresponds to the stretching vibrations of tetrahedral complexes Fe-O and the lower absorption band around 410 cm^{-1} is attributed to the vibrations of octahedral groups Fe-O [Liu *et al.*, (2013)].

The different values of absorption position for octahedral and tetrahedral site of $NiFe_2O_4$ nanoparticles are due to the different values of Fe^{3+} to O^{2-} distance for octahedral and tetrahedral sites [Haowen Liu *et al.*, (2013)]. The absorption bands presented around 3400 cm^{-1} in all the samples could be due to the hydrogen bonded hydroxyl group. The other two bands occurring around 2960–2854 cm^{-1} are assigned to the anti-symmetric and symmetric CH_2-vibrations of the carbon chains, respectively, and the absorption band at around 1464 cm^{-1} corresponds to the CH_2-bending vibration [Manish Srivastava *et al.*, (2009)].

4.2.3. STRUCTURAL ANALYSIS

The XRD pattern of as-synthesized and calcinated $NiFe_2O_4$ nanoparticles at 400 °C, 600 °C and 800 °C are shown in the Fig.4.3.

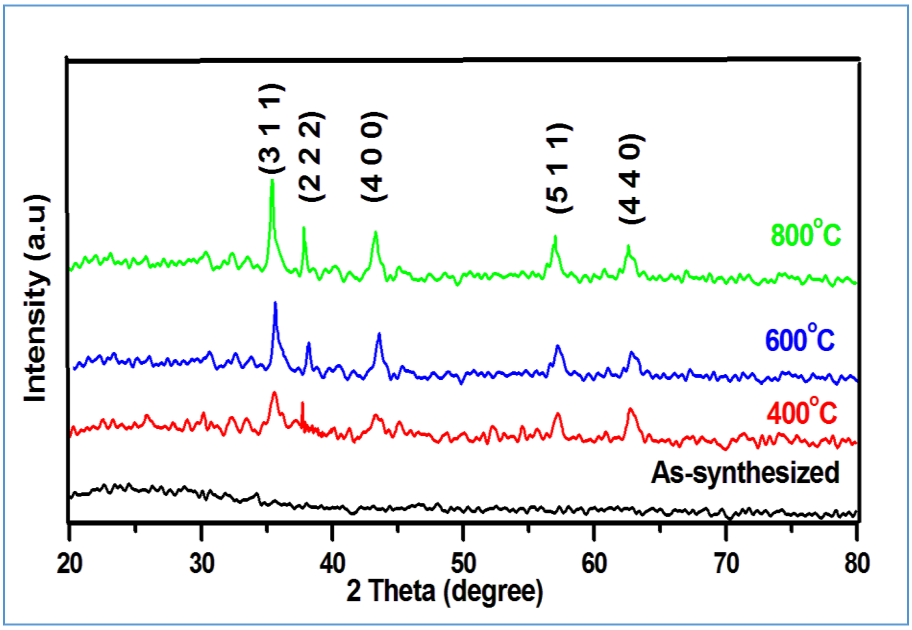

Fig. 4.3. XRD SPECTRA of $NiFe_2O_4$ NANO PARTICLES AS-SYNTHESIZED AND CALCINATED AT DIFFERENT TEMPERATURES

As-synthesized sample doesn't show any peaks and indicate that calcination is necessary to stabilizing the particle size and preventing their agglomeration [Karakaş *et al.*, (2015)]. The XRD pattern of all calcinated samples exhibit the reflections with hkl values of (311), (222), (400), (440) and (511) planes indicate the cubic phase [NaCao *et al.*, (2015)] with space group Fd3m [Joshi *et al.*, (2014)]. The obtained XRD peaks are well matched with the standard characteristics peaks of the cubic spinel lattice of $NiFe_2O_4$ reported in JCPDS card no # 86-2267 [Jiang *et al.*, (2008)]. The observed peaks in the present study clearly indicate the formation of nickel ferrite nanoparticles without any impurities [Zhao *et al.*, (2007)]. The peaks becoming sharper and narrower with increase in intensity has been observed with increasing calcination temperature from 400 °C to 600 °C and 600 °C to 800 °C shows the improvement of crystallite size with heat treatment [Prabhakaran and Hemalatha (2014)]. The average particle size has been calculated using Debye Scherer's formula and it is shown in table 5.The particle size increases with increasing temperatures are observed in the present study indicate the growth of the nickel ferrite nanoparticles. Similar conclusion was drawn by Zhang *et al.*, (2012) for the preparation of nickel ferrite nanoparticles by solid state reaction. Lattice parameter "a" can be calculated by using the relation $a= d_{hkl} (h^2+k^2+l^2)^{1/2}$ and it is shown in table 5. From XRD study in the present study suggest that $NiFe_2O_4$ nanoparticles calcinated at 600 °C is suitable for further analysis.

TABLE 5: PARTICLE SIZE AND LATTICE PARAMETER OF $NiFe_2O_4$ NANO PARTICLES

TEMPERATURE(°C)	Particle Size(nm)	Lattice Parameter(a)Å
400	16	8.375
600	23	8.377
800	31	8.378

The increase in trend for lattice constant with the increase of calcination temperature is found it may be due to some structural changes accompanied the formation of nickel ferrite. These changes may be owing to the rearrangement of the ions in the ferrite lattice (tetrahedral or octahedral sites). Hessien *et al.,* (2013) have reported that the annealing temperature strongly affects the lattice parameter in which an increase in trend of lattice parameter is found with increase of temperature owing to rearrangement of the ions in the ferrite lattice (tetrahedral or octahedral sites) and this will directly influence the magnetic performance of the ferrite.

4.2.4. FIELD EMISSION SCANNING ELECTRON MICROSCOPE (FESEM) WITH EDAX

The surface morphology and microstructures of the synthesized powder calcinated at 600 °C are thoroughly studied through FESEM analysis. The FESEM images of nickel ferrite are shown in Fig.4.4 (a) and (b).

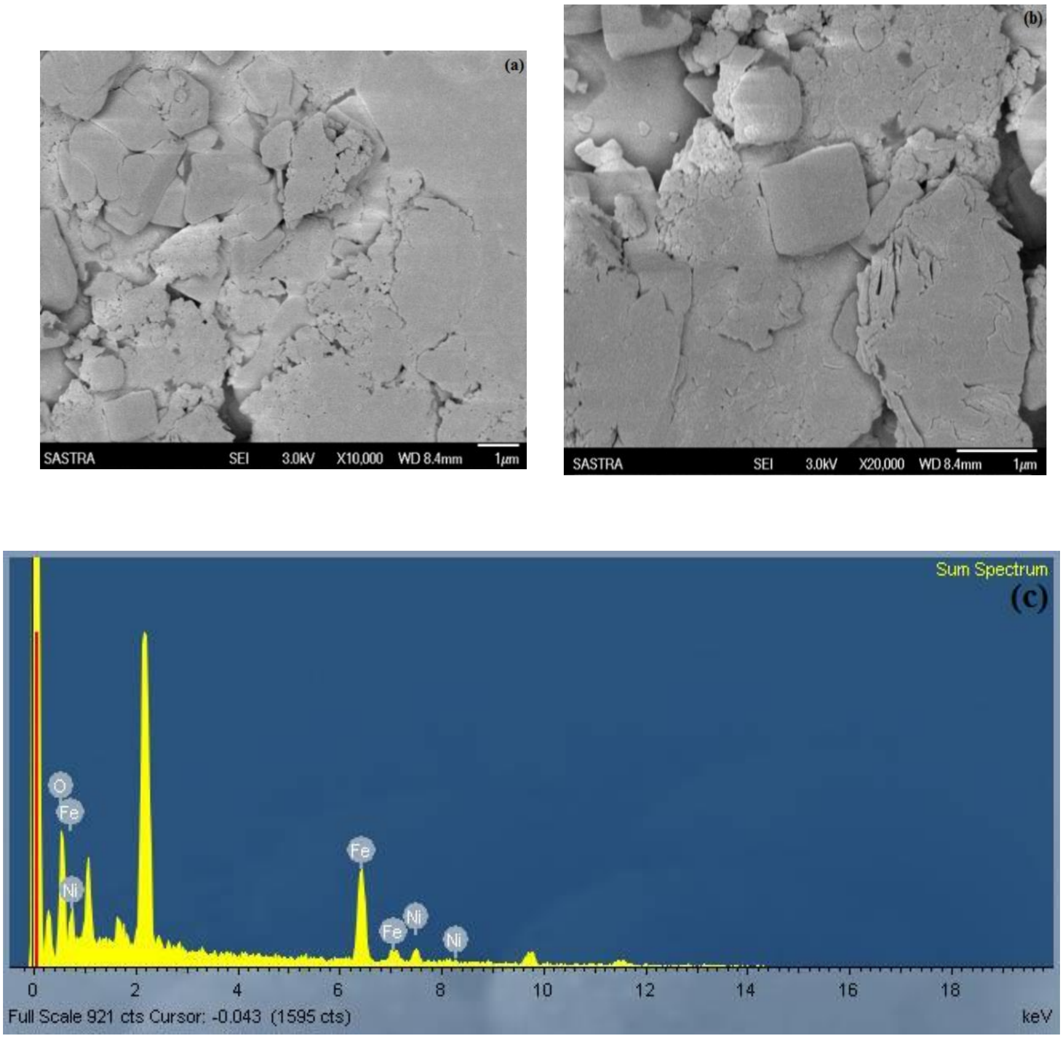

Fig. 4.4. (a), (b) FESEM IMAGE of $NiFe_2O_4$ NANO PARTICLES CALCINATED at 600 °C with DIFFERENT MAGNIFICATIONS AND (c) the CORRESPONDING EDAX

FESEM image clearly shows nickel ferrite nanoparticles are of cubic shape with particle size ranges from 22 to 30nm. The elemental composition of nickel ferrite has been investigated with the help of EDAX analysis. From the EDAX spectrum, numerous well defined peaks were predicted to Ni, Fe and O which clearly indicate that the synthesized particles as nickel ferrite. Karakaş *et al*., (2015) have also reported a similar result regarding the nickel ferrite sample contains Fe, Ni and O elements only without any other impurities. No impurities are detected except the extra gold peak is shown in Fig.4.4 (c). The presence of gold peak is due to the thin coating on the sample surface to make it conducting, which is required to record the FESEM.

4.2.5. Field Emission Transmission Electron Microscope (FETEM) with SAED

The $NiFe_2O_4$ nanoparticles calcinated at 600 °C with different scale bar (5nm and 10nm is shown in Fig.4.5 (a) and (b).

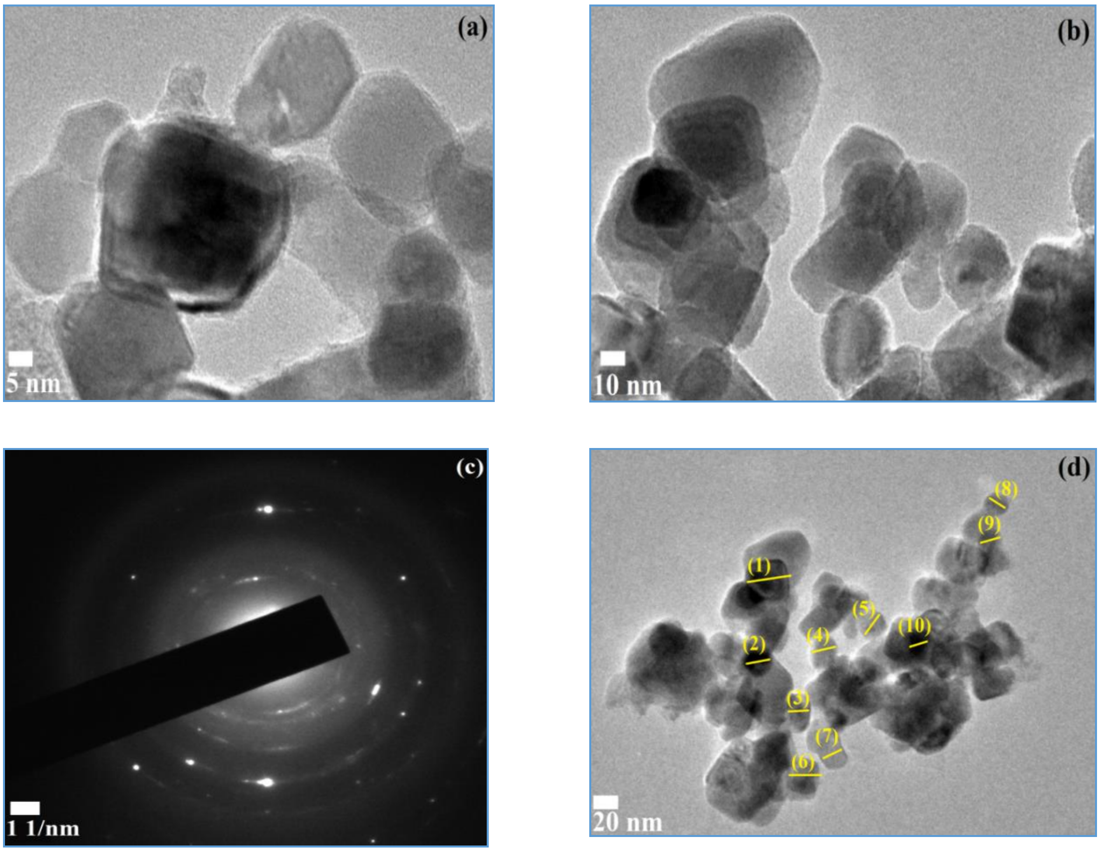

Fig. 4.5. (a), (b) FETEM of $NiFe_2O_4$ nano particles calcinated at 600 °C with different magnification also (c) Corresponding SAED and (d) Particle size measured using image J viewer software

The image reveals that the synthesized $NiFe_2O_4$ nanoparticles are cubic in shape with some agglomeration. Some degree of agglomeration between nanoparticles is understood due to the nanoparticles calcinated at high temperature. The maximum particle size estimated from the micrograph is around 36 nm. The SAED pattern of the cubic shaped $NiFe_2O_4$ nanoparticles is shown in Fig.4.5 (c). All spots are identified as the diffractions from cubic $NiFe_2O_4$, which reveals the crystalline nature of $NiFe_2O_4$ nanostructure. The length of the individual selected particles is shown in Fig.4.5 (d) and graph 1 using the "Image J viewer software" [Loganathan *et al.,* (2015)] and its average particle size of 23nm observed in FETEM analysis closely agree with the XRD result. Nejati and Zabihi (2012) have reported cubic-like morphology for nickel ferrite nanoparticles synthesized by hydrothermal method.

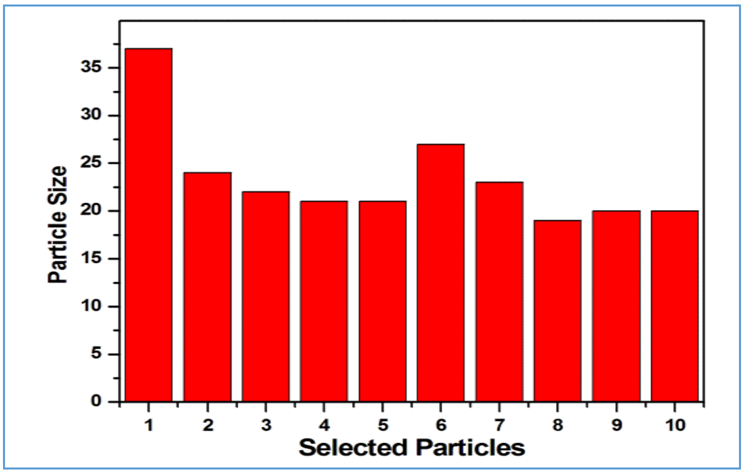

GRAPH.1 AVERAGE PARTICLE SIZE of $NiFe_2O_4$ NANOPARTICLES USING IMAGE J VIEWER SOFTWARE FROM FETEM

4.2.6: CYCLIC VOLTAMMETRY (CV)

The CV curves of nickel ferrite nanoparticles of 600 °C at various scan rates such as 2, 3, 5, 10, 20, 30, 50 and 100 mVs^{-1} is shown in Fig. 4.6

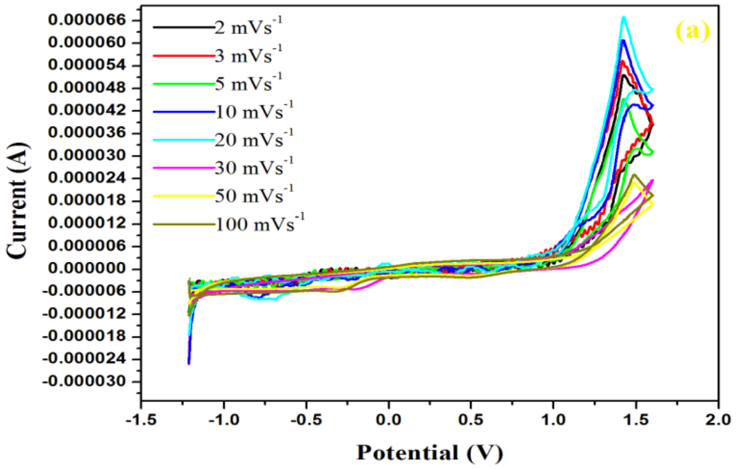

Fig. 4.6. (a) CV PATTERNS OF $NiFe_2O_4$ NANO PARTICLES CALCINATED AT 600 °C FOR DIFFERENT SCAN RATES

The shape of the CV curves is an ideal rectangular shape observed at 2 mVs^{-1}. Further increasing the scan rate the observed pattern of the CV curve is altered and it confirms the pseudo-capacitive nature of the material. The specific capacitances (SC) values of $NiFe_2O_4$ electrode can be calculated by using the formula [Sathishkumar *et al.*, (2015)].

$$Cs = \frac{Q}{\Delta v . m}$$

Where, Cs is the specific capacitance, Q the anodic and cathodic charges on each scanning, m is the mass of the electrode material (mg) and Δv is the scan rate (mVs^{-1}). Electrochemical measurements was carried out in 0.2 M tetra butyl ammonium perchlorate with a standard three electrode conFiguration consisting of a sample (working electrode), an Ag/AgCl (reference electrode) and a high platinum wire (counter electrode)[34]. The scan rate increased in the range from 2 mVs^{-1} to 100 mVs^{-1} and its corresponding specific capacitance value depicted in Fig.4.6 (b) and table 6.

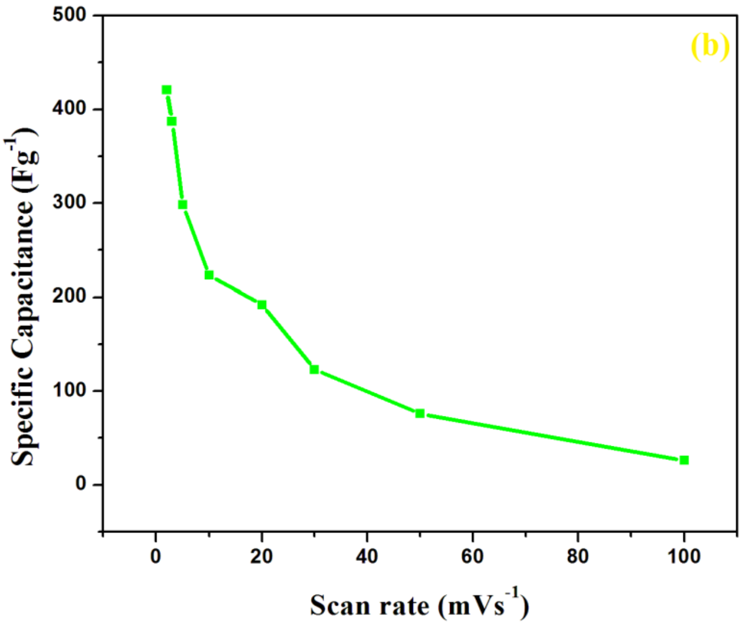

Fig. 4.6. (b) DIFFERENT SCAN RATE AND THEIR SPECIFIC CAPACITANCE VALUES

TABLE 6: THE SPECIFIC CAPACITANCE OF THE $NiFe_2O_4$ NANO PARTICLES CALCINATED AT 600 °C VS DIFFERENT SCAN RATES

Different scan rate (mVs^{-1})	**$NiFe_2O_4$ (600°C) (Fg^{-1})**

2	421
3	387
5	298
10	223
20	192
30	123
50	76
100	26

Lower specific capacitance values observed for higher scan rates indicate that the ionic diffusion takes place only for outer surfaces whereas at low scan rate the ionic diffusion takes place both inner and outer surfaces [Shahid Anwar *et al.,* (2011)]. The capacitance value 421Fg^{-1} observed at the scan rate 2 mVs^{-1} for the sample calcinated at 600 °C. This result is very much higher than the previously reported value of 251 Fg^{-1} by Pintu Sen *et al.*, 2010 for nickel ferrite sample calcinated 400 °C at the scan rate 2 mVs^{-1}. The higher specific capacitance value observed at 600 °C in the present study closely well connection with the good crystallinity of the $NiFe_2O_4$ nano particles at 600 °C by XRD analysis and it may be used for supercapacitor applications.

4.2.7. DYNAMIC LIGHT SCATTERING (DLS) AND ZETA POTENTIAL

Dynamic light scattering (DLS) is a technique that can be used to determine the size (hydro-dynamic diameter) distribution profile of small particles in suspension or polymers in solution [Gopalakrishnan *et al.,* (2015)]. In the scope of DLS, temporal fluctuations are usually examined by means of the intensity or photon auto-correlation function (also known as photon correlation spectroscopy or quasi-elastic light scattering). Size distribution of the $NiFe_2O_4$nanoparticles calcinated at 600 °C of pH 8 is shown in Fig.4.7 (a). The Z-average value for the $NiFe_2O_4$ nano particle is 205.9 nm. This greater size is due to insolubility and aggregation of the sample in water. Fig.4.7 (b) shows the zeta potential of $NiFe_2O_4$nanoparticles calcinated at 600 °C.

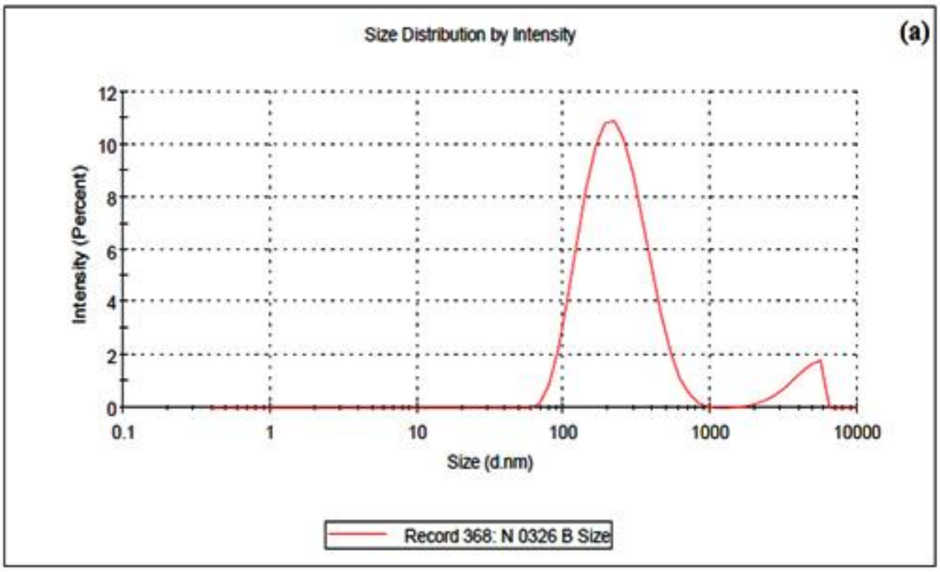

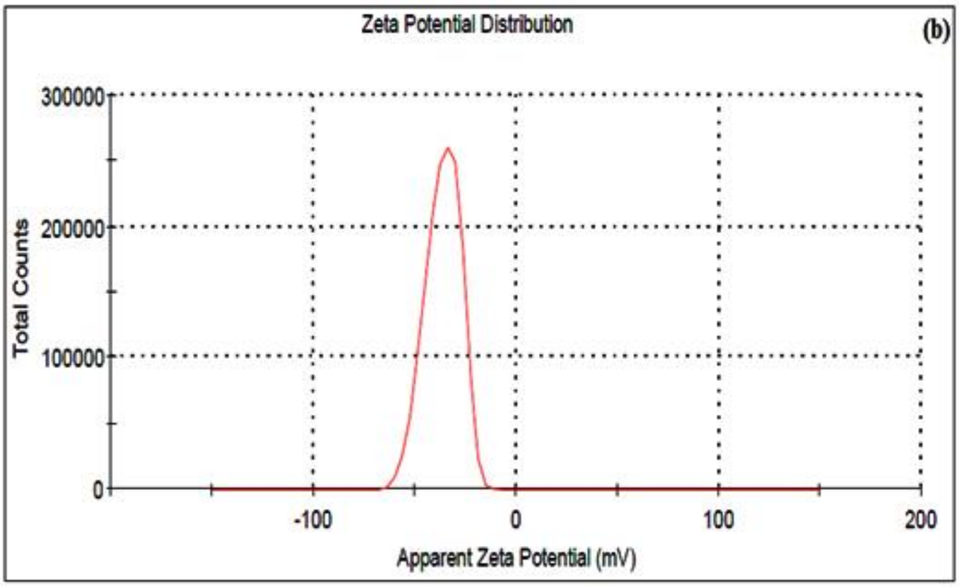

Fig. 4.7 (a) ZETA SIZER AND (b) ZETA POTENTIAL OF $NiFe_2O_4$ NANO PARTICLES CALCINATED AT 600 °C

The stability of the $NiFe_2O_4$ nanoparticles is determined using a zeta potentiometer. The magnitude of the zeta potential gives an indication of the potential stability and surface charge of the synthesized $NiFe_2O_4$ nanoparticles. The result of the Zeta potential and Zeta deviation are -36.1 mV and 8.32 mV respectively and it reveals the good stability of synthesized $NiFe_2O_4$nanoparticles. The obtained zeta potential is higher than the previously reported value of -30 mV by Bhosale *et al.,* (2015) observed for nickel ferrite nanoparticles.

4.2.8. X-RAY PHOTOELECTRON SPECTROSCOPY (XPS)

X-ray photoelectron spectroscopy (XPS) is a surface-sensitive assessable spectroscopic technique that processes the elemental composition at the electronic state of the elements that exist within a material. XPS spectra are attained by irradiating a material with a beam of rays while simultaneously determining the kinetic energy and number of electrons that escape from the top 0 to 10 nm of the material being studied. Generally in transition metal compounds there exist multiple oxidation states simultaneously [Biesinger *et al.,* (2009)]. Fig.4.8 (a) depicts the Fe2p peak fixed around 708.3 eV resembles to Fe^{2+}.

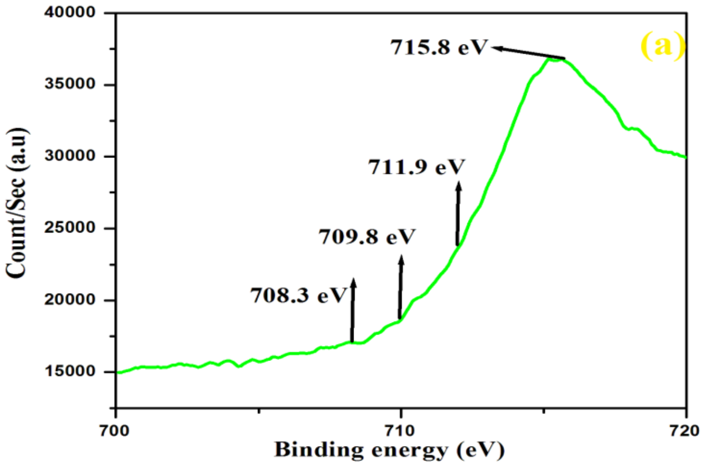

Fig. 4. 8. (a) XPS SPECTRA OF FE FOR $NiFe_2O_4$ NANO PARTICLES CALCINATED AT 600 °C

The peak around 709.8 and 711.9 eV are fixed to Fe^{3+} at octahedral and tetrahedral sites respectively.In addition a satellite peak observed at a binding energy of around 715.8 eV [Tudorache *et al.,* (2013)]. Fig.4.8 (b) illustrates the XPS spectra of Ni 2p region of nickel.

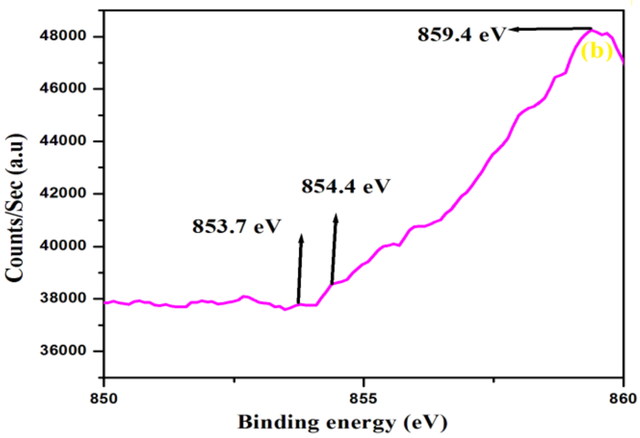

Fig. 4. 8. (b) XPS SPECTRA NI FOR $NiFe_2O_4$ NANO PARTICLES CALCINATED AT 600 °C

The spectra contain a main binding energy peak at 853.7 eV and a shoulder at 854.4 eV assigned to Ni^{2+} and Ni^{3+} respectively. Also a satellite peak was obtained around 859.4 eV [Mcintyre *et al.*, (1997)].

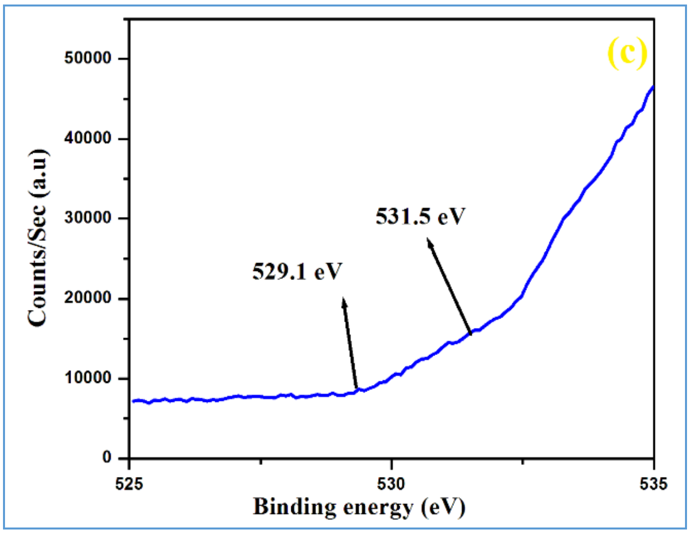

Fig. 4. 8. (c) XPS SPECTRA OF O FOR $NiFe_2O_4$ NANO PARTICLES CALCINATED AT 600 °C

Fig.4.8(c) shows the O1s photo electron spectra of the sample, the dominant photoelectron peak around at 529.1 eV is the influence from the crystal lattice Oxide ion (O^{2-}), while the shoulder signifies non-stoichiometry which results due to photoelectron ejected from oxide ion in the vicinity of such defects and suffers from excess loss in kinetic energy resulting in higher binding energy [Tan *et al.*, (1991)]. Besides, the higher binding energy peak at 531.5 eV may be attributed to surface defects or chemisorbed oxygen species (–OH) [Carley *et al.,* (1983)]. From the XPS analysis it may conclude that the $NiFe_2O_4$ nanoparticles have exist in multiple oxidation states.

4.3. CONCLUSION

Nanosized $NiFe_2O_4$ materials were prepared by a simple high yielding and low-cost co-precipitation method. Structural, compositional and capacitive behaviour of the synthesized products were well studied. XRD study reveals the resultant product was $NiFe_2O_4$ nanoparticles and the particle size varied with the calcinated temperature. No weight loss was noticed from 362 °C in TGA and exothermic peak at 357 °C in DTA study confirmed the formation of $NiFe_2O_4$. FTIR analysis confirmed that the synthesized sample as $NiFe_2O_4$ nanoparticles. FESEM and FETEM images reveal that the particles were in cubic shape. EDAX confirmed the elemental composition of $NiFe_2O_4$ nanoparticles were Fe, Ni and O. The particle size observed from FETEM analysis agrees well with the particle size calculated from XRD. The zeta potential value revealed that the synthesized nickel ferrite nano particles have good stability. From CV study, higher capacitance value of 421 Fg^{-1} was observed for $NiFe_2O_4$ nanoparticles calcinated at 600 °C suggested for super capacitance application. The XPS analysis confirmed the synthesized $NiFe_2O_4$ nanoparticles have exist in multiple oxidation states.

CHAPTER –V

Preparation and Characterization of nanosized cobalt ferrite particles by co-precipitation method with citrate as chelating agent

5.1. Introduction

In recent years, synthesizing nanosized materials is an attractive and challenging area of research for industrial applications. All the applications need energy to process the input and achieve a desired output. On the other hand storing this energy is always a big challenge. To overcome this problem electrochemical energy storage systems is an appropriate one i.e., batteries, supercapacitors etc. The batteries distribute high energy density and low power density whereas, conventional capacitors deliver high power density and low energy density. Supercapacitor is main attraction because it can afford high-power density, high-rate capability, and long cycle life [Chen, *et al.,* (2015); Lavela and Tirado, (2007)]. These supercapacitors have abundant potential applications such as power electronics, electric vehicles, computer backup and sensor etc., [Prasad and Miura, (2004)]. For which ferrite based supercapacitor found much attention in researchers. Among which cobalt ferrite plays a vital role in the area of supercapacitors [Kumbhar *et al.,* (2012)]. Cobalt ferrite not only having super capacitance application besides it is having a number of applications like microwave devices [Shanmugavani *et al.,* (2015)], recording media [Cedeno-Mattei *et al.,* (2008)], magnetic fluids [Moumen and Pileni, (1996)], gas sensors [Sathitwitayakul *et al.,* (2012)] and catalysts [Kooti *et al.,* (2012)]. $CoFe_2O_4$ nanoparticles can be easily synthesized by various chemical methods, such as co-precipitation [Surendra *et al.,* (2011)], hydrothermal [Allaedini *et al.,* (2015)], sol gel [Sajjia *et al.,* (2014)], micro-emulsion [Katalin Sinko *et al.,* (2012)] spray pyrolysis [Patrushera *et al.,* (2014)], reverse micelles [Ibrahim Sharifi *et al.,* (2012)] and sono-chemical technique [Shafi *et al.,* (1998)]. Co-precipitation method has the advantage of producing ultrafine, high purity and crystalline nano particles in shortest duration than other methods [Liu *et al.,* (2008); Kima *et al.,* (2003)]. In the present work an attempt is made to synthesis and characterization of cobalt ferrite nano particles by using simple co-precipitation method along with citric acid as a chelating agent.

5.2. RESULTS AND DISCUSSION

5.2.1. THERMO GRAVIMETRIC AND DIFFERENTIAL THERMAL ANALYSIS

To analyse the thermal behaviour of $CoFe_2O_4$ nanoparticles, TG/DTA curves has been recorded for the as-synthesized products in the temperature range of 35 °C to 850 °C were performed with an increment of 20 °C/min in the nitrogen atmosphere. Fig.5.1 depicts the TGA and DTA curves of as-synthesized $CoFe_2O_4$ nanoparticles.

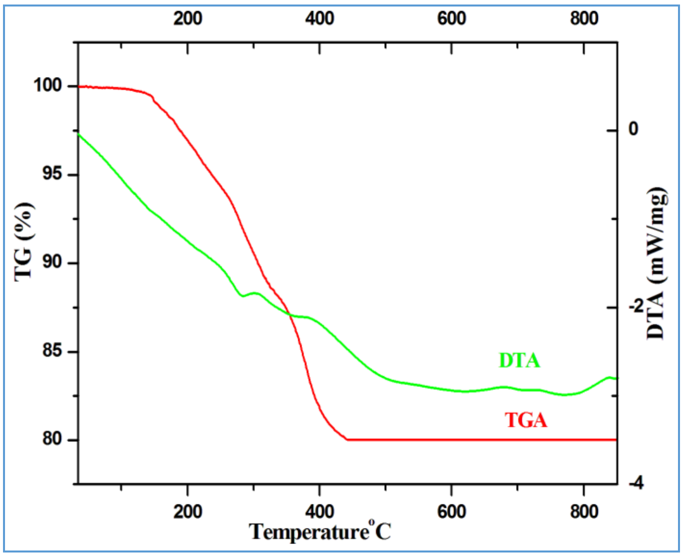

Fig. 5.1. TGA/DTA ANALYSIS OF $CoFe_2O_4$ NANO PARTICLES

From the TG analysis it has been observed three major weight losses in the range from 35 °C to 850 °C. The first stage of weight loss of 2% is detected at a temperature less than 130 °C due to desorption of water. The second weight loss of 6% is predicted in the range starting from 130 °C to 284 °C as a result of decomposition of organic templates. The final major weight loss 12% is observed between 284 °C and 432 °C due to crystallization of the final product. No weight loss is found beyond 432 °C representing the formation of pure $CoFe_2O_4$ nano particles. Velho-Pereira *et al.,* (2015) have reported no weight loss was observed beyond 421 °C indicating the formation of pure cobalt ferrite nanoparticles. The DTA curve displays a small endothermic peak at 129 °C due to dehydration. The exothermic peak at 282 °C is attributed owing to the decomposition of nitrates and initiates the formation of cobalt ferrite crystallization [Salunkhe *et al.,* (2012)]. After dehydration, the anhydrous precursor experiences decomposition to yield cobalt ferrite. The endothermic peak at 308 °C and 383 °C corresponds to the thorough decomposition of citrate precursor to form cobalt ferrite with the simultaneous evolution of CO, CO gas and acetone molecules formed. Similar result was clearly reported by Xiao *et al.,* (2007) for the preparation of cobalt ferrite nanoparticles.

5.2.2. FUNCTIONAL GROUP ANALYSIS

The FTIR spectra were recorded in the range 400-4000 cm^{-1}. The FTIR spectra of $CoFe_2O_4$ nanoparticles calcinated 400 °C, 600 °C and 800 °C were presented in Fig.5.2.

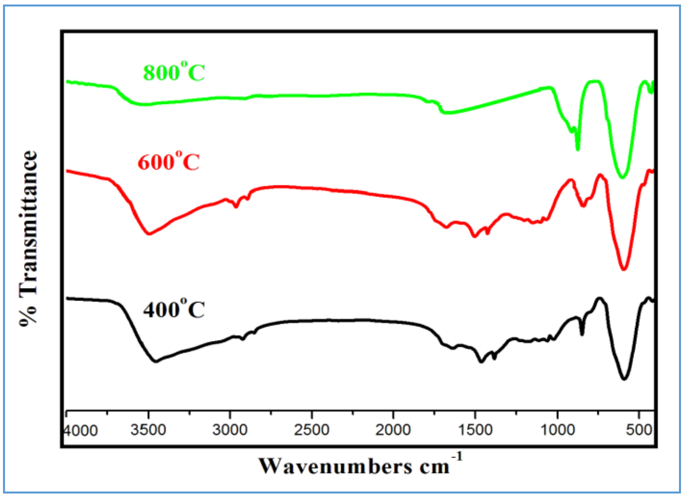

Fig. 5.2. FTIR SPECTRA OF $CoFe_2O_4$ NANO PARTICLES CALCINATED AT DIFFERENT TEMPERATURES

Two strong absorption bands are observed around at 590 and around 422 cm^{-1} for all calcinated $CoFe_2O_4$ samples. These two vibrations bands are correspond to the vibrations of octahedral and tetrahedral sites in the spinel structure, respectively [Gandhi *et al.,* (2011); Qin *et al.,* (2010)]. The existence of spinel ferrite, $CoFe_2O_4$ in a sample which had the structural properties of tetrahedron, attributed the high frequency band around 592 cm^{-1}corresponds to the stretching vibrations of tetrahedral complexes Fe-O and octahedron is fall in low frequency regions around 413 cm^{-1} attributed to the vibrations of octahedral groups Co-O [Tailhades *et al.,* (1998); Deraz and Omar, (2014)]. The different frequency between the characteristic vibrations (ν_1 and ν_2) may be attributed to the higher frequency of oxygen-metals ions in the octahedral sites and lower frequency of oxygen-metals ions in the tetrahedral sites**.** In addition a broad band around 3426 cm^{-1} which is assigned to the stretching vibrations of (O-H) hydroxyl group. Srivastava *et al*, (2009) have also reported that the stretching vibrations of hydroxyl group will occur around at 3430 cm^{-1}. The other two bands occurring around 2923–2854 cm^{-1} are assigned due to the anti-symmetric and symmetric CH_2-vibrations [Li *et al.,* 2010; Cannas *et al.*, 2010] of the carbon chains, respectively, and the absorption band around 1464 cm^{-1} corresponds to the CH_2-bending vibration [Watawe *et al*, (2015)].

5.2.3. STRUCTURAL ANALYSIS

The XRD pattern of as-synthesized and calcinated $CoFe_2O_4$ nanoparticles calcinated at 400 °C, 600 °C and 800 °C are shown in the Fig.5.3.

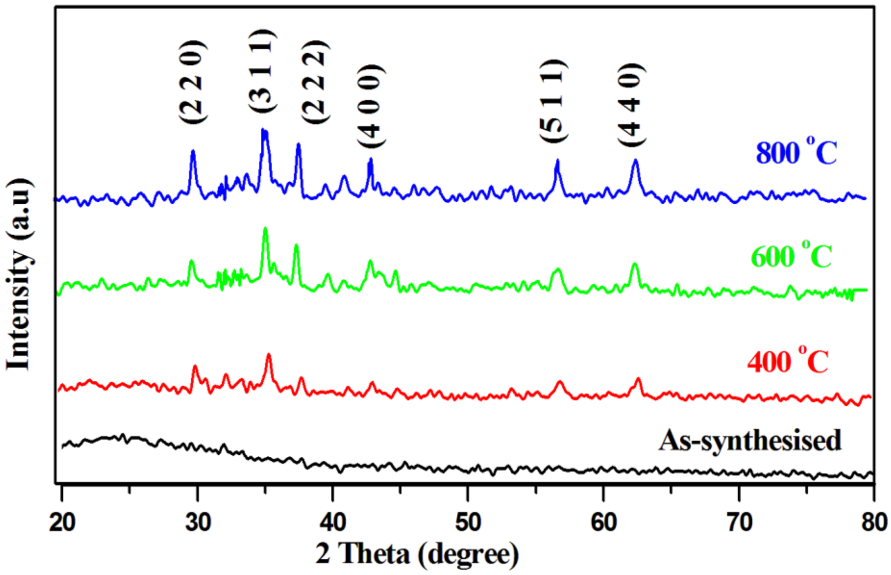

Fig. 5.3. XRD Spectra of $CoFe_2O_4$ nano particles as-synthesized and calcinated at different temperatures

In which the as-synthesized sample doesn't show any peaks it specifies that calcination is necessary to stabilizing the particle size and formation of nanoparticles. X-ray Diffraction pattern of all the calcinated samples exhibited the reflection planes of (220), (311), (222), (400), (511) and (440) for their equivalent 2θ. The obtained XRD peaks are indexed well with the standard pattern for $CoFe_2O_4$ reported in JCPDS card no # 22-1086 [Yang *et al.,* (2005)]. The obtained peaks in the present study confirm the formation of cobalt ferrite nanoparticles without any impurities and it has a cubic, spinel type lattice of space group Fd3m [Surendra *et al.,* (2011)]. By using the relation $a= d_{hkl}\ (h^2+k^2+ l^2)^{1/2}$ the lattice parameter "a" has been found and it is shown if table 7. The obtained XRD pattern in the present study suggest that 600 °C is suitable for further analysis.

TABLE 7: PARTICLE SIZE AND LATTICE PARAMETER of $CoFe_2O_4$ NANO PARTICLES

Temperature (°C)	Particle Size (nm)	Lattice Parameter(a)Å
400	14	8.389
600	29	8.390
800	42	8.397

The lattice parameter has been found increase with the increase of calcination temperature which may be attributed to the fact that on increasing the calcination temperature, a certain number of Co^{2+} ions migrate from octahedral to the tetrahedral sites, accompanied by opposite transfer of equivalent number of Fe^{3+} ions from tetrahedral to octahedral sites in order to relax the compressive strain. The result observed in the present study is close agreement with Rao *et al.,* (2015) for the preparation of ultra-fine cobalt ferrite nanoparticles. As the calcination temperature increases with increase in intensity of peaks and peak width has been detected in the present study representing the enhancement of crystallite size. By using Debye Scherer's formula the average particle size has been calculated [Houshiar *et al.,* (2014)]. The increase in trend for the particle size from 400 °C to 800 °C (table 7), has been obtained in the present study discloses the linear relation between particle growth and calcination. Huixian *et al.,* (2014) have reported to increase the particle size with the calcination temperatures are observed in the order of 19.7, 26.6, 29.3 nm at 600 °C, 800 °C and 1000 °C respectively. In addition the present work reveals that the synthesized product yield good particle growth than the earlier reported one.

5.2.4. FIELD EMISSION SCANNING ELECTRON MICROSCOPE (FESEM) WITH EDAX

Field emission scanning electron microscopy (FESEM) provides topographical and elemental information at higher magnification, with virtually unlimited depth of field. The FESEM images of cobalt ferrite are shown in Fig.5.4 (a), (b) and (c).

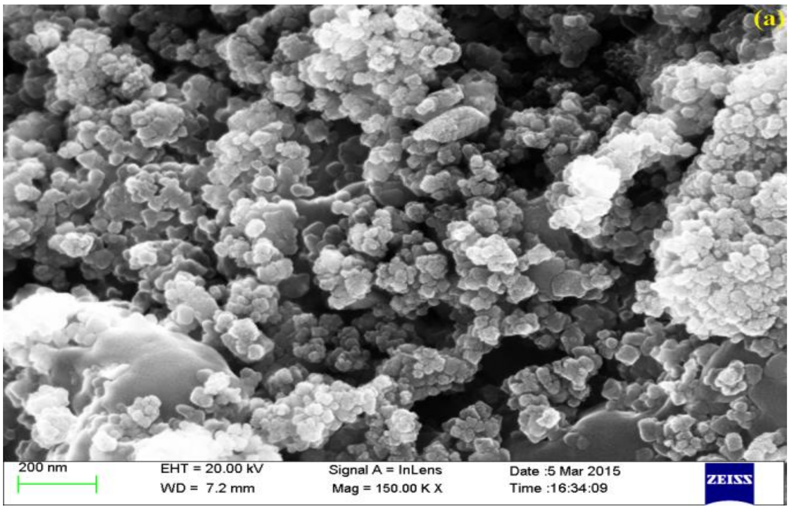
(a)
200 nm
EHT = 20.00 kV
WD = 7.2 mm
Signal A = InLens
Mag = 150.00 K X
Date :5 Mar 2015
Time :16:34:09
ZEISS

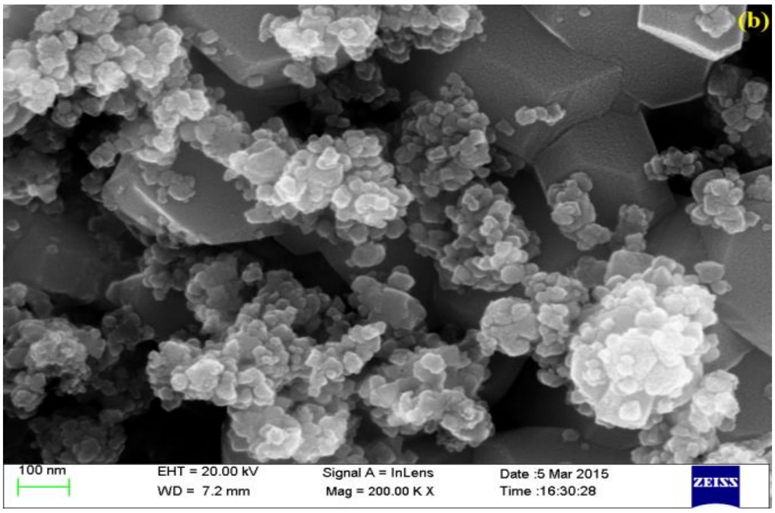
(b)
100 nm
EHT = 20.00 kV
WD = 7.2 mm
Signal A = InLens
Mag = 200.00 K X
Date :5 Mar 2015
Time :16:30:28
ZEISS

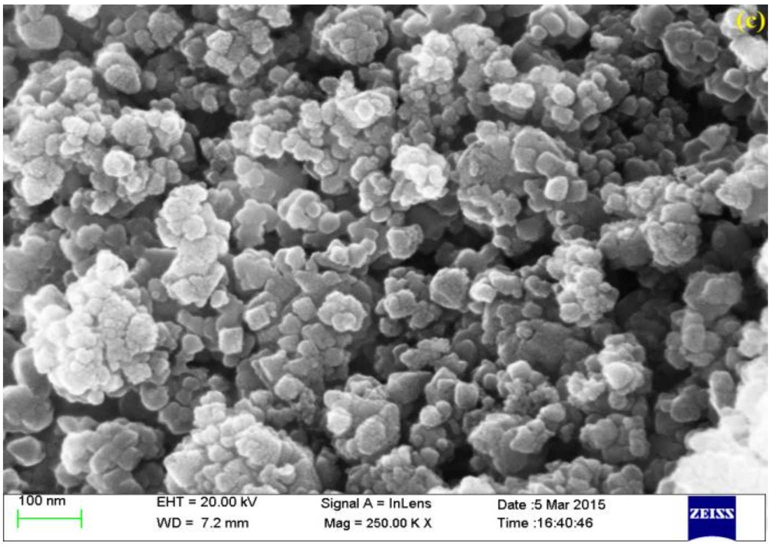
(c)
100 nm
EHT = 20.00 kV
WD = 7.2 mm
Signal A = InLens
Mag = 250.00 K X
Date :5 Mar 2015
Time :16:40:46
ZEISS

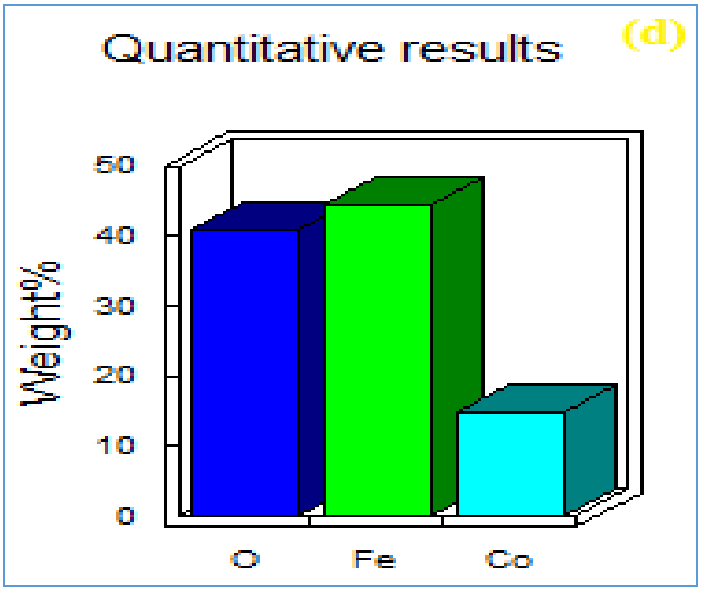

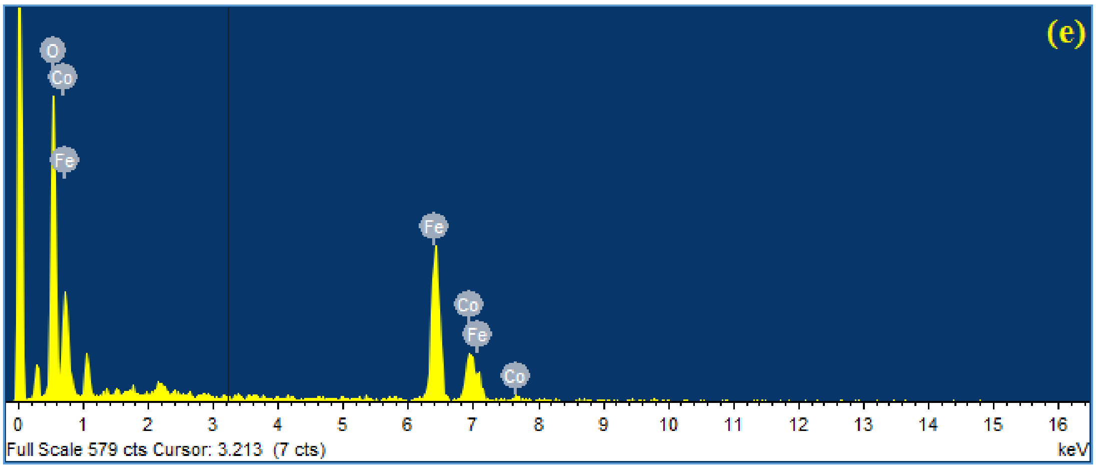

Fig. 5.4. (a), (b) and (c) FESEM image of $CoFe_2O_4$ nano particles calcinated at 600 °C with different magnifications Quantitative result (d) and (e) Corresponding EDAX

Uniform distribution of nearly cubical particles is identified through field emission scanning electron microscope (FESEM) images with particle size range from 29 to 31 nm. Cojocariu *et al.*, (2012) have reported the cubic SEM morphology for cobalt ferrite nanoparticles. The chemical composition of the sample is shown in Fig.5.4 (d) and its corresponding EDAX is shown in Fig.5.4 (e). EDAX spectrum of cobalt ferrite samples suggesting that the synthesized products are composed of Co, O and Fe elements. Moreover, EDAX results confirmed the ratio of the transition metal atoms in each material according to the nominal stoichiometry. The atomic ratio of Fe:Co for the entire calcinated sample (Fig.5.4 (e)) is maintained at ~ 2:1. These results revealed the sustained spinel structure of the $CoFe_2O_4$ crystal at calcination temperature. Similar result was reported by Pauline and Amdiya. (2011).The extra gold peak obtained in EDAX is due to the thin coating done on the sample to make the sample conducting, which is required to record the FESEM.

5.2.5. Field Emission Transmission Electron Microscope (FETEM) with SAED

The FETEM micrograph of cobalt ferrite nanoparticles calcinated at 600 °C for different magnification is shown in Fig.5.5 (a), (b), (c) and (d).

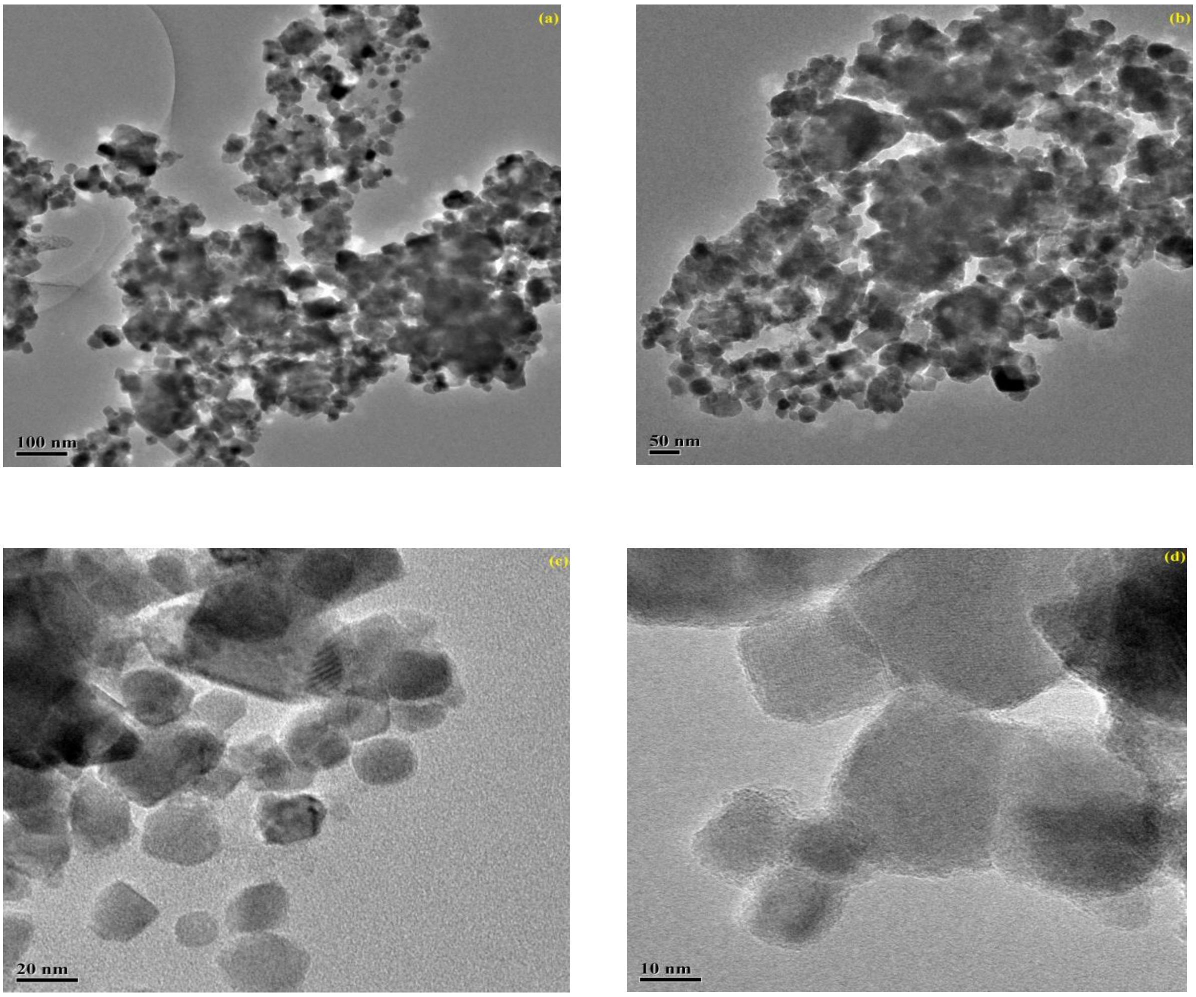

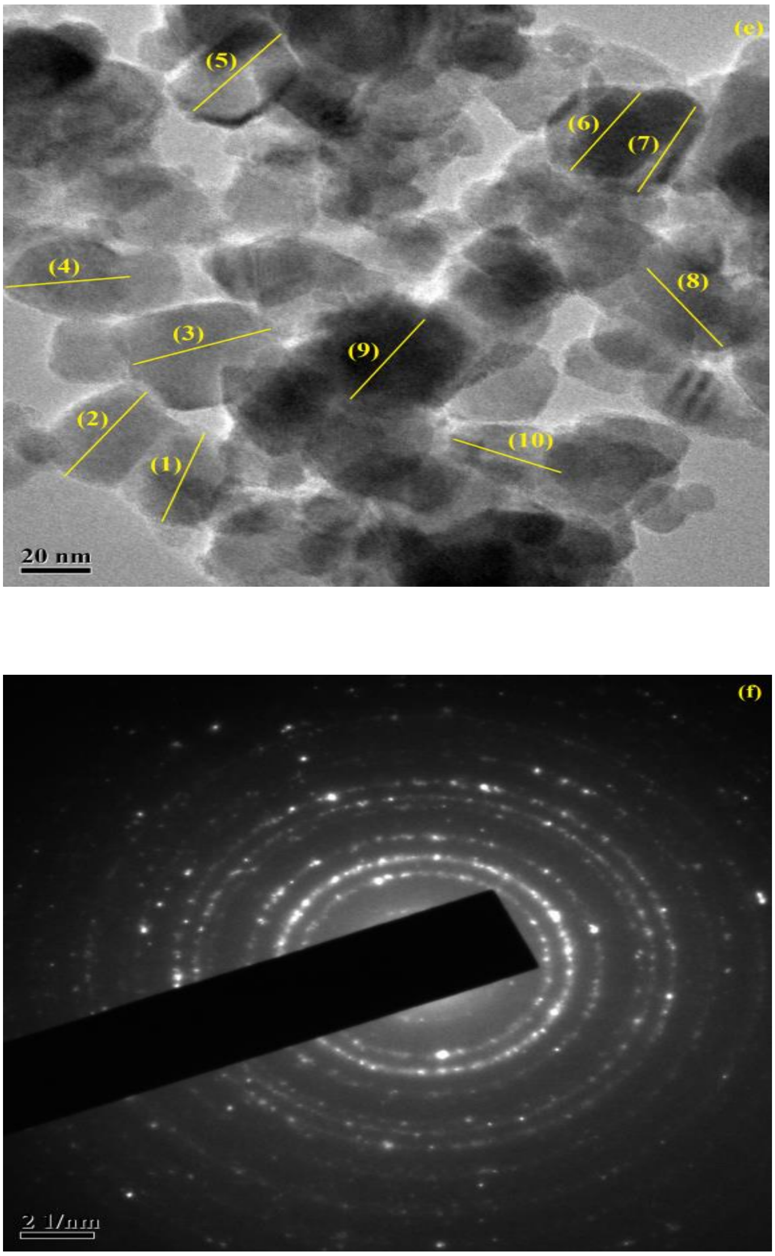

Fig. 5.5. (a), (b) (c) and (d) FETEM OF $CoFe_2O_4$ NANO PARTICLES CALCINATED AT 600 °C WITH DIFFERENT MAGNIFICATION. (e)PARTICLE SIZE MEASURED USING IMAGE J VIEWER SOFTWARE (f) CORRESPONDING SAED.

From the FETEM micrograph, it can be seen the particles are nano sized and revealed it is in cubic shape. Daliya *et al*., 2007 have reported the cubic morphology TEM image for cobalt ferrite nanoparticles. Well crystalline nature of $CoFe_2O_4$ nanostructure was confirmed by SAED pattern and it is shown in Fig.5.5 (f). By using the "Image J viewer software" [Loganathan *et al.,* (2015)] the length of the individual selected particles is found and it is shown in Fig.5.5 (e) and graph 2. From the software it is obtained the average particle size of 29 nm which is closely agree well with the XRD result.

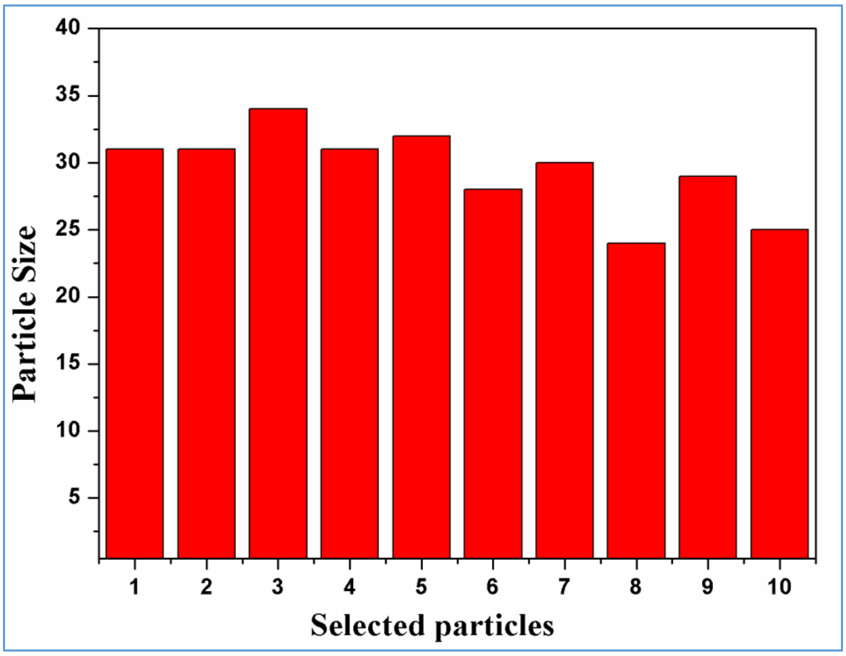

GRAPH.2 AVERAGE PARTICLE SIZE $CoFe_2O_4$ NANOPARTICLES USING IMAGE J VIEWER SOFTWARE FROM FETEM

5.2.6. CYCLIC VOLTAMMETRY (CV)

Cyclic voltammetry is the most widely used technique for acquiring quantitative information about electrochemical reactions. The power of cyclic voltammetry results from its ability to rapidly provide considerable information on the thermodynamics of redox processes and the kinetics of heterogeneous electron-transfer reactions, and on coupled chemical reactions or adsorption processes. In particular, it offers a rapid location of redox potentials of the electro-active species, and convenient evaluation of the effect of media upon the redox process [Warsi *et al.*, (2014)] The CV curve recorded at scan rate of 2, 3, 5, 10, 20, 30, 50 and 100 mVs^{-1} for $CoFe_2O_4$ calcinated at 600°C electrode is shown in Fig.5.6 (a).

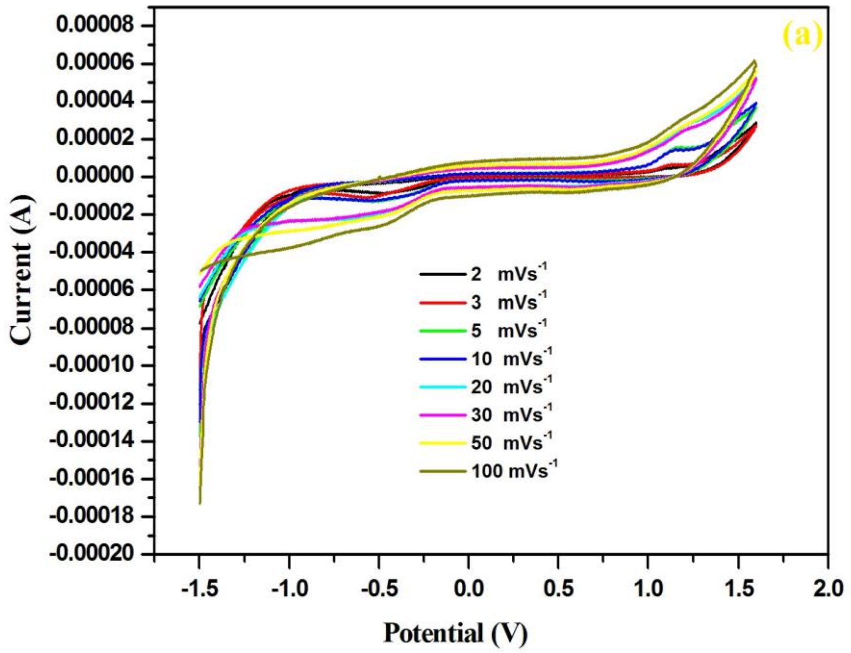

Fig. 5.6. (a) CV patterns of $CoFe_2O_4$ nano particles calcinated at 600 °C for different scan rates

The shape of the CV curves is an ideal rectangular shape observed at 2mVs^{-1}. The change in CV pattern with increasing scan rate, observed in the present study confirms the pseudo-capacitive nature of the material. The specific capacitances (SC) values of $CoFe_2O_4$ electrode can be calculated using the formula [Sathishkumar *et al.,* (2015)].

$$Cs = \frac{Q}{\Delta v . m}$$

Where, Cs indicates the specific capacitance, Q is the anodic and cathodic charges on each scanning, m points the mass of the electrode material (mg) and Δv represents the scan rate (mVs^{-1}). Normally three standard electrode configuration consisting of a sample (working electrode) an Ag/AgCl (reference electrode) and a high platinum wire which act as counter electrode was taken in 0.2 M tetra butyl ammonium perchlorate [Sathishkumar *et al.,* (2015)]. As the scan rate increases in the range from 2 mVs^{-1} to 100 mVs^{-1} their corresponding specific capacitance value decreases with the increase of scan rates which are illustrated in Fig.5.6 (b) and table 8.

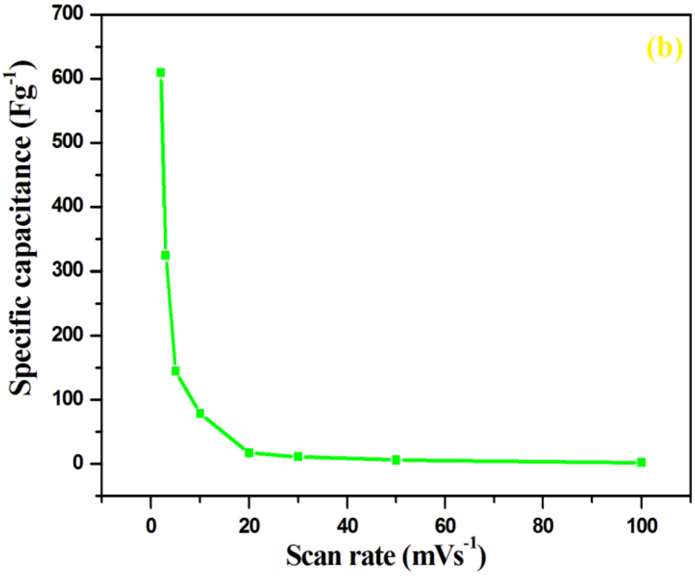

Fig. 5.6. (b) DIFFERENT SCAN RATE AND THEIR SPECIFIC CAPACITANCE VALUES

TABLE 8. THE SPECIFIC CAPACITANCE OF THE $CoFe_2O_4$ NANO PARTICLES CALCINATED AT 400 °C, 600 °C and 800 °C FOR DIFFERENT SCAN RATES

Scan Rates (mVs^{-1})	$CoFe_2O_4$ (600°C) Fg^{-1}
2	609
3	324
5	145
10	78
20	17
30	11
50	6
100	2

A higher capacitance value of 609 Fg^{-1} for $CoFe_2O_4$ nano particles calcinated at 600 °C is noted in the present study. Kumbhar *et al.*, 2012 have reported a maximum specific capacitance value of 366 Fg^{-1} for cobalt ferrite nanoparticles with particle size of 34 nm sample annealed at 450 °C which is much lesser than the present study. Higher specific capacitance at low scan rate is observed in the present study, suggest that the ionic diffusion takes place in, both inner and outer surfaces, whereas lower specific capacitance values observed for higher scan rates indicate that the ionic diffusion takes place only for outer surfaces [Pang *et al.,* (2011)]. The higher specific capacitance value observed in the present study confirms the good crystallinity of the $CoFe_2O_4$ nano particles [Hao *et al.*, (2015)].

5.2.7: DYNAMIC LIGHT SCATTERING (DLS) AND ZETA POTENTIAL

Dynamic Light Scattering is one of the most popular light scattering techniques which allows particle sizing down to 1 nm diameter. Typical applications are emulsions, micelles, polymers, proteins, nanoparticles or colloids. The sample is illuminated by a laser beam and the fluctuations of the scattered light are detected at a known scattering angle θ by a fast photon detector. Simple DLS instruments that measure at a fixed angle can determine the mean particle size in a limited size range. More elaborated multi-angle instruments can determine the full particle size distribution. [Backes, *et al.,* (2015)]. Size distribution of the $CoFe_2O_4$ nanoparticles calcinated at 600 °C of pH8 is shown in Fig.5.7 (a). The
Z-average is found by using DLS zeta analyser as 296.6 nm. The greater size is due to insolubility and aggregation of the sample in water while analysing. Fig.5.7 (b) depicts the zeta potential of $CoFe_2O_4$ nanoparticles calcinated at 600 °C.

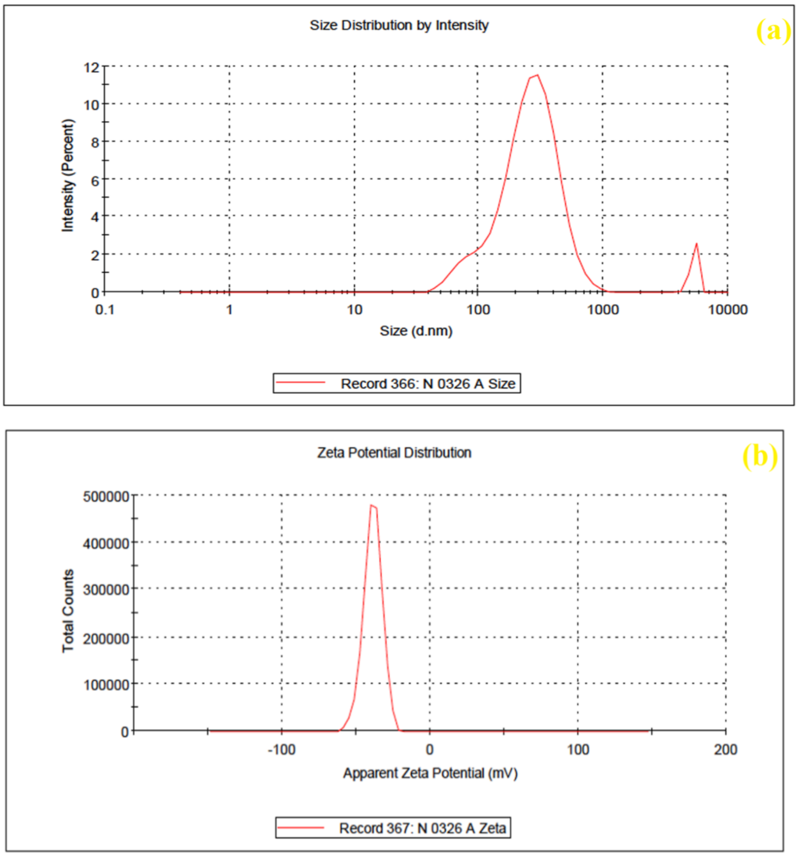

Fig.5.7 (a) Zeta sizer and Fig. 5.7 (b) Zeta potntial of $NiFe_2O_4$ nano particles calcinated at 600 °C

The stability of the $CoFe_2O_4$ nanoparticles is determined using a zeta potentiometer. The zeta potential is a key indicator of the stability of colloidal dispersions which gives the magnitude of potential stability and surface charge of the synthesized $CoFe_2O_4$ nanoparticles. The results of the zeta potential and zeta deviation are -38.4 mV and 5.96 mV respectively and they reveal the good stability of synthesized $CoFe_2O_4$ nanoparticles. Sasmita Mohapatra *et al.,* (2011) have reported a stability range of -17 mV is very much lower value than the present work and confirmed that the prepared sample is more stable.

5.2.8: X-ray photoelectron spectroscopy (XPS)

The element composition can be quantified by use of X-ray photoelectron spectroscopy [Gaikwad *et al.,* (2011)]. Fig.5.8 (a) depicts the Fe2p peak fixed around 708.2 eV belongs to Fe^{2+}.

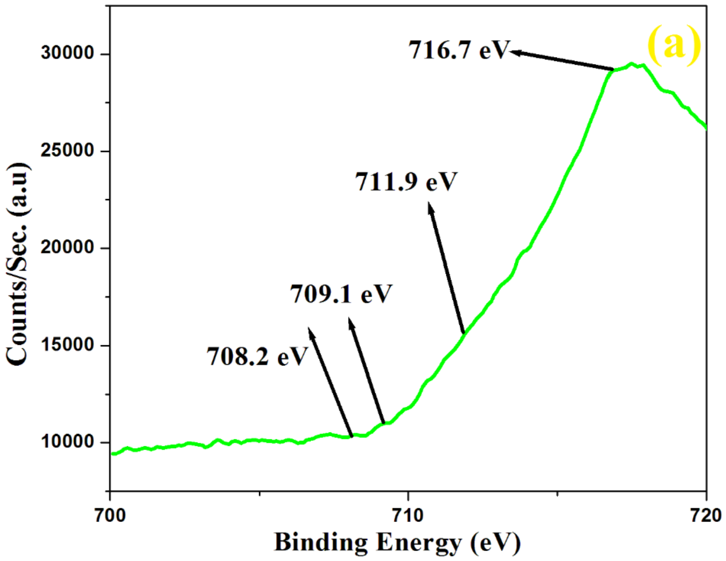

Fig.5.8.(a) XPS spectra of Fe for $CoFe_2O_4$ nano particles calcinated at 600 °C

The peak around 709.1 and 711.9 eV are assigned to Fe^{3+} at octahedral and tetrahedral sites respectively.In addition to this a satellite line observable at a binding energy of around 716.7 eV [Nakagomi *et al.,* (2007)]. Fig. 5.8 (b) illustrates the XPS spectra of the sample enclose peaks around 778.7 eV and 779.6 eV corresponding to Co^{2+} at octahedral and tetrahedral sites.

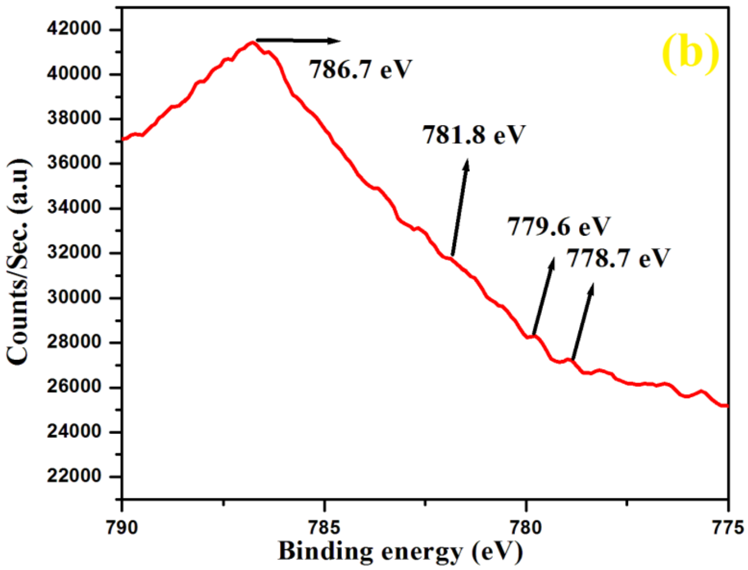

Fig. 5.8. (b) XPS SPECTRA OF CO FOR $CoFe_2O_4$ NANO PARTICLES CALCINATED AT 600 °C

A shoulder around 781.8 eV which is assigned to Co^3+ and a satellite peak has been detected around 786.7 eV. Fig.5.8 (c) shows the O1s photo electron spectra of the present sample, the prominent photoelectron peak around at 529.3 eV is the influence from the crystal lattice Oxide ion (O^{2-}), while the shoulder signifies non-stoichiometry which results due to photoelectron emitted from oxide ion in the vicinity of such defects and suffers from excess loss in kinetic energy resulting in higher binding energy [Nowak and Laajalehto kari (2007)].

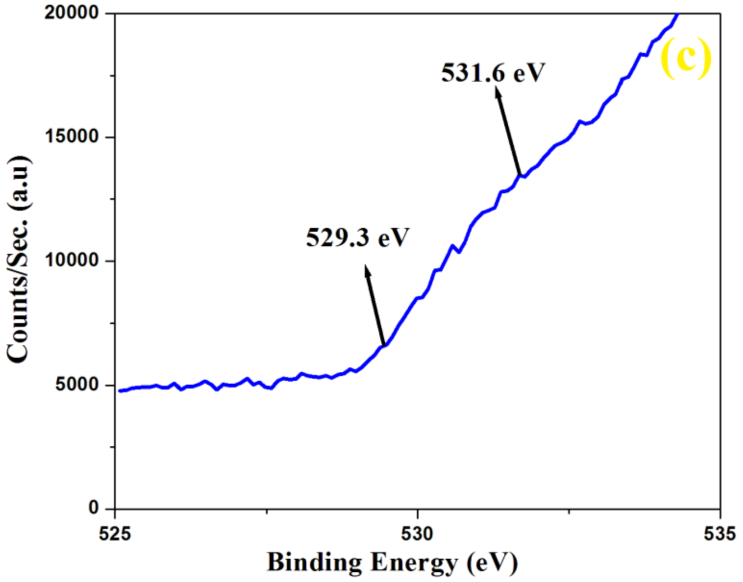

Fig. 5.8.(c) XPS spectra of O for $CoFe_2O_4$ nano particles calcinated at 600 °C

In addition, the higher binding energy peak at 531.6 eV may be attributed to surface defects or chemisorbed oxygen species (–OH) [Zhang*et al.,* (2011)]. From the XPS analysis it may conclude that the $CoFe_2O_4$ nanoparticles have existed in multiple oxidation states.

5.3. Conclusion

Cobalt ferrite nanoparticles were synthesized by co-precipitation method with citrate as chelating agent and it is further calcinated at various temperatures such as 400, 600 and 800 °C. XRD pattern confirmed that the prepared sample was nanosized cobalt ferrite nanoparticles. TG/DTA study exposed the mechanism of formation of $CoFe_2O_4$ nano particles. Functional groups have been identified with the FTIR analysis. FESEM and FETEM with SAED pattern confirm that the prepared sample was cubic in shape. EDAX showed that the sample contains only Co, Fe and O. Particle size was calculated from XRD by using Debye Scherer formula matched well with the particle size calculated from FETEM using the software “image j viewer”. DLS zeta potential exposed the well stability of the prepared $CoFe_2O_4$ nanoparticles. Higher capacitance value 609 Fg^{-1} was observed for $CoFe_2O_4$ nano particles calcinated at 600 °C at the scanning rate of 2 mVs^{-1} from the CV study which is suitable for super capacitance application. The XPS analysis confirmed that the synthesized $CoFe_2O_4$ nanoparticles have exist in multiple oxidation states.

CHAPTER-VI

SYNTHESIS AND CHARACTERIZATION OF NICKEL COBALT FERRITE (Ni1-xCoxFe2O4) NANO PARTICLES BY CO-PRECIPITATION METHOD WITH CITRATE AS CHELATING AGENT

6.1. INTRODUCTION

The particles of size having in the range nano will exhibit unique chemical and physical properties [Wang *et al.,* (2006)]. Among which nanocomposite materials composed of nano-metric metal and metal oxide particles embedded in vitreous matrices reveal a variety of interesting magnetic, electric, catalytic properties etc. [Nejati *et al.,* (2012); Mishra *et al.,* (2006); Mandlimath and Gopal, (2011)]. In electric, supercapacitor plays a vital role because of the increase in demand for high power energy resources. Supercapacitors have attracted much attention owing to their fast charging, safety and long term cycle stability [Kotz and Carlen, (2000)]. Ferrite based nanoparticles continue to evoke interest owing to their extensive use in technological and industrial applications. Moreover, spinel ferrites are very much important group of materials due to their chemical, structural, mechanical and magnetic properties. Amongst all inverse spinel ferrites, the nickel substituted cobalt ferrite has been extensively studied in view of their better chemical and thermal stability, supercapacitor behavior, super-paramagnetism etc. There are several novel methods which are used to prepare ferrite nanoparticles, such as co-precipitation method [Derakhshi *et al.,* (2012)], microwave-assisted flash combustion technique [Krieble *et al.,* (2005)], solid state method [Zhao *et al.,* (2006); Thakur *et al.,* (2007)], sol-gel method [Kumar *et al.,* (2009)], ball milling process [Pradhan *et al.,* (2005)] and spray pyrolysis [Jung *et al.,* (2009)]. Among which co-precipitation method has been chosen because it has advantage of producing ultra-fine, high purity and crystalline nano particles in minimum duration than other methods. Nickel substituted cobalt ferrite based supercapacitor is a new idea to overcome the energy deficiency.In addition the supercapacitor nature $Ni_{1-x}Co_xFe_2O_4$ nanoparticles also have abundant applications such as gas sensors [Chen; *et al.,* (2010)], recording media [Jung *et al.,* (2009)], energystorage [Koseoglu *et al.,* (2009)], ferro-fluids [Sousa *et al.,* (2002)] and catalysts [Ramankutty and Sugunan, (2001)]. In the present work, nickel cobalt ferrite nano particles have been attained through simple co-precipitation method along using citric acid as a chelating agent.

6.2. RESULTS AND DISCUSSION

6.2.1. THERMO GRAVIMETRIC AND DIFFERENTIAL THERMAL ANALYSIS

In thermal analysis changes the physical and chemical properties of materials are measured as a function of increasing temperature (with constant heating rate), or as a function of time (with constant temperature and/or constant mass loss).To study the thermal behaviour of as-prepared $Ni_{1-x}Co_xFe_2O_4$ nanoparticles, thermo gravimetric (TG) and differential thermal (DT) analysis were performed simultaneously in the temperature range of 35 °C to 850 °C. Fig.6.1 depicts the TGA and DTA curves of as-synthesized $Ni_{1-x}Co_xFe_2O_4$ nanoparticles (x=0.5).

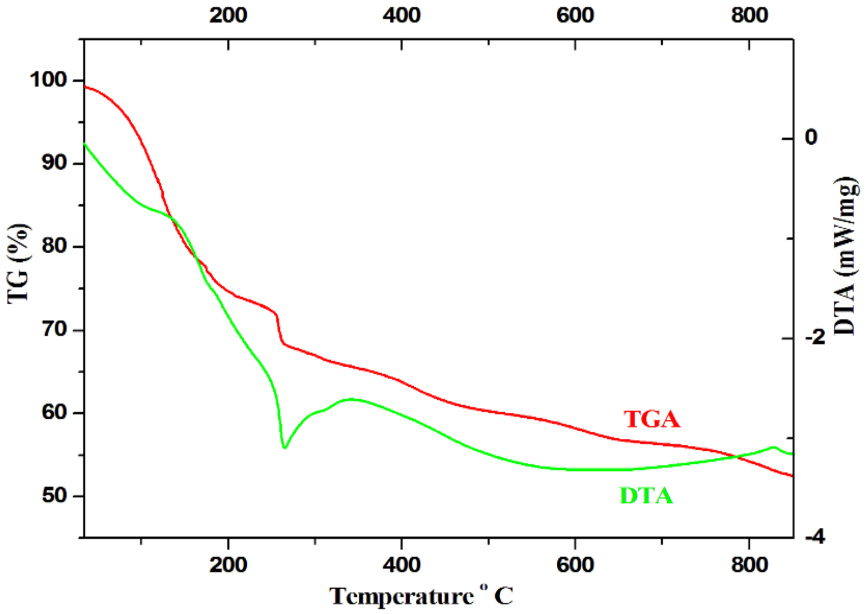

Fig. 6.1. TGA/DTA ANALYSIS OF $Ni_{1-x}Co_xFe_2O_4$ (x=0.5) NANO PARTICLES

Three major weight losses have been observed from the TG analysis in the range from 35 °C to 850 °C. The first stage of moderate weight loss 11% is detected at a temperature below 120 °C due to desorption of water. The second stage of major weight loss 20% is observed in the range from 120 °C to 265 °C as a result of decomposition of organic templates. The final stage of minimum weight loss 3% is found between 265 °C and 455 °C due to crystallization of the final product. Above 455 °C, there is no weight loss, representing that precursor generates a stable phase indicating the formation of $Ni_{1-x}Co_xFe_2O_4$ nano particles. Hankare *et al.*,

(2013) have reported no significant weight loss observed above 370 °C, indicating that precursor generates a stable phase. A peak at119 °C in DTA curve shows an endothermic peak due to dehydration. The endothermic peak at 280 °C is recognized due to the decomposition of nitrates. The exothermic peak at 345 °C relates to the complete decomposition of citrate precursor to nickel cobalt ferrite with the simultaneous evolution of CO, CO gas and acetone molecules formed Ati *et al.,* (2014) have reported that the exothermic and endothermic regions in the DTA pattern are consistent with the change regions in the TG pattern which confirms the formation of stable cobalt nickel ferrite after no weight loss in TGA.

6.2.2. FUNCTIONAL GROUP ANALYSIS

In order to know the presence of functional groups in the prepared samples, FTIR spectra of $Ni_{1-x}Co_xFe_2O_4$ (x = 0.3, 0.5, 0.7) nanoparticles calcinated at 400 °C, 600 °C and 800 °C were recorded in the range of 4000-400 cm^{-1} is shown in Fig.6.2 (a),(b) and (c).

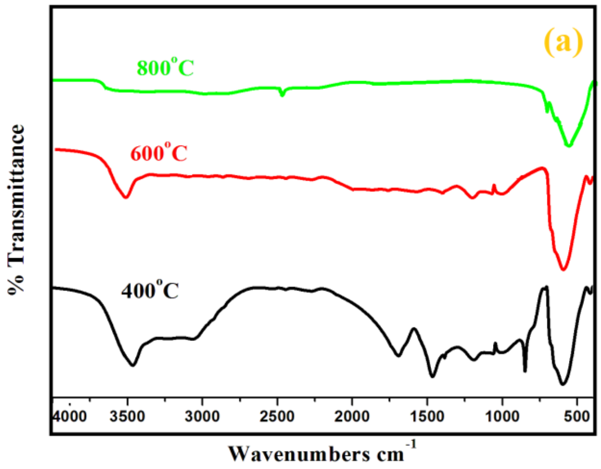

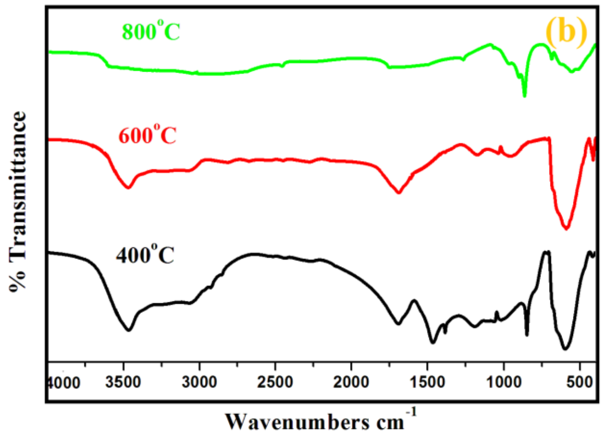

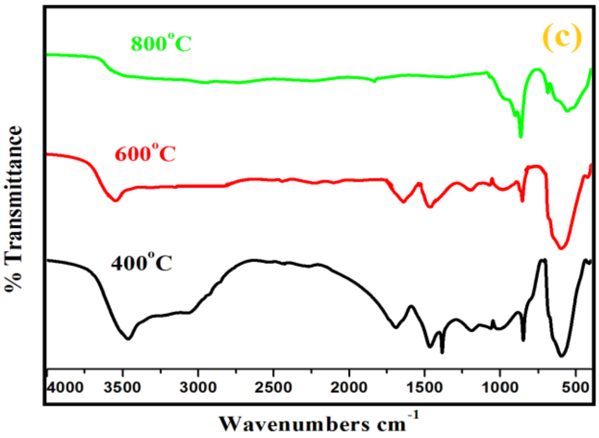

Fig. 6.2. FTIR SPECTRA OF $Ni_{1-x}Co_xFe_2O_4$ (x = 0.3, 0.5, 0.7) NANO PARTICLES CALCINATED AT DIFFERENT TEMPERATURES 400 °C, 600 °C AND 800 °C

The FTIR spectrum has two main absorption bands around 410 cm^{-1}and 590 cm^{-1}, which corresponds to the octahedral and tetrahedral sites of $Ni_{1-x}Co_xFe_2O_4$ (x = 0.3, 0.5, 0.7) respectively. In which the higher absorption band around 590cm^{-1} resembles to the intrinsic vibrations Fe-O of tetrahedral complexes and the lower absorption band around 410 cm^{-1} is recognised to the vibrations (Ni-O and Co-O) of octahedral complexes [Singh *et al.*, (2014); Deraz and Omar, (2014)]. The absorption bands presented around 3400 cm^{-1} in all the samples could be due to the hydrogen bonded hydroxyl group. The other two bands occurring around 2970–2446 cm^{-1} are assigned to the anti-symmetric and symmetric CH_2-vibrations respectively, and the absorption band around 1450 cm^{-1} corresponds to the CH_2-bending vibration [Gonsalves *et al.*, (2012)].

6.2.3. STRUCTURAL ANALYSIS

By using the XRD patterns the phase identification of as-prepared and calcinated $Ni_{1-x}Co_xFe_2O_4$ powder was carried out. Fig.6.3 (a), (b) and (c) depicts the X-ray diffractograms of $Ni_{1-x}Co_xFe_2O_4$ where x = 0.3, 0.5 and 0.7 samples at various temperatures 400 °C, 600 °C and 800 °C. Among them the as-synthesized sample does not show any peaks and it clearly stipulates that, calcinations is essential for the formation of $Ni_{1-x}Co_xFe_2O_4$ nanoparticles.

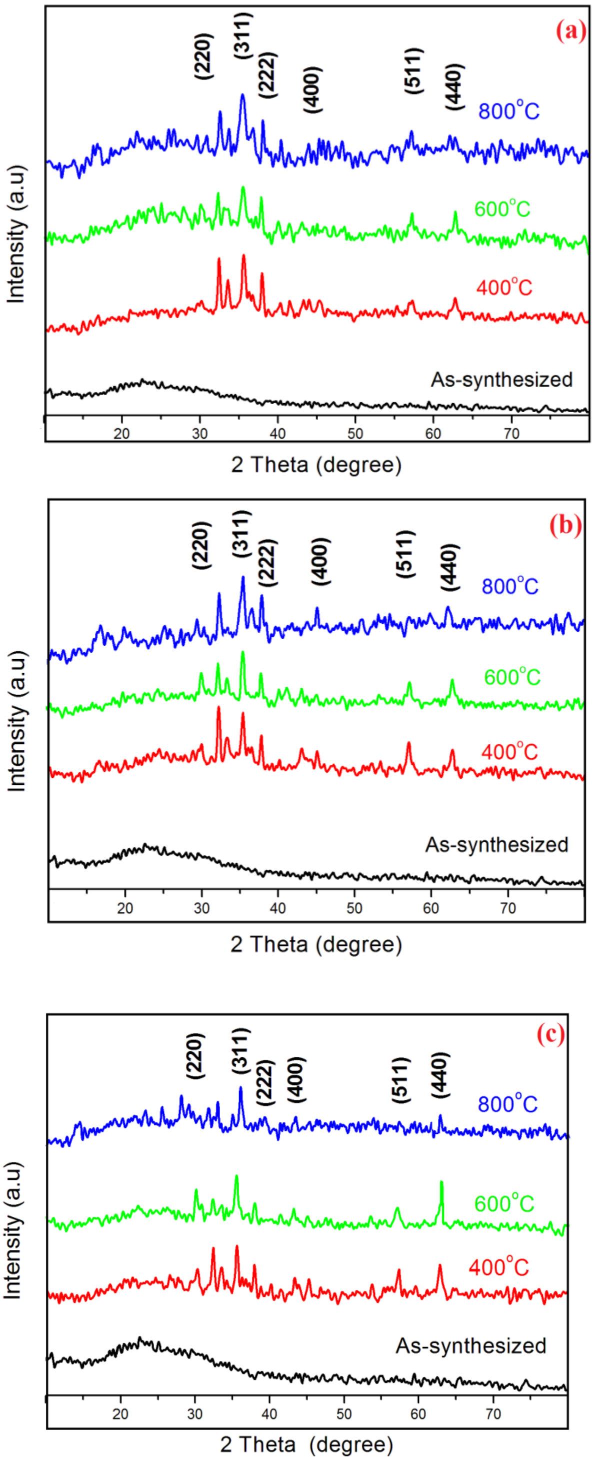

Fig. 6.3. XRD SPECTRA OF $Ni_{1-x}Co_xFe_2O_4$ (a),(b) and (c) (x = 0.3, 0.5 AND 0.7 RESPECTIVELY) NANO PARTICLES AS-SYNTHESIZED AND CALCINATED AT DIFFERENT TEMPERATURES

XRD pattern of the calcinated samples at various temperatures show the main diffraction planes of (220), (311), (222), (400), (511) and (440) with maximum intensity at (311) plane. The attained XRD peaks are matched well with the standard pattern reported in JCPDS card no. 742081 for Nickel ferrites ($NiFe_2O_4$) and JCPDS card no. 791744 for the Cobalt ferrites ($CoFe_2O_4$) [Abdul Gaffoor *et al.*, (2014)]. The detected peaks in the present study confirm the formation of nickel cobalt ferrite nanoparticles without any impurities agrees to the well-known structure of $Ni_{1-x}Co_xFe_2O_4$ which has a cubic, spinel type lattice of space group Fd3m [Velhal *et al.*, (2015)]. The average crystallite size has been found from the full-width at half-maximum (FWHM) for the prominent reflection peak (311) by applying the Scherrer equation [Cullity *et al.*, (1978)].

$$D = \frac{K\lambda}{\beta \cos\theta}$$

Whereas, D represents the crystallite size, K (=0.9) is a constant related to the shape of the crystal, λ is the incident wavelength of Cu-Kα radiation of the XRD, β specifies the peak width at mid-height and h is the considered angle in radians, and θ is the Bragg diffraction angle. The average lattice parameter “a” has been calculated by using the formula $a=d_{hkl}(h^2+k^2+l^2)^{1/2}$ [Salem *et al.*, (2011)].The table 9 depicts that the particle size not only increases with the increase of calcination temperature from 400 °C to 600 °C and 600 °C to 800 °C but also increases with the increase of cobalt content which is due to the ionic radii of cobalt is higher than that of nickel. Moreover a similar trend is found that lattice parameter not only increases with the increase of calcination temperature but also increases with the increase of cobalt content which is also shown in table 9. From the obtained XRD pattern in the present study suggest that the further analysis were carried out for nickel cobalt ferrite nanoparticles calcinated at 600 °C.

TABLE 9: THE AVERAGE PARTICLE SIZE USING DEBYE SCHERER’S FORMULA FROM XRD SPECTRA OF $Ni_{1-x}Co_xFe_2O_4$ (x = 0.3, 0.5 and 0.7) NANO PARTICLES CALCINATED AT DIFFERENT TEMPERATURES

Calcinated Temperature (°C)	$Ni_{0.7}Co_{0.3}Fe_2O_4$		$Ni_{0.5}Co_{0.5}Fe_2O_4$		$Ni_{0.3}Co_{0.7}Fe_2O_4$	
	Particle size (nm)	**a Å**	**Particle size (nm)**	**a Å**	**Particle size (nm)**	**a Å**
400 °C	21	8.381	27	8.384	34	8.386
600 °C	26	8.387	31	8.390	41	8.393

800 °C	40	8.391	57	8.396	66	8.399

The intensity of peaks and peak width has been detected in the present study representing the enhancement of crystallite size for the increase in calcination temperature [Umare *et al.*, (2008)]. Using Debye Scherer's formula the particle size of ($Ni_{1-x}Co_xFe_2O_4$; x = 0.3, 0.5, 0.7) is exposed in table 9, which reveals the linear relation between particle growth and calcination. Also from the table it is able to note that the particle size gradually increases with the increase of cobalt concentration. This may due to the ionic radii of cobalt is higher than that of nickel ion, while replacing nickel ions and incorporating the cobalt ions in the nickel ferrite lattice will promote the increase of particle size. de Freitas *et al.*, (2016) have reported the increase of particle size with the increase of cobalt concentration for $Ni_xCo_{1-x}Fe_2O_4$ (x=1, 0.75, 0.5, 0.25 and 0) as 38.0 nm, 41.4 nm, 42.7 nm, 48.4 nm and 49.0 nm respectively.

6.2.4. **FIELD EMISSION SCANNING ELECTRON MICROSCOPE (FESEM) WITH EDAX**

FESEM visualize very small topographic details of the sample on the surface or entire or fractioned objects. It can able to provide topographical and elemental information at magnifications of 10x to 300,000x, with virtually unlimited depth of field.Fig.6.4 (a) to (o) depicts the FESEM images of 600 °C calcinated $Ni_{1-x}Co_xFe_2O_4$ (x = 0.3, 0.5, 0.7). Fig.6.4 (a), (b), (c) corresponds to the FESEM images with various magnification of $Ni_{0.7}Co_{0.3}Fe_2O_4$ also Fig.6.4 (f), (g), (h) belongs to the FESEM images with various magnification of $Ni_{0.5}Co_{0.5}Fe_2O_4$ and Fig.6.4(k), (l), (m) relates to the FESEM images with various magnification of $Ni_{0.3}Co_{0.7}Fe_2O_4$.

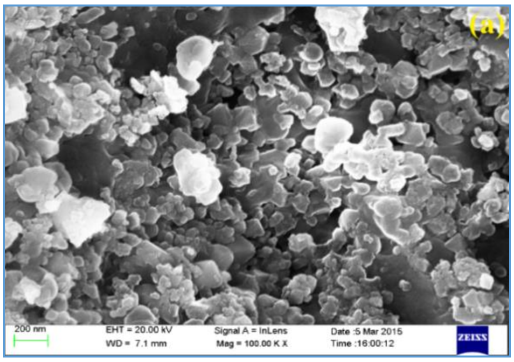

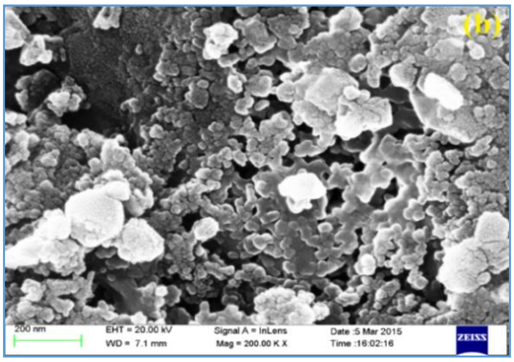

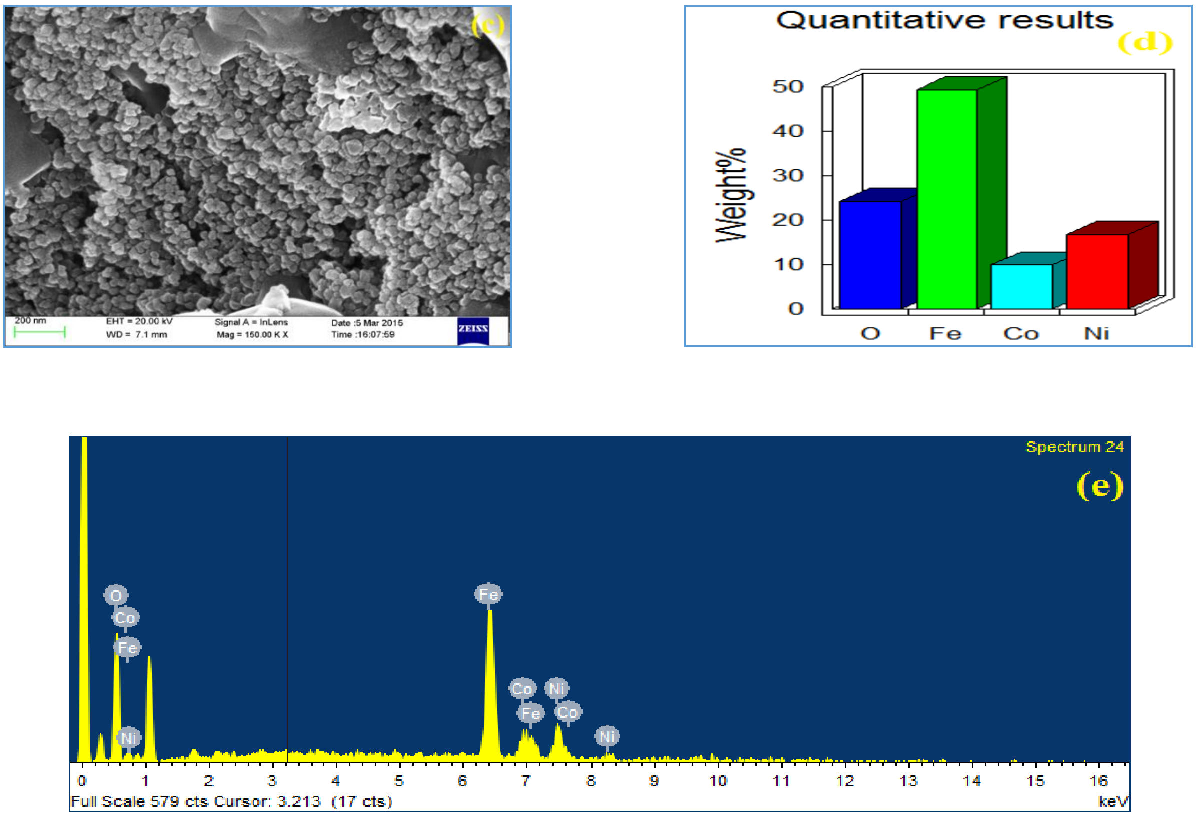

Fig. 6.4. (a), (b), (c) FESEM IMAGE OF $Ni_{1-x}Co_xFe_2O_4$ (x = 0.3) NANO PARTICLES CALCINATED AT 600 °C WITH DIFFERENT MAGNIFICATIONS ALSO (d) QUANTITATIVE RESULTS AND (e) CORRESPONDING EDAX

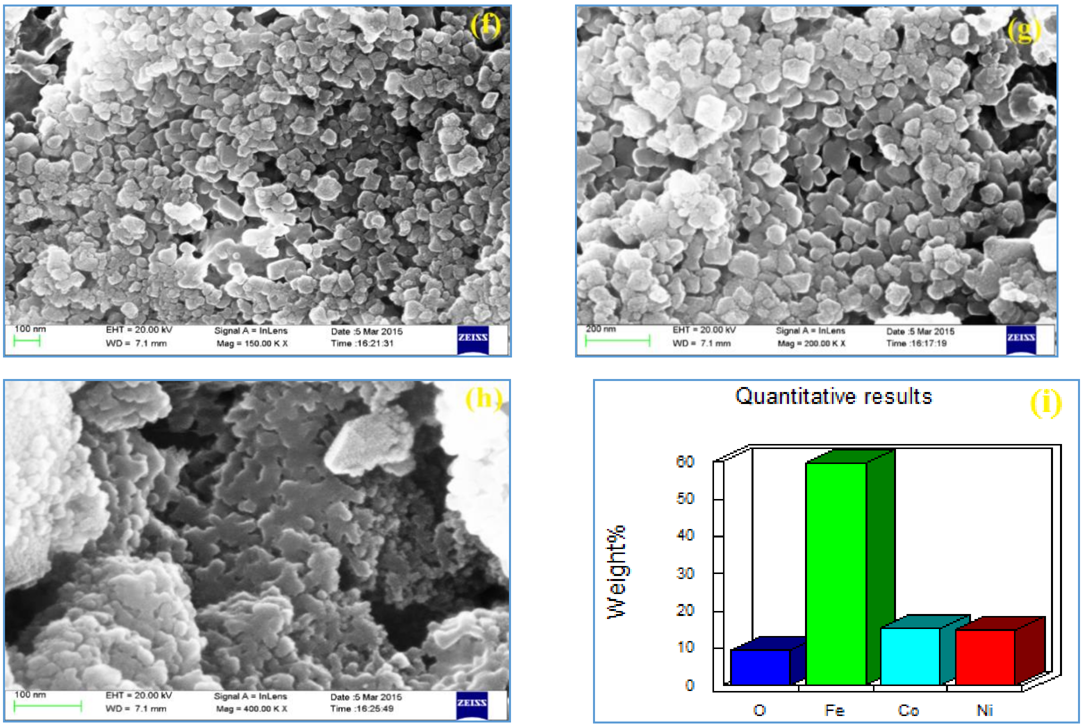

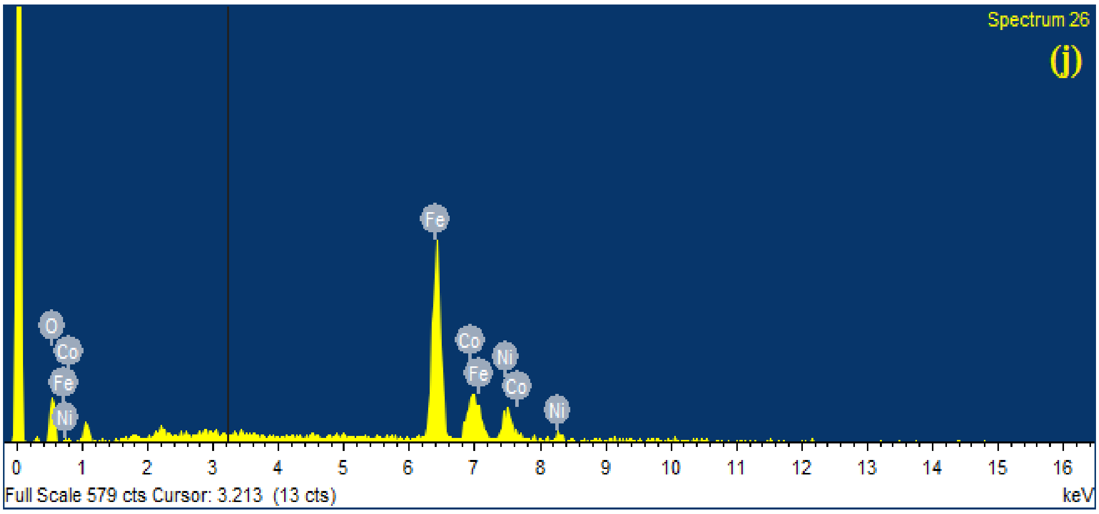

Fig. 6.4. (f), (g), (h) FESEM IMAGE OF $Ni_{1-x}Co_xFe_2O_4$ (x = 0.5) NANO PARTICLES CALCINATED AT 600 °C WITH DIFFERENT MAGNIFICATIONS ALSO (i) QUANTITATIVE RESULTS AND (j) CORRESPONDING EDAX

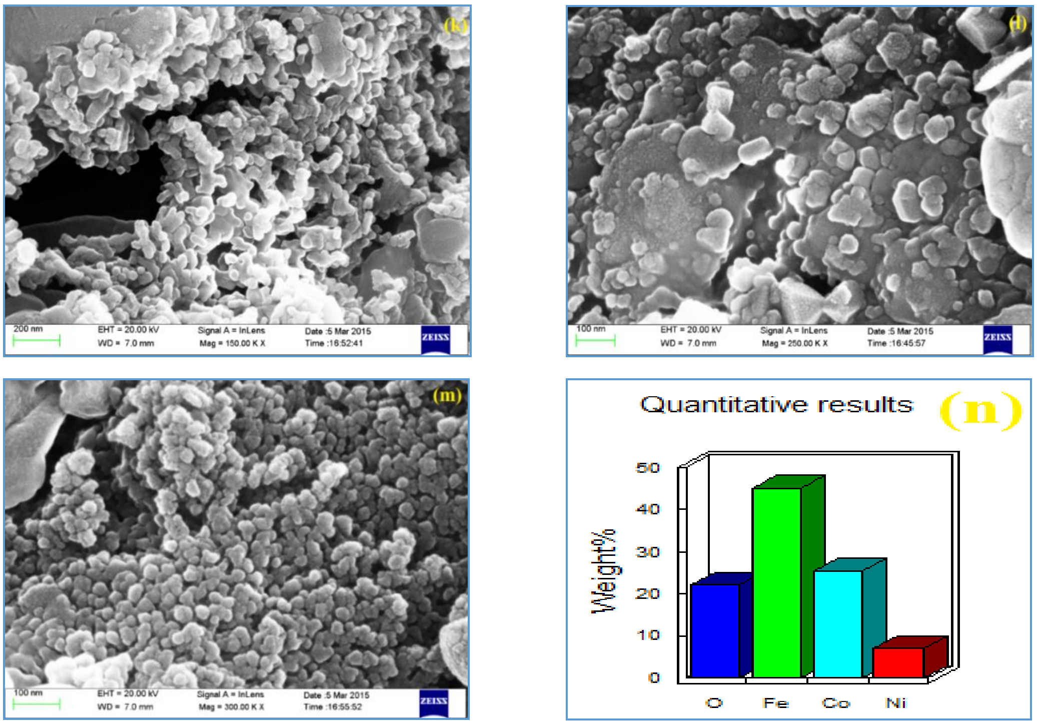

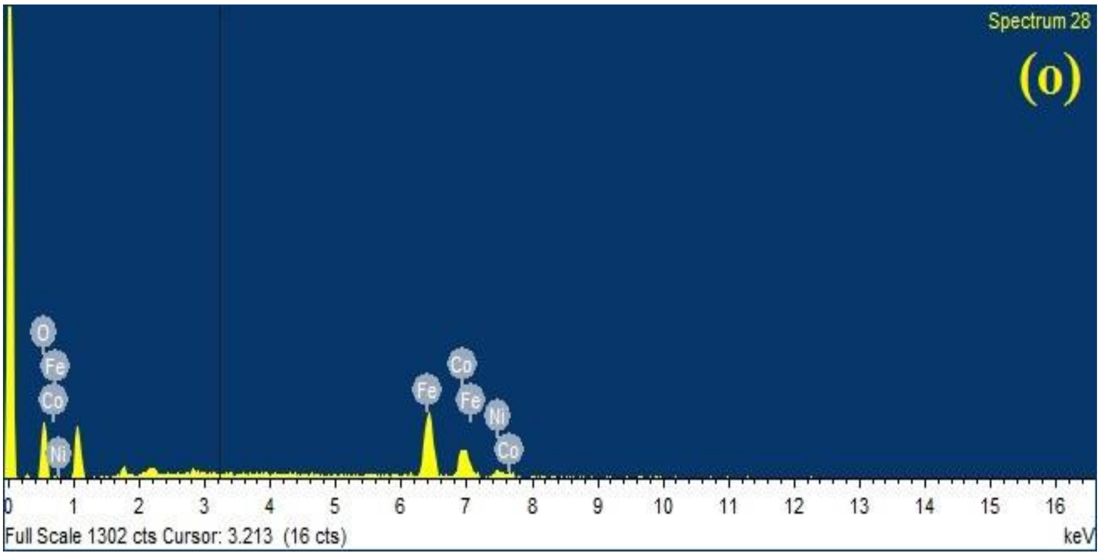

Fig. 6.4. (k), (l), (m) FESEM IMAGE OF **$Ni_{1-x}Co_xFe_2O_4$ (x = 0.7)** NANO PARTICLES CALCINATED AT 600 °C WITH DIFFERENT MAGNIFICATIONS ALSO (N) QUANTITATIVE RESULTS AND (O) CORRESPONDING **EDAX.**

From all different concentrations (x = 0.3, 0.5, 0.7) it is clearly detected that the particles are uniformly distributed of nearly cubical particles [Maaz *et al.*, (2009)]. Also the Fig.6.4 (d), (i), (n) represents the chemical composition of the sample it discloses the percentage of the elements present in the sample. It reveals the increase of cobalt concentration as the value “x” gets increases from 0.3, 0.5 and 0.7. Also it clearly depicts that when the value of “x” increases the cobalt concentration also get increased whereas nickel concentration got decreased later it was confirmed by EDAX spectrum. The corresponding EDAX of $Ni_{1-x}Co_xFe_2O_4$ (x = 0.3, 0.5, 0.7) is exposed in Fig.6.4 (e), (j) and (o) respectively. EDAX spectrum of $Ni_{1-x}Co_xFe_2O_4$(x = 0.3, 0.5, 0.7) samples suggesting that the synthesized products are composed of Co, Ni, O and Fe elements. Moreover, EDAX results confirmed the ratio of the transition metal atoms in each material according to the nominal stoichiometry. Singh *et al.*, (2014) have also reported that synthesized nickel cobalt ferrite nanoparticles contains only Co, Ni, Fe, O elements are in nominal stoichiometry. The extra gold peak achieved in EDAX is owing to the thin coating which is done on the sample before examining for making the sample into conducting one, which is essential to analysis the FESEM.

6.2.5. FIELD EMISSION TRANSMISSION ELECTRON MICROSCOPE (FETEM) WITH SAED

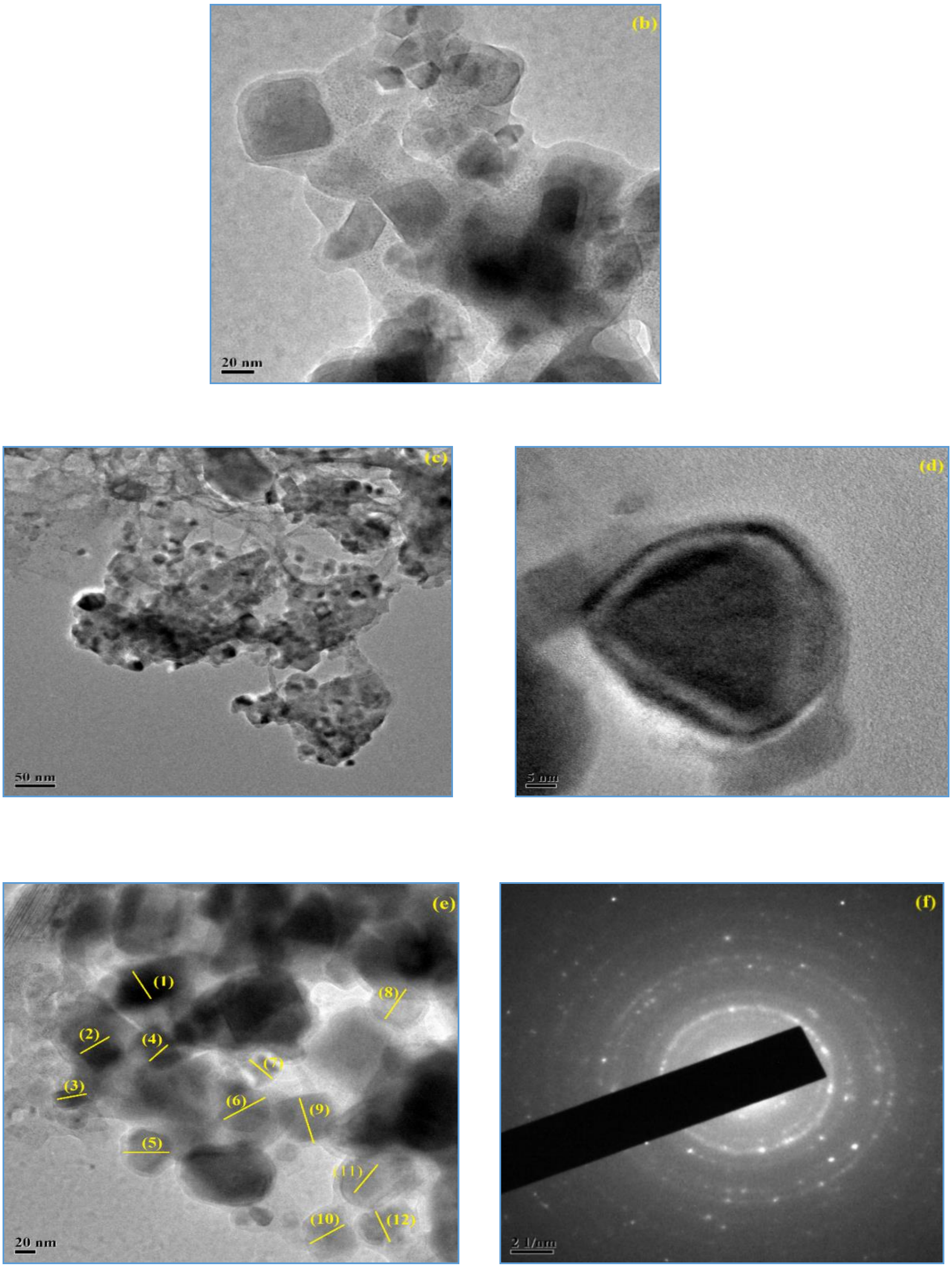

Fig.6.5. (a), (b), (c), (d) FETEM IMAGE OF $Ni_{1-x}Co_xFe_2O_4$ ($x = 0.5$) NANOPARTICLES CALCINATED AT 600 °C WITH DIFFERENT MAGNIFICATIONS also (e) PARTICLE SIZE USING IMAGE J VIEWER SOFTWARE AND (f) CORRESPONDING SAED PATTERN

The particles are nano sized and it is in cubic shape denoted in FESEM is confirmed from FETEM micrograph. SAED pattern shown in Fig.6.5 (f) confirmed that the synthesized $Ni_{1-x}Co_xFe_2O_4$(x = 0.5) nanoparticles are well crystalline nature. From "Image J viewer software" [Loganathan *et al.*, (2015)] it has been able to find the length of the individual selected particles which is shown in Fig.6.5 (e) and graph 3. From this software it is able to achieve the average particle size 31 nm which is closely satisfied with the XRD result.

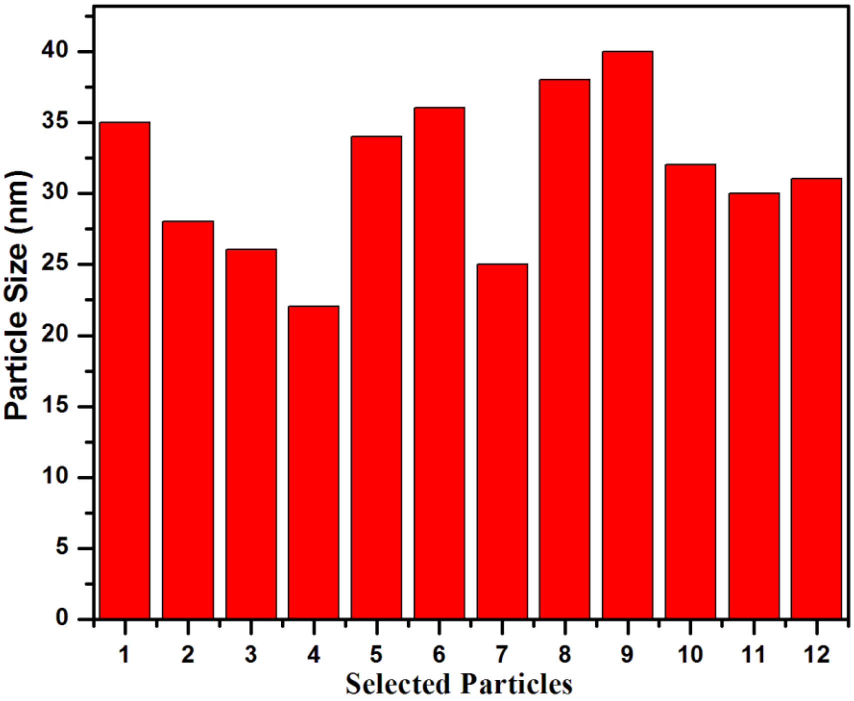

GRAPH 3: AVERAGE PARTICLE SIZE $Ni_{0.5}Co_{0.5}Fe_2O_4$ NANOPARTICLES USING IMAGE J VIEWER SOFTWARE FROM FETEM

6.2.6. CYCLIC VOLTAMMETRY (CV)

The cyclic voltammetry study for $Ni_{1-x}Co_xFe_2O_4$ (x = 0.3, 0.5, 0.7) calcinated at 600 °C electrode is carried out and it is recorded at different scan rates 2, 3, 5, 10, 20, 30, 50 and 100 mVs^{-1} is shown in Fig.6.6 (a) to (c).

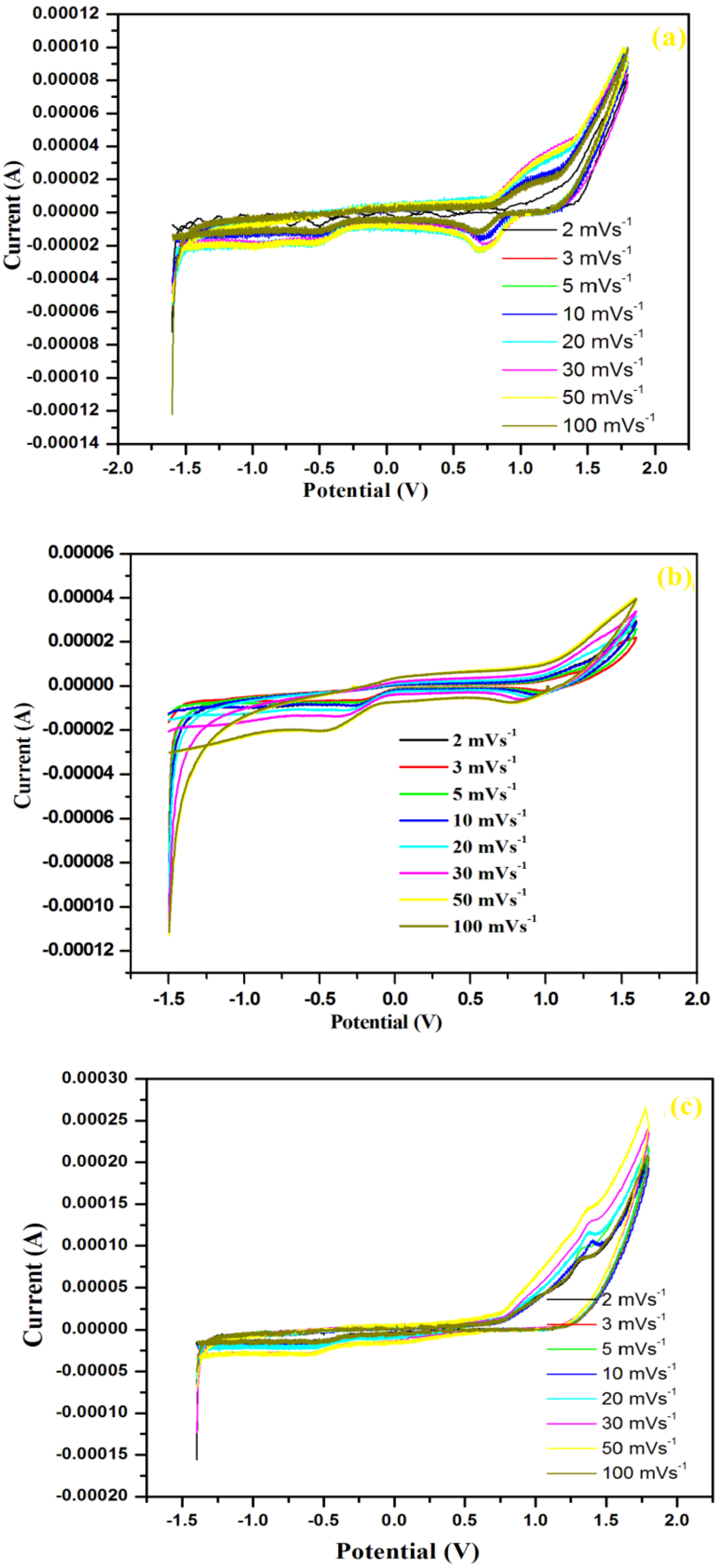

Fig. 6.6.CV PATTERN OF $Ni_{1-x}Co_xFe_2O_4$ (d), (e) AND (f) (x = 0.3, 0.5 AND 0.7 RESPECTIVELY) NANO PARTICLES CALCINATED AT 600 °C

Ideal rectangular shape is observed in the CV sure for 2 mVs^{-1}. The pseudo-capacitive nature is confirmed for the $Ni_{1-x}Co_xFe_2O_4$ (x = 0.3, 0.5, 0.7) nanoparticles calcinated at 600 °C as the CV pattern changes with increasing scan rate. The specific capacitances (SC) values of our desired synthesized material nickel cobalt ferrite electrode can be calculated using the relation [Sathishkumar *et al.*, (2015)].

$$Cs = \frac{Q}{\Delta v . m}$$

Whereas, Cs is the specific capacitance, Q signifies the anodic and cathodic charges on each scanning, m specifies the mass of the electrode material (mg) and Δv means the scan rate (mVs^{-1}) have been fixed in examining. Tetra butyl ammonium perchlorate 0.2 M with a standard three electrode configuration consisting of a sample (working electrode), an Ag/AgCl (reference electrode) and a high platinum wire (counter electrode) is taken during electrochemical measurements [Sathishkumar *et al.*, (2015)]. Different scan rate stating from 2 mVs^{-1} to 100 mVs^{-1} is done and their equivalent specific capacitance value decreased as the scan rate increases which is illustrated in Fig.6.7 (a) to (c) and table 10.

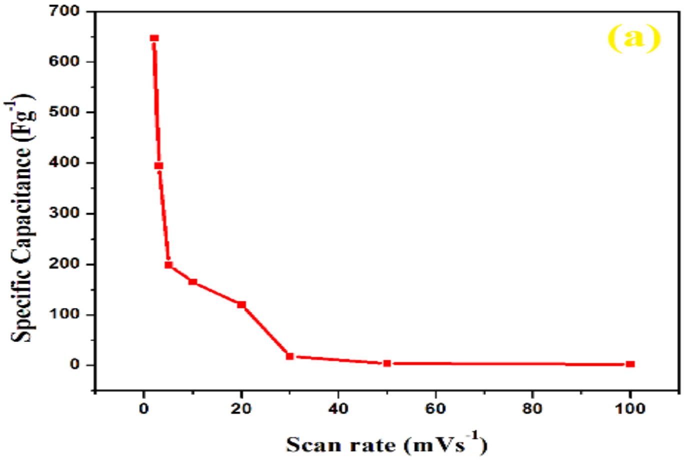

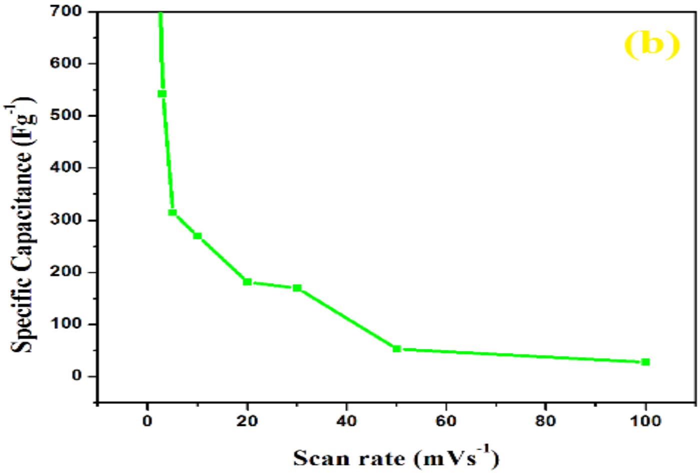

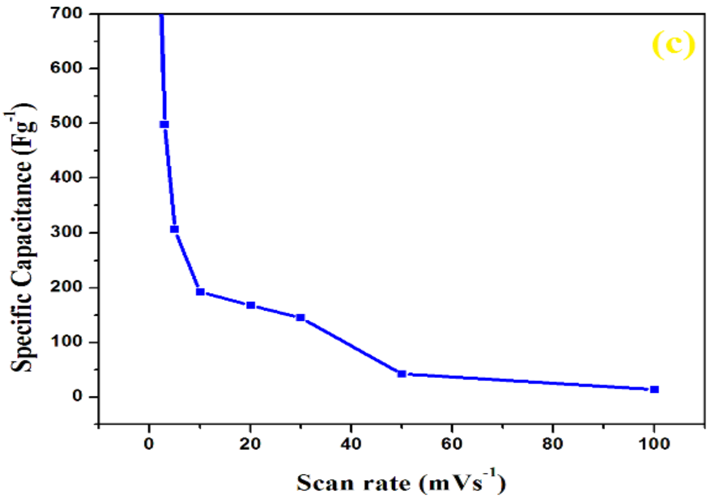

Fig. 6.7. (a-c) THE SPECIFIC CAPACITANCE OF THE $Ni_{1-x}Co_xFe_2O_4$ (x = 0.3, 0.5 and 0.7 RESPECTIVELY) NANOPARTICLES CALCINATED AT 600 °C VS DIFFERENT SCAN RATES

Table 10: THE SPECIFIC CAPACITANCE OF THE $Ni_{1-x}Co_xFe_2O_4$ (x = 0.3, 0.5 and 0.7 RESPECTIVELY) NANOPARTICLES CALCINATED AT 600 °C FOR DIFFERENT SCAN RATES

Different scan rate	**$Ni_{0.7}Co_{0.3}Fe_2O_4$ (600°C)**	**$Ni_{0.5}Co_{0.5}Fe_2O_4$ (600°C)**	**$Ni_{0.3}Co_{0.7}Fe_2O_4$ (600°C)**
2	782	865	812
3	435	543	464
5	262	314	305
10	175	270	258
20	137	182	165
30	119	170	130
50	27	53	32
100	12	28	24

A higher capacitance value of 865 Fg^{-1} is recorded for $Ni_{0.5}Co_{0.5}Fe_2O_4$ (calcinated at 600 °C) nanoparticles than $Ni_{1-x}Co_xFe_2O_4$ (x = 0.3 and 0.7) nanoparticles. The present study reveals that optimum temperature as

600 °C as well as the better concentration as x=0.5 by exhibiting higher specific capacitance. Higher specific capacitance value at low scan rate has been detected in the present study i.e., 2 mVs^{-1} propose that the ionic diffusion takes place in, both inner and outer surfaces depict lower specific capacitance values detected for higher scan rates specify that the ionic diffusion takes place only for outer surfaces [SuhCem Pang *et al.*, (2011)]. The greater specific capacitance value detected in the present study confirms the better crystallinity of the $Ni_{0.5}Co_{0.5}Fe_2O_4$ nano particles. Bhujun *et al.*, (2016) have reported a maximum specific capacitance of 221 Fg^{-1} at 5 mVs^{-1} scan rate for the sample $Ni_{0.5}Co_{0.5}Fe_2O_4$having particle size 17 nm. This shows the specific capacitance obtained in the present study is higher than the previously reported one and it helps to attain a better super capacitor.

6.2.7. **DYNAMIC LIGHT SCATTERING (DLS) AND ZETA POTENTIAL**

Particle size can be determined by measuring the random variations in the intensity of light scattered from a suspension or solution. This technique is usually known as dynamic light scattering (DLS), but is also called photon correlation spectroscopy (PCS) and quasi-elastic light scattering (QELS). Dynamic light scattering (DLS) it is based on the laser diffraction technique having several scattering method measures the hydro-dynamic diameter of the colloidal nanoparticles [Bojana mojic *et al.*, (2012)]. Size distribution of the $Ni_{0.5}Co_{0.5}Fe_2O_4$nanoparticles calcinated at 600 °C of pH 8 is exposed in Fig.6.8 (a). The Z-average is calculated by using DLS zeta analyser as 554.7 nm. This larger size is owing to insolubility and aggregation of the sample in water while examining.

Fig.6.8 (b) illustrates the zeta potential of $Ni_{0.5}Co_{0.5}Fe_2O_4$ nanoparticles calcinated at 600 °C. The stability of the $Ni_{0.5}Co_{0.5}Fe_2O_4$ nanoparticles is found out by using a Zeta potentiometer. The magnitude of the zeta potential delivers a symptom of the potential stability and surface charge of the synthesized nickel cobalt ferrite nanoparticles. The results of zeta potential and zeta deviation are -36.8 mV and 7.65 mV respectively and they reveal the good stability of synthesized $Ni_{0.5}Co_{0.5}Fe_2O_4$ nanoparticles.

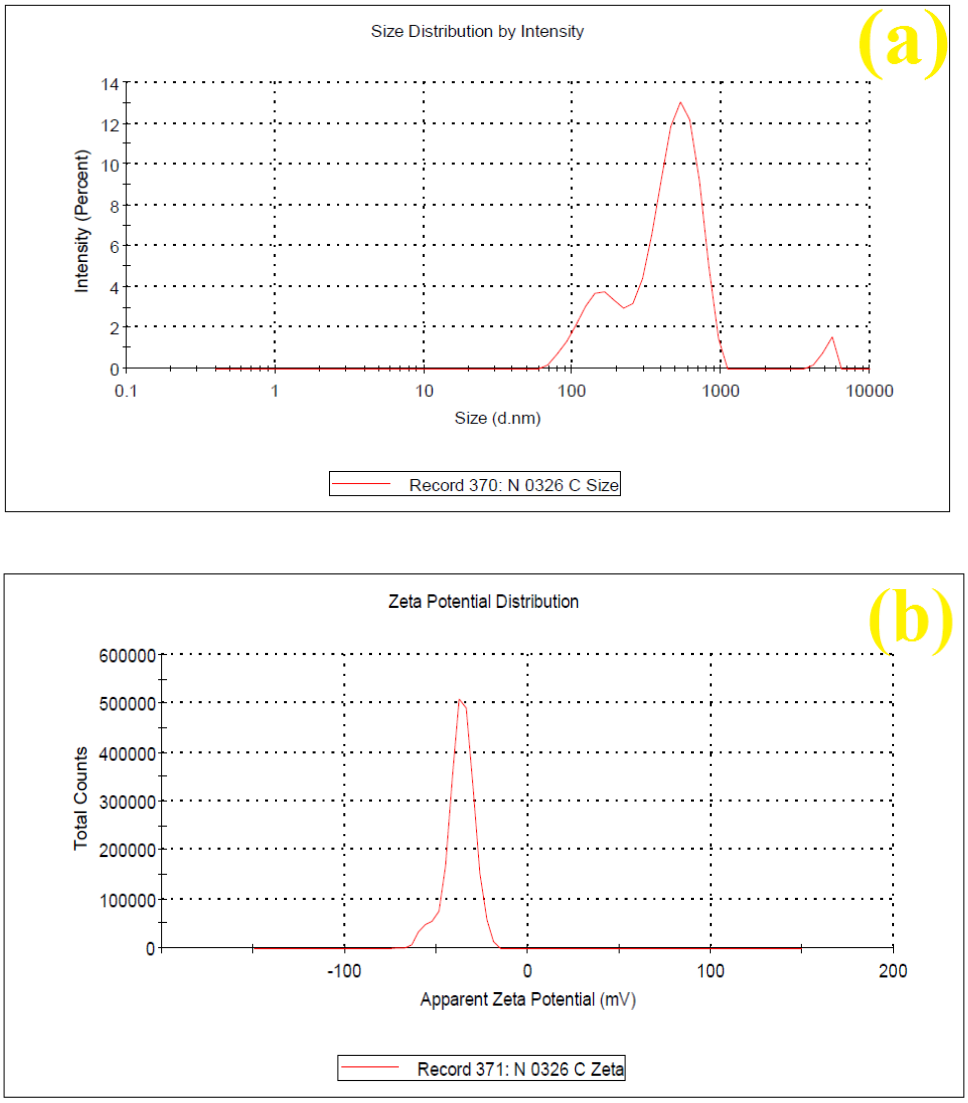

Fig. 6.8. ZETA SIZER AND ZETA POTENTIAL (a),(b) of $Ni_{0.5}Co_{0.5}Fe_2O_4$ NANO PARTICLES CALCINATED AT 600 °C

6.2.8. X-RAY PHOTOELECTRON SPECTROSCOPY (XPS)

X-ray photoelectron spectroscopy (XPS) was helps to identify the oxidation states. In transition metal compounds usually there exist multiple oxidation states simultaneously [Joshi *et al.*, (2016)]. Consequently, the corresponding XPS peaks are used to find the relative contribution of distinct oxidation state. Fig. 6.9(a) shows the Fe2p peak centred on 708.8 eV corresponds to Fe^{2+}.

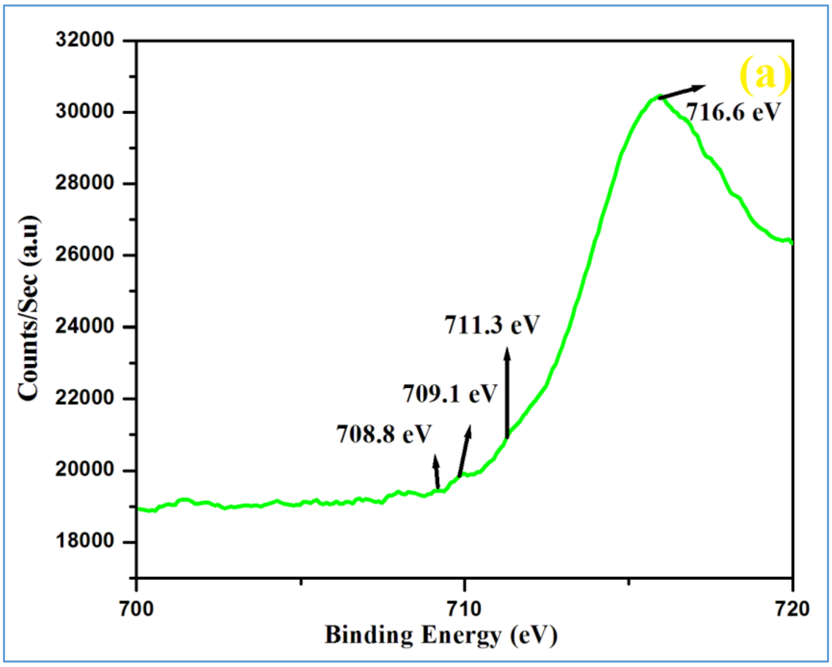

Fig. 6.9. (a) XPS SPECTRA OF FE FOR $Ni_{1-x}Co_xFe_2O_4$ (x = 0.5) NANO PARTICLES CALCINATED AT 600 °C

The peak around 709.1 and 711.3 eV are allotted to Fe^{3+} at octahedral and tetrahedral sites respectively. In addition a satellite peak noticeable at a binding energy of around 716.6 eV [Corneille *et al.*, (1995)]. Fig. 6.9(b) illustrates the XPS spectra for Ni 2p region of nickel incorporated cobalt ferrite.

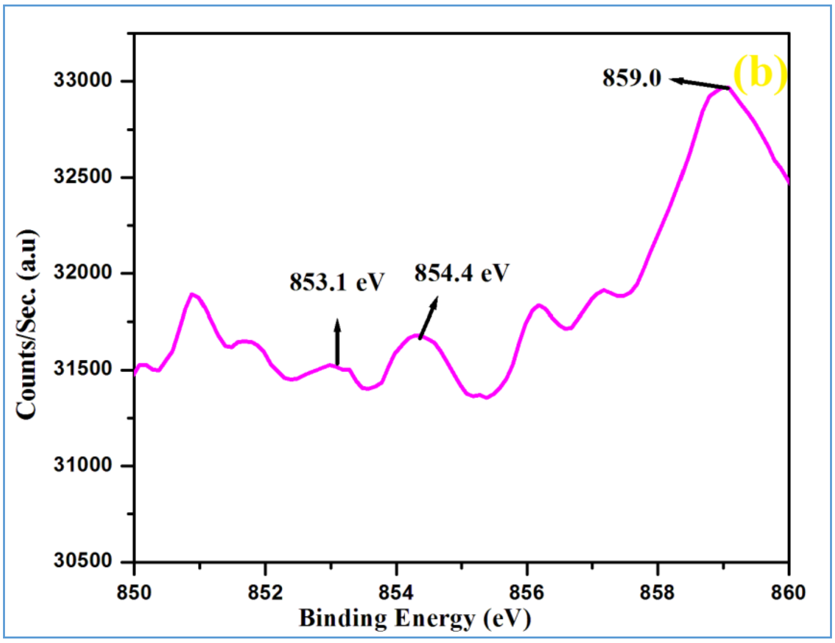

Fig. 6.9. (b) XPS SPECTRA OF NI FOR $Ni_{1-x}Co_xFe_2O_4$ (x = 0.5) NANOPARTICLES CALCINATED AT 600 °C

The spectra of both samples contain a foremost binding energy peak at 853.1 eV and a shoulder at 854.4 eV assigned to Ni^{2+} and Ni^{3+} respectively. Also a satellite peak was attained around 859.0 eV [Joshi *et al.*, (2016)]. The XPS spectra of the sample have peaks around 778.1 eV and 779.3 eV corresponding to Co^{2+} at octahedral and tetrahedral sites. A shoulder around 781.7 eV which is allotted to Co^{3+} and a satellite peak has been noticed around 785.1 eV which is shown in Fig.6.9(c) [Tudorachea *et al.*, (2013)].

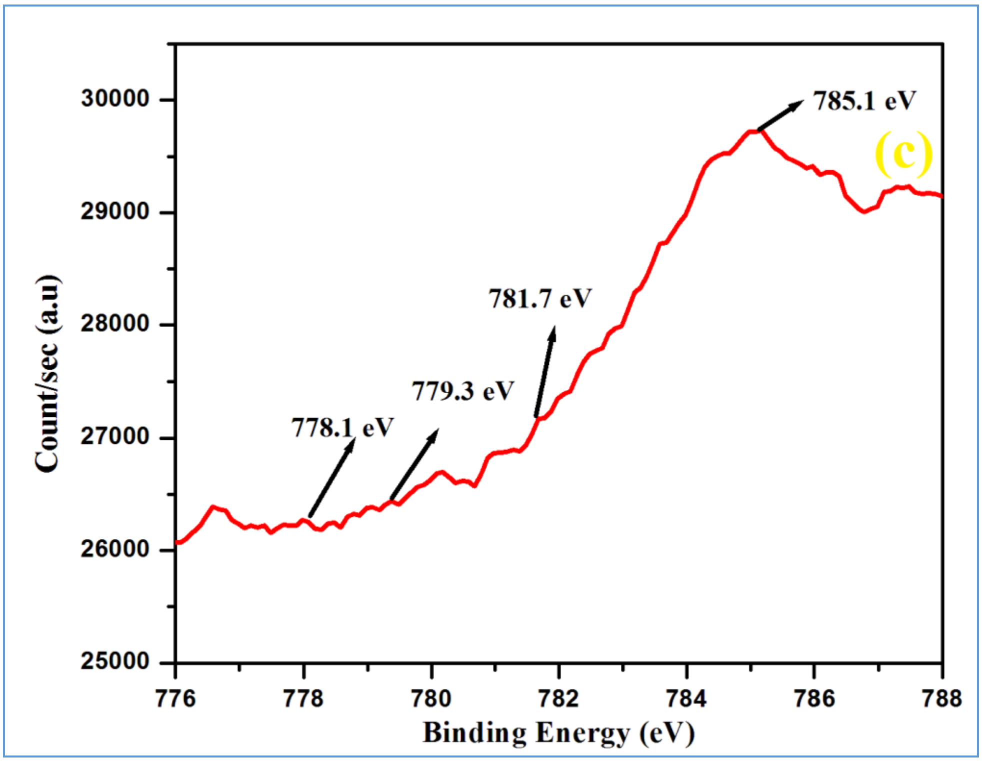

Fig. 6.9. (c) XPS SPECTRA OF CO FOR $Ni_{1-x}Co_xFe_2O_4$ (x = 0.5) NANOPARTICLES CALCINATED AT 600 °C

The main O 1s peak centered at 528.9 eV, common for all samples, relates to O^{2-} anions in the $NiCoFe_2O_4$ spinel crystal lattice. The second contribution, centred at 531.2 eV could be recognised to under-coordinated lattice oxygen, proposing structural defects [Joshi *et al.*, (2016)] which is shown in Fig.6.9 (d).

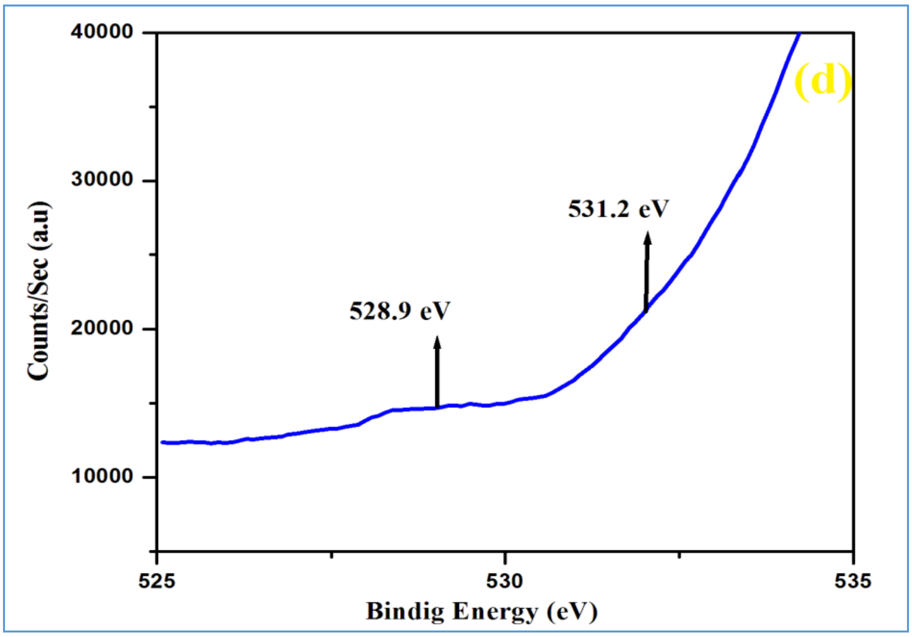

Fig. 6.9. (d) XPS SPECTRA OF O FOR $Ni_{1-x}Co_xFe_2O_4$ (x = 0.5) NANOPARTICLES CALCINATED AT 600 °C

From the XPS analysis it may conclude that the synthesized nickel cobalt ferrite nanoparticles have exist in multiple oxidation states.

6.3. CONCLUSION

Nickel Cobalt ferrite ($Ni_{1-x}Co_xFe_2O_4$; x = 0.3, 0.5, 0.7) were successfully synthesized and characterized by co-precipitation method with citrate as chelating agent further it was calcinated at different temperatures such as 400 °C, 600 °C and 800 °C. The synthesized sample was nanosized and well crystalline nickel cobalt ferrite nanoparticles were confirmed from XRD analysis. The functional groups present in the nickel cobalt ferrite nanoparticles was confirmed from the FTIR analysis. The mechanism of formation of $Ni_{1-x}Co_xFe_2O_4$ nanoparticles were found through TG/DTA analysis also the essential of calcination was confirmed from this analysis. Cubic shape of the synthesized nanoparticles was identified by using both morphological studies FESEM and FETEM. EDAX analysis exposed the elemental composition (Ni, Co and Fe) which was in appropriate proportion in the synthesized compound. Particle size was calculated from XRD using Debye Scherer formula which matches well with the particle size calculated from FETEM by using "image j viewer" software. Higher capacitance value of 865 Fg^{-1} $Ni_5Co_5Fe_2O_4$ (600 °C) at lower scanning rate of 2 mVs^{-1} gave a thorough idea regarding that the synthesized nanoparticles could be appropriate for super capacitance application. From the XPS analysis it may conclude that the synthesized $NiCoFe_2O_4$ nanoparticles have existed in multiple oxidation states. Superior stability of the synthesized nickel cobalt ferrite nanoparticles was confirmed from DLS zeta potential analysis.

CHAPTER –VII

SUMMARY AND CONCLUSION

In the last few decades, the new term with prefix nano have consumed sufficient space into the scientific vocabulary. The greater interest of the researchers in nano objects is owing to the unusual physical and chemical properties of these objects, which are strongly influenced by the crystalline shape and size. In these nanoparticles, transition based metal ferrite composites are attractive for a variety of devices viz, capacitors, memory devices, gas sensors and biomedical diagnosis. Nowadays energy crisis is the major problem to overcome this several research work has been done by various researchers. In this content the present work is focused on electrochemical supercapacitors. Electrochemical supercapacitors are having combination of high power density and high energy density, where it can be used as a harmonizing energy-storage device beside with the primary source such as battery or an efficient fuel cell, for power enhancement in short pulse applications. For commercial application the supercapacitors have to fulfil the following requirements: high specific capacitance, long cycle life and high charge-discharge rate. Transition metal doped ferrite, characterized by cheaper cost, abundance and eco-friendly nature, have been extensively evaluated as active electrode material for electrochemical supercapacitors. Although an enhanced capacitance could be achieved through transition metal ferrite based composites. In the present work a facile simple co-precipitation method has been proposed to synthesize a composite to enhance the electrochemical performance.

A composite of $NiFe_2O_4$ nano particles were synthesized by simple co-precipitation method. Thermo-gravimetric analysis confirms that pure $NiFe_2O_4$ will form above 362 °C only after the degradation of organic templates present in the sample. After calcination at respective temperatures, the synthesized $NiFe_2O_4$ nano particles were analyzed for structural and electrochemical behaviour. From the TG analysis no weight loss is found beyond 362°C indicating the formation of $NiFe_2O_4$ nanoparticles.Further the synthesized products were calcinated to 400 °C, 600 °C and 800 °C based on thermal analysis. The XRD analysis confirms the synthesized sample as $NiFe_2O_4$ nanoparticles are cubic spinel structure with Fd3m space group. The morphology of $NiFe_2O_4$ nano particles calcinated to 600 °C was analyzed by FESEM and confirmed by FETEM. The FETEM results of the product calcinated at 600 °C revealed the presence of cubic morphology. EDAX spectrum confirmed that the sample contains only Ni, Fe and O without any other impurities. The FTIR analysis revealed the synthesized sample as nickel ferrite. The higher zeta potential value indicated that the synthesized nickel ferrite nano particles have good stability. The XPS analysis confirmed that the synthesized $NiFe_2O_4$ nanoparticles have exist in multiple oxidation states. The electrochemical behaviours of the products were analyzed by cyclic voltammetry. From CV study, higher capacitance value of 421Fg^{-1} at scan rate of 2 mVs^{-1} was observed for $NiFe_2O_4$ nanoparticles calcinated at 600 °C suggested for super capacitor application.

Cobalt ferrite ($CoFe_2O_4$) nanoparticles was prepared by a facile novel co-precipitation method. Thermo-gravimetric analysis confirms that pure $CoFe_2O_4$ will form above 432 °C only after the degradation of organic templates present in the sample. The synthesized products were calcinated to 400 °C, 600 °C and 800 °C based on thermal analysis. From XRD analysis it is confirmed that the synthesized sample as $CoFe_2O_4$ nanoparticles. The cubic morphology of $CoFe_2O_4$ nano particles calcinated to 600 °C was analyzed by FESEM and it was confirmed by FETEM analysis. EDAX analysis confirmed that the sample contains only Co, Fe and O without any other impurities. The FTIR confirmed the synthesized sample as cobalt ferrite. The zeta potential value exposed that the synthesized cobalt ferrite nano particles have better stability. The XPS analysis confirmed that the synthesized $CoFe_2O_4$ nanoparticles have exist in multiple oxidation states. The electrochemical behaviours of the products were analyzed by cyclic voltammetry. From this study a higher capacitance value of 609 Fg^{-1} for $CoFe_2O_4$ nanoparticles calcinated at 600 °C is may be used for super capacitor application.

Finally, to improve the electrochemical performance some more extend an attempt has been done in preparing a composite involving nickel cobalt ferrite nanoparticles by co-precipitation method. Thermo-gravimetric analysis confirms that pure nickel cobalt ferrite will form above 455 °C only after the degradation of organic templates exist in the sample. Afterwards the synthesized products were calcinated to 400 °C, 600 °C and 800 °C based on thermal study XRD analysis confirms the formation of pure nickel cobalt ferrite nanocomposite. In XRD analysis the particle size involving two component systems such as nickel ferrite and cobalt ferrite when comparing them the cobalt ferrite shows increased particle size than that of nickel ferrite. Same trend is noticed while increasing the cobalt content in the three component system nickel cobalt ferrite. This is due to the increase in ionic radii of cobalt is higher than that of nickel. The cubic morphology of synthesized $Ni_{1-x}Co_xFe_2O_4$ nano particles calcinated to 600 °C was identified using FESEM and confirmed by FETEM. From EDAX study it confirmed that the synthesized sample only contains Ni, Co, Fe and O without any other impurities. The FTIR analysis confirmed the synthesized sample as nickel cobalt ferrite. The zeta potential value exposed that the synthesized nickel ferrite nano particles have good stability. The XPS analysis confirmed that the synthesized $NiCoFe_2O_4$ nano particles have exist in multiple oxidation states. The electrochemical behaviours of the products were analyzed by cyclic voltammetry. From CV study a higher capacitance value of 865 Fg^{-1} is recorded for $Ni_{0.5}Co_{0.5}Fe_2O_4$ nano particles which is greater than $Ni_{1-x}Co_xFe_2O_4$ (x = 0.3 and 0.7) nanoparticles.

The specific capacitance values are observed in the present study for 600 °C is of the order $NiFe_2O4 < CoFe_2O4 < Ni_{1-x}Co_xFe_2O_4$. From which a composite involving three component system shows higher capacitance than that of two component system. In addition the nickel cobalt ferrite composite having concentration $Ni_{0.5}Co_{0.5}Fe_2O_4$ depicts higher capacitance value than $Ni_{0.7}Co_{0.3}Fe_2O_4$ and $Nio.3Co_{0.7}Fe_2O_4$. Hence the three component composite having higher concentration $Ni_{0.5}Co_{0.5}Fe_2O_4$ is suitable for super capacitor application.

FUTURE PLAN

The methodology developed in the present study could be extended to other transition metals for making ferrite based nano composite to enhance their electrochemical performance.

REFRENCES

Abdul Gaffoor., Ravinder, D., "Characterization of Nano-structured Nickel-Cobalt Ferrites Synthesized By Citrate-Gel Auto Combustion Method", *Int. Journal of Engineering Research and Applications,* 4(4), 73-79, (2014).

Al-Hoshan, M.S., Singh, J.P., Al-Mayouf, A.M., Al-Suhybani, A.A., Shaddad, M.N., "Synthesis, physicochemical and electrochemical properties of nickel ferrite spinels obtained by hydrothermal method for the oxygen evolution reaction (OER)", *Int. J. Electrochem. Sci.,* **7**, 4959-4973, (2012).

Allaedini, G., Tasirin, S.M., Aminayi, P., "Magnetic properties of cobalt ferrite synthesized by hydrothermal method". *International Nano Letters*, **5(4)**, 183-186, (2015).

Almeida, T.P., Fay, M.W., Zhu, Y., Brown, P.D., "Hydrothermal synthesis of mixed cobalt-nickel ferrite nanoparticles". *InJournal of Physics: Conference Series, IOP Publishing,* **371 (1)**, 012-074, (2012).

Anju Ahlawat, V.G., Sathe, V.R., Reddy., Ajay Gupta., Mossbauer., Raman., "X-ray diffraction studies of superparamagnetic $NiFe_2O_4$ nanoparticles prepared by sol–gel auto-combustion method", *Journal of Magnetism and Magnetic Materials*, **323,** 2049–2054, (2011).

Anwar, S., Muthu, K.S., Ganesh, V., Lakshminarasimhan, N. A., "'Comparative study of electrochemical capacitive behavior of $NiFe_2O_4$ synthesized by different routes". *Journal of The Electrochemical Society*, **158(8)**, 976-981, (2011).

Ashiq, M.N., Iqbal, M.J., Gul, I.H., "Structural, magnetic and dielectric properties of Zr–Cd substituted strontium hexaferrite ($SrFe_{12}O_{19}$) nanoparticles", *Journal of Alloys and compounds,* **487(1),** 341-345, (2009).

Ati, A.A., Othaman, Z., Samavati, A., “Influence of cobalt on structural and magnetic properties of nickel ferrite nanoparticles”, *Journal of Molecular Structure,* **25**, 177-182, (2013).

Ati, M.A., Khudhair, H., Dabagh, S., Rosnan, R.M., Ati, A.A., “Synthesis and Characterization of Cobalt doped Nickel-Ferrites Nanocrystalline by Co-precipitation Method”, *International Journal of Scientific & Engineering Research,* **5(9)**, 2229-5518, (2014).

Backes, S., Witt, M.U., Roeben, E., Kuhrts, L., Aleed, S., Schmidt, A.M., von Klitzing, R., “Loading of PNIPAM Based Microgels with $CoFe_2O_4$ Nanoparticles and Their Magnetic Response in Bulk and at Surfaces”, *The Journal of Physical Chemistry B,* **119(36),** 12129-37, (2015).

BaijuVidhyadharan.,NurulKhayyriahMohdZain.,IzanIzwanMisnon., RadhiyahAbd Aziz., Jamil Ismail., Mashitah, M., Yusoff., Rajan Jose., “High performance supercapacitor electrodes from electrospun nickel oxide nanowires”, *Journal of Alloys and Compounds*, **610,** 143–150, (2014).

Bhosale, S.V., Kanhe, N.S., Bhoraskar, S.V., Bhat, S.K., Bulakhe, R.N., Shim, J.J., Mathe, V.L., “Micro-structural analysis of $NiFe_2O_4$ nanoparticles synthesized by thermal plasma route and its suitability for BSA adsorption”, *Journal of Materials Science: Materials in Medicine,* **26(8)**, 1-5, (2015).

Bhujun, B., Tan, M.T., Shanmugam, A.S., “Study of mixed ternary transition metal ferrites as potential electrodes for supercapacitor applications”, *Results in Physics*, (2016).

Biesinger, M.C., Payne, B.P., Lau, L.W., Gerson, A., Smart, R.S., “X-ray photoelectron spectroscopic chemical state quantification of mixed nickel metal, oxide and hydroxide systems”, *Surface and Interface Analysis,* **41(4)**, 324-332, (2009).

Bojana Mojic., Konstantinos, P., Giannakopoulos., Zeljka Cvejic., Vladimir, V., Srdic., "Silica coated ferrite nanoparticles: Influence of citrate functionalization procedure on final particle morphology", *Ceramics International,* **38** 6635–6641, (2012).

Byung-Keunoh., Sungho Park., Jill, E., Millstone., Seung Woo Lee., Ki-Bum Lee., Chad, A., Mirkin., "Separation of Tricomponent Protein Mixtures with TriblockNanorods", *J. Am. Chem. Soc.,* **128(36),** 11825–11829, (2006).

Cannas, C., Musinu, A., Ardu, A., Orru, F., Peddis, D., Casu, M., Sanna, R., Angius, F., Diaz, G., Piccaluga, G., "$CoFe_2O_4$ and $CoFe_2O_4/SiO_2$ core/shell nanoparticles: magnetic and spectroscopic study", *Chemistry of Materials,* **22(11)**, 3353-3361, (2010).

Carley, A.F., Rassias, S., Roberts, M.W., "The specificity of surface oxygen in the activation of adsorbed water at metal surfaces", *Surface science*, **135(1)**, 35-51, (1983).

Ceden o-Mattei, Y., Perales-Perez, O., Tomar, M.S., Roman, F., Voyles, P.M., Stratton, W.G., "Tuning of magnetic properties In cobalt ferrite nanocrystals", *Journal of Applied Physics,* **103(7)**, 7E512, (2008).

Chandramohan, P., Srinivasan, M.P., Velmurugan, S., Narasimhan, S.V., "Cation distribution and particle size effect on Raman spectrum of $CoFe_2O_4$", *Journal of Solid State Chemistry*, **184(1)**, 89-96, (2011).

Chen, D., Wang, Q., Wang, R., Shen, G., "Ternary oxide nanostructured materials for supercapacitors: a review", *Journal of Materials Chemistry,* **3 (19)**, 10158-10173, (2015).

Chen, L., Dai, H., Shen, Y., Bai, J., "Size-controlled synthesis and magnetic properties of $NiFe_2O_4$ hollow nanospheres via a gel-assistant hydrothermal route", *Journal of Alloys and Compounds,* **491(1),** 33-38, (2010).

Cojocariu Alina Mihaela., Soroceanu Marius., Hrib Luminita., Nica Valentin., Caltun Ovidiu Florin., “Microstructure and magnetic properties of substituted (Cr, Mn) - cobalt ferrite nanoparticles”, *Materials Chemistry and Physics*, **135** (2012).

Conway, B.E., “Electrochemical Supercapacitors-Scientific Fundamentals and Technological Applications”, *Plenum Press. New York,* (1999).

Cordente, N., Respaud, M., Senocq, F., Casanove, M.J., Amiens, C., Chaudret, B., “Synthesis and magnetic properties of nickel nanorods”, *Nano letters*, **1(10)**, 565-568, (2001).

Corneille, J.S., He, J.W., Goodman, D.W., “Preparation and characterization of ultra-thin iron oxide films on a Mo (100) surface”, *Surface science,* **338(1)**, 211-224, (1995).

Cullity, B.D., Elements of X-ray Diffraction, *Wesely, USA*, 284 (1978)., De Vicente, J., Delgado, A.V., Plaza, R.C., Duran, J.D., González-Caballero, F., “Stability of cobalt ferrite colloidal particles. Effect of pH and applied magnetic fields”, *Langmuir*, **16(21)**, 7954-7961, (2000).

Deng, D.H., Pang, H., Du, J. M., Deng, J. W., Li, S. J., Chen, J., Zhang, J. S., “Fabrication of cobalt ferrite nanostructures and comparison oftheir electrochemical properties”, *Cryst. Res. Technol.*, 1–7 (2012).

Derakhshi, P., Khorrami, S.A., Lotfi, R., “An investigation on ynthesis and morphology of nickel doped cobalt ferrite in presence of surfactant at different calcinations temperature by co-precipitation route”, *World Appl. Sci. J.*, **16**, 156-159, (2012).

Deraz N.M., Omar H. Abd-Elkader., “Processing and characterization of nano-magnetic $Co_{0.5}Ni_{0.5}Fe_2O_4$ system”, *Journal of Industrial and Engineering Chemistry,* **20**, 3251-3255, (2014) Deschanvres, J.L., Langlet, M., Joubert, J.C., “New spray pyrolysis deposition and magnetic properties of ferrite thin films for microwave applications”, *Journal of Magnetism and Magnetic Materials*, **83(1–3)**,437-438, (1990).

Dominguez-CrespoMiguel Antonio., Ramírez-Meneses, E., Montiel-Palma, V., Torres Huerta, A.M., Dorantes Rosales, H., “Synthesis and electrochemical characterization of stabilized nickel nanoparticles”, *International Journal of Hydrogen Energy*, **34(4),** 1664–1676, (2009).

El-Okr, M.M., Salem, M.A., Salim, M.S., El-Okr, R.M., Ashoush, M., Talaat, H,M., “Synthesis of cobalt ferrite nano-particles and their magnetic characterization”, *Journal of Magnetism and Magnetic Materials*, **323(7)**, 920-926, (2011).

Fan, H.M., Yi, J.B., Yang, Y., Kho, K.W., Tan, H.R., Shen, Z.X., Ding, J., Sun, X.W., Olivo, M.C., Feng, Y.P., “Single-crystalline MFe_2O_4 nanotubes/nanorings synthesized by thermal transformation process for biological applications”, *Acs Nano*, **3(9)**, 2798-2808, (2009).

Fang, J., Shama, N., Tung, L.D., Shin, E.Y., OConnor, C.J., Stokes, K.L., Caruntu, G., Wiley, J.B., Spinu, L., Tang, J., “Ultrafine $NiFe_2O_4$ powder fabricated from reverse microemulsion process” *Journal of Applied Physics*, **93(10)**, 7483, (2003).

Freitas, M.R., Gouveia, G.L., Dalla Costa, L.J., Oliveira, A.J., Kiminami, R.H., “Microwave Assisted Combustion Synthesis and Characterization of Nanocrystalline Nickel-doped Cobalt Ferrites”, *Materials Research*, (2016).

Gadkari, A.B., Shinde, T.J., Vasambekar, P.N., “Structural analysis of Y 3+-doped Mg–Cd ferrites prepared by oxalate co-precipitation method”, *Materials Chemistry and Physics*, **114(2)**, 505-510, (2009).

Gaikwad, R.S., Chae, S.Y., Mane, R.S,. Han, S.H., Joo, O.S., “Cobalt errite nanocrystallites for sustainable hydrogen production pplication”, *International Journal of Electrochemistry*, (2011).

Gama, L., Diniz, A.P., Costa, A.C.F.M., Rezende, S.M., Azevedo, A., ornejo D.R., "Magnetic properties of nanocrystalline Ni–Zn ferrites doped with samarium", *Physica B: Condensed Matter*, **384(1–2)**, 97–99, (2006).

Gandhi, N., Singh, K., Ohlan, A., Singh, D.P., Dhawan, S.K., "Thermal, dielectric and microwave absorption properties of polyaniline–$CoFe_2O_4$ nanocomposites", *Composites Science and Technology*, **71(15)**, 1754-1760, (2011).

Gatelytė, A., Jasaitis, D., Beganskienė, A., Kareiva, A., "Sol-gel synthesis and characterization of selected transition metal nano-ferrites", *Materials Science*, **17(3)**, 302-307, (2011).

Geim, A.K., "Graphene: status and prospects", *Science*, **324(5934)**, 1530-1534, (2009).

Gharagozlou, M., "Influence of calcination temperature on structural and magnetic properties of nanocomposites formed by Co-ferrite dispersed in sol-gel silica matrix using tetrakis (2-hydroxyethyl) orthosilicate as precursor", *Chemistry Central Journal,* **5(1)**, 1, (2011).

Gleick, P.H., "Dirty-water: Estimated Deaths from Water-related Diseases 2000-2020", *Oakland: Pacific Institute for Studies in Development, Environment, and Security*, (2002).

Gleiter, H., "Nanostructured materials: state of the art and perspectives", *Nanostructured Materials*, **6(1–4)**, 3-14, (1995).

Godman, A., "The magnetic applications choice among ferrite ceramics, metallic strips, or metal powder cores", *J. Mater. Eng.* **4,** 395–400, (1995).

Goldman, A., "Modern ferrite technology", *Springer Science & Business Media,* (2006).

Gonsalves, L.R., Verenkar, V.M., "Synthesis and characterization of nanosize nickel-doped cobalt ferrite obtained by precursor combustion method", *Journal of thermal analysis and calorimetry*, **108(3)**, 877-880, (2012).

Gopalakrishnan, R., Loganathan, B., Raghu, K., "Green synthesis of Au–Ag bimetallic nanocomposites using Silybum marianum seed extract and their application as a catalyst", *RSC Advances*, **5(40)**, 31691-31699, (2015).

Gotic, M., Czako-Nagy, I., Popovic, S., Music, S., "Formation of nanocrystalline $NiFe_2O_4$", *Philosophical magazine letters*, **78(3)**, 193-201, (1998).

Gu, Z., Xiang, X., Fan, G., Li, F., "Facile synthesis and characterization of cobalt ferrite nanocrystals via a simple reduction– oxidation route", *The Journal of Physical Chemistry C*, **112(47)**, 18459-18466, (2008).

Han, D.H., Luo, H.L., Yang, Z., "Remanent and anisotropic switching field distribution of platelike Ba-ferrite and acicular particulate recording media" *Journal of magnetism and magnetic materials*, **161**, 376-378 (1996).

Hankare, P.P., Sanadi, K.R., Garadkar, K.M., Patil, D.R., Mulla, I.S., "Synthesis and characterization of nickel substituted cobalt ferrite nanoparticles by sol–gel auto-combustion method", *Journal of Alloys and Compounds*, **553**, 383-388, (2013).

Hao, J., Yang, W., Zhang, Z., Lu, B., Zhang, B., Tang, J., "Facile Synthesis of 3D Hierarchical Flower-like Co_{3-x} Fe_xO_4 ferrite on Nickel Foam as High-Performance Electrodes for Supercapacitors", *Electrochimica Acta.*, **152**, 13-18, (2015).

Hessien, M.M., Zaki, Z.I., Mohsen, A.Q., "Low-Temperature Synthesis of Nanocrystalline $Mn_{0.2}$ $Ni_{0.8}$ Fe_2O_4 by Oxalate Precursor Route", (2013).

Houshiar, M., Zebhi, F., Razi, Z.J., Alidoust, A., Askari, Z., "Synthesis of cobalt ferrite ($CoFe_2O_4$) nanoparticles using combustion, coprecipitation, and precipitation methods: A comparison study of size, structural, and magnetic properties", *Journal of Magnetism and Magnetic Materials,* **371**, 43-48, (2014).

Huixia, F., Baiyi, C., Deyi, Z., Jianqiang, Z., Lin, T., "Preparation and characterization of the cobalt ferrite nano-particles by reverse coprecipitation", *Journal of Magnetism and Magnetic materials*, **356**, 68-72, (2014).

Huo, J., Wei, M., "Characterization and magnetic properties of nanocrystalline nickel ferrite synthesized by hydrothermal method", *Materials Letters*, **63(13)**, 1183-1184, (2009).

Israf Ud Din, Tasleem, S., Naeem, A., Maizatul S. Shaharun, Qazi Nasir., "Study of annealing conditions on particle size of nickel ferrite nanoparticles synthesized by wet chemical route" *Synthesis and Reactivity in Inorganic, Metal-Organic, and Nano-Metal Chemistry*," **46 (3),** 405-408, (2016).

Jackson, C.L., Mckenna, G.B., "The melting behavior of organic materials confined in porous solids", *The Journal of Chemical Physics,* **93(12)**, 9002-9011, (1990).

Jacob, J., Khadar, M.A., "Investigation of mixed spinel structure of nanostructured nickel ferrite", *Journal of applied physics*, **107(11)**, 114310, (2010).

Jacobo, S.E., Duhalde, S., Bertorello, H.R., "Rare earth influence on the structural and magnetic properties of NiZn ferrites", *J. Magn. Magn. Mater*, **2253,** 272–276, (2004).

Jagminas, A., Kurtinaitiene, M., Mazeika, K., "Synthesis of cobalt errite nanoparticles by co-precipi-tation at ambient and hydrothermal conditions", *Chemija*., **24(2)**, 103-110, (2013).

Janczak, C.M., Aspinwall, C.A., "Composite nanoparticles: the best of two worlds", *Analytical and bioanalytical chemistry*, **402(1)**, 83-90, (2012).

Jiang, J., Yang, Y.M., Li, L.C., "Surfactant-assisted synthesis of nanostructured $NiFe_2O_4$ via a refluxing route", *Materials Letters*, **62(12),** 1973-1975, (2008).

Joshi, S., Kumar, M., “Effect of Ni^{2+} substitution on structural, magnetic, dielectric and optical properties of mixed spinel $CoFe_2O_4$ nanoparticles”, *Ceramics International,* (2016).

Joshi, S., Kumar, M., “Influence of Co 2+ Substitution on Cation Distribution and on Different Properties of $NiFe_2O_4$ Nanoparticles”, *Journal of Superconductivity and Novel Magnetism*, **29(6)**, 1561-1572, (2016).

Joshi, S., Kumar, M., Chhoker, S., Srivastava, G., Jewariya, M., Singh, V.N., “Structural, magnetic, dielectric and optical properties of nickel ferrite nanoparticles synthesized by co-precipitation method”, *Journal of Molecular Structure,* **1076**, 55-62, (2014).

Jung, D.S., Kang, Y.C., “Effects of precursor types of Fe and Ni components on the properties of $NiFe_2O_4$ powders prepared by spray pyrolysis”, *Journal of magnetism and magnetic materials*, **321(6)**, 619-623, (2009).

Kale, A., Gubbala, S., Misra, R.D., “Magnetic behavior of nanocrystalline nickel ferrite synthesized by the reverse micelle technique”, *Journal of Magnetism and Magnetic Materials*, **277(3)**, 350-358, (2004).

Kambale, R.C., Shaikh, P.A., Kamble, S.S., Kolekar, Y.D., “Effect of cobalt substitution on structural, magnetic and electric properties of nickel ferrite”, *Journal of Alloys and Compounds*, **478(1)**, 599-603, (2009).

Kambale, R.C., Song, K.M., Koo, Y.S., Hur, N., “Low temperature synthesis of nanocrystalline Dy3+ doped cobalt ferrite: structural and magnetic properties”, *Journal of Applied Physics*, **110(5)**, 053910, (2011).

Karakas, Z.K., Boncukcuoglu, R., Karakas, H., Ertugrul, M., “The effects of heat treatment on the synthesis of nickel ferrite ($NiFe_2O_4$) nanoparticles using the microwave assisted combustion method”, *Journal of Magnetism and Magnetic Materials*, **374**, 298-306, (2015).

Khan, Z., Chetia, T.R., Qureshi, M., "Rational design of hyperbranched 3D heteroarrays of SrS/CdS: synthesis, characterization and evaluation of photocatalytic properties or efficient hydrogen generation and organic dye degradation", *Nanoscale*, **4(11)**, 3543-3550, (2012).

Khosravi, I., Eftekhar, M., "Characterization and evaluation catalytic efficiency of $NiFe_2O_4$ nano spinel in removal of reactive dye from aqueous solution", *Powder technology*, **250**, 147-153, (2013).

Kim, S.J., Kim, W.C., Kim, C.S., Lee, S.W., "Moessbauer studies of superexchange interactions in $NiFe_2O_4$", *Journal of the Korean physical society*, **36(6)**, 430-434, (2000).

Kim, Y.I., Kim, D., Lee, C.S., "Synthesis and characterization of C $CoFe_2O_4$ magnetic nanoparticles prepared by temperature-controlled coprecipitation method", *Physica. B: Condensed Matter*, **337(1)**, 42-51, (2003).

Kooti, M., Afshari, M., "Magnetic cobalt ferrite nanoparticles as an efficient catalyst for oxidation of alkenes", *Scientia Iranica*, **19(6),** 1991-1995, (2012).

Koseoglu, Y., Baykal, A., Gozuak, F., Kavas, H., "Structural and magnetic properties of $Co_xZn_{1-x}Fe_2O_4$ nanocrystals synthesized by microwave method", *Polyhedron*, **28(14),** 2887-2892, (2009).

Kotz, R., Carlen, M., "Principles and applications of electrochemical capacitors", *Electrochimica. acta.*, **45(15)**, 2483-2498, (2000).

Krieble, K., Schaeffer, T., Paulsen, J.A., Ring, A.P., Lo, C.C., "Snyder JE. Mössbauer spectroscopy investigation of Mn-substituted Co-ferrite ($CoMn_xFe_{2-x}O_4$)", *Journal of applied physics*, **97(10)**, 10F101, (2005).

Kumar, G., Chand, J., Verma, S., Singh, M., "Mixed Mg–Mn ferrites for high frequency applications processed by citrate precursor technique", *Journal of Physics D: Applied Physics*, **42(15)**, 155001, (2009).

Kumar, L., Kumar, P., Narayan, A., Kar, M., "Rietveld analysis of XRD patterns of different sizes of nanocrystalline cobalt ferrite", *International Nano Letters*, **3(1)**, 1-2, (2013).

Kumbhar, V.S., Jagadale, A.D., Shinde, N.M., Lokhande, C.D., "Chemical synthesis of spinel cobalt ferrite ($CoFe_2O_4$) nano-flakes for supercapacitor application", *Applied Surface Science*, **259**, 39-43, (2012).

Kurikka, V. P., Shafi, M., Aharon Gedanken., "Sonochemical Preparation and Size-Dependent Properties of Nanostructured $CoFe_2O_4$ Particles", *Chem. Mater,* **10**, 3445-3450, (1998).

Lao, Z.J., Konstantinov, K., Tournaire, Y., Ng, S.H., Wang, G.X., Liu, H.K., "Synthesis of vanadium pentoxide powders with enhanced surface-area for electrochemical capacitors", *Journal of power sources*, **162(2)**, 1451-1454, (2006).

Lavela, P., Tirado, J.L., "$CoFe_2O_4$and $NiFe_2O_4$synthesized by sol–gel procedures for their use as anode materials for Li ion batteries", *Journal of power sources*, **172(1)**, 379-387, (2007).

Lee, J.G., Park, J.Y., Kim, C.S., "Growth of ultra-fine cobalt ferrite particles by a sol–gel method and their magnetic properties", *Journal of Materials Science*, **33(15)**, 3965-3968, (1998).

Li, F.S., Wang, L., Wang, J.B., Zhou, Q.G., Zhou, X.Z., Kunkel, H.P., Williams, G., "Site preference of Fe in nanoparticles of $ZnFe_2O_4$", *Journal of Magnetism and Magnetic Materials*, **268(3)**, 332-339, (2004).

Li, X.H., Xu, C.L., Han, X.H., Qiao, L., Wang, T., Li, F.S., "Synthesis and magnetic properties of nearly monodisperse $CoFe_2O_4$ nanoparticles through a simple hydrothermal condition", *Nanoscale research letters*, **5(6)**, 1039, (2010).

Lifshitz, I.M., Slyozov, V.V., "The kinetics of precipitation from supersaturated solid solutions", *Journal of physics and chemistry of solids*, **19(1-2)**, 35-50, (1961).

Liu, B., Ding, J., Yi, J., Yin, J., Dong, Z., "Magnetic anisotropies in cobalt-nickel ferrites ($Ni_xCo_{1-x}Fe_2O_4$)", (2008).

Liu, E.H., Meng, X.Y., Ding, R., Zhou, J.C., Tan, S.T., "Potentiodynamical co-deposited manganese oxide/carbon composite for high capacitance electrochemical capacitors", *Materials Letters*, **61(16)**, 3486-3489, (2007).

Liu, H., Zhu, H., Yang, H., "A low temperature synthesis of nanocrystalline spinel $NiFe_2O_4$ and its electrochemical performance as anode of lithium-ion batteries", *Materials Research Bulletin*, **48(4)**, 1587-1592, (2013).

Liu, J., Essner, J., Li, J., "Hybrid supercapacitor based on coaxially coated manganese oxide on vertically aligned carbon nanofiber arrays", *Chemistry of Materials*, **22(17)**, 5022-5030, (2010).

Liu, X., Cheng, B., Hu, J., Qin, H., Jiang, M., "Semiconducting gas sensor for ethanol based on $LaMg_xFe_{1-x}O_3$ nanocrystals", *Sensors and Actuators B: Chemical,* **129(1)**53-58, (2008).

Liu, Z., Li, X., Leng, Y., Lian, J., Liu, S., Xiu, Z., Huo, D., Li, J,G., Sun, X., "Homogeneous precipitation synthesis and magnetic Properties of cobalt ferrite nanoparticles", *Journal of Nanomaterials*, **73,** (2008).

Loganathan, B., Chandraboss, V.L., Senthilvelan, S., Karthikeyan, B., "Surface enhanced vibrational spectroscopy and first-principles study of L-cysteine adsorption on noble trimetallic Au/Pt@ Rh clusters", *Physical Chemistry Chemical Physics*, **17(33)**, 21268-21277, (2015).

Lu, A.H., Salabas, E.E., Schüth, F., "Magnetic nanoparticles: synthesis, protection, functionalization, and application", *Angewandte Chemie. International Edition*, **46(8)**, 1222-1244, (2007).

Maaz, K., Karim, S., Mashiatullah, A., Liu, J., Hou, M.D., Sun, Y.M., Duan, J.L., Yao, H.J., Mo, D., Chen. Y.F., "Structural analysis of nickel doped cobalt ferrite nanoparticles prepared by coprecipitation route", *Physica B: Condensed Matter,* **404(21)**, 3947-3951, (2009).

Maaz, K., Karim, S., Mumtaz, A., Hasanain, S.K., Liu, J., Duan, J.L., "Synthesis and magnetic characterization of nickel ferrite nanoparticles prepared by co-precipitation route", *Journal of Magnetism and Magnetic Materials*, **321(12),** 1838-1842, (2009).

Maaz, K., Khalid, W., Mumtaz, A., Hasanain, S.K., Liu, J., Duan, J.L., "Magnetic characterization of $Co_{1-x}Ni_xFe_2O_4$ ($0 \leqslant x \leqslant 1$) nanoparticles prepared by co-precipitation route", *Physica E: Low-dimensional Systems and Nanostructures*, **41**(**4**), 593-599, (2009).

Mandlimath, T.R., Gopal, B., "Catalytic activity of first row transition metal oxides in the conversion of p-nitrophenol to P-aminophenol", *Journal of Molecular Catalysis A: Chemical*, **350**(**1**), 9-15, (2011).

Maqusood Ahamed., MohdJaved Akhtar., Maqsood, A., Siddiqui., Javed Ahmad., Javed Musarrat., Abdulaziz, A., Al-Khedhairy., Mohamad, S., AlSalhi., Salman, A., Alrokayan.*Toxicology*, **283(2–3),** 101–108, (2011).

Mathew, D.S., Juang, R.S., "An overview of the structure and magnetism of spinel ferrite nanoparticles and their synthesis in microemulsions", *Chemical Engineering Journal*, **129(1)**, 51-65, (2007).

McIntyre, N.S., Zetaruk, D.G., "X-ray photoelectron spectroscopic tudies of iron oxides", *Analytical Chemistry*, **49(11)**, 1521-1529, (1977).

Melagiriyappa, E., Jayanna, H.S., "Structural and magnetic susceptibility studies of samarium substituted magnesium–zinc ferrites", *J. Alloys and Comps*, **482(1–2)**, 147–150, (2009).

Mishra, S., Karak, N., Kundu, T.K., Das, D., Maity, N., Chakravorty, D., "Nanocrystalline nickel ferrites prepared by doping with niobium ions", *Materials Letters*, **60(9)**, 1111-1115, (2006).

Mohapatra, S., Rout, S.R., Maiti, S., Maiti, T.K., Panda, A.B., "Monodisperse mesoporous cobalt ferrite nanoparticles: synthesis and application in targeted delivery of antitumor drugs", *Journal of Materials Chemistry*, **21(25)**, 9185-9193, (2011).

Moumen, N., Pileni, M.P., "Control of the size of cobalt ferrite magnetic fluid", *The Journal of Physical Chemistry*, **100(5)**, 1867-1873, (1996).

Murdock, E.S., Simmons, R.F., "Davidson R. Roadmap for 10 Gbit/in 2 media: challenges", *IEEE transactions on magnetic*, **28(5)**, 3078-3083, (1992).

Nakagomi, F., Da Silva, S. W., Garg, V. K., Oliveir, A. C., Morais, C., "The influence of cobalt population on the structural Propertiesof $Co_xFe_{3-x}O_4$", *Journal Of Applied Physics*, **101**, (2007).

Nakamura, T., Miyamoto, T. Yamada, Y., "Complex permeability spectra of polycrystalline Li–Zn ferrite and application to EM-wave absorber", *Journal of Magnetism and Magnetic Materials*, **256(1–3)**, 340–347, (2003).

Naveen, A.N., Selladurai, S., "Novel synthesis of highly porous three-dimensional nickel cobaltite for supercapacitor application", *Ionics.*,1-3, (2016).

Nejati, K., Zabihi, R., "Preparation and magnetic properties of nano size nickel ferrite particles using hydrothermal method", *Chemistry Central Journal*, **6(1)**, (2012).

Nermin Kasapoglu., Abdulhadi Baykal., Muhammet Toprak., Yuksel Koseoglu., Harun Bayrakdar., "Synthesis and Characterization of $NiFe_2O_4$Nano-Octahedrons by EDTA-Assisted Hydrothermal Method", *Turk J. Chem.* **31**, 659 – 666, (2007).

Nikolic, A.S., Jovic, N., Rogan, J., Kremenovic, A., Ristic, M., Meden, A., Antic, B., "Carboxylic acids and polyethylene glycol assisted synthesis of nanocrystalline nickel ferrites", *Ceramics International*, **39(6)**, 6681-6688, (2013).

Novoselova, L.Y., "Structure and properties of composite nanomaterials: Products of the thermal treatment of molybdenum-and iron-containing powders", *Russian Journal of Physical Chemistry A*, **86(11)**, 1689-1696, (2012).

Nowak Paweł., Laajalehto Kari., "On the interpretation of the xps spectraof adsorbed layers of flotation collectors – ethyl xanthate on metalliclead", *Physicochemical Problems of Mineral Processing*, **41**, 107-116, (2007).

Palaniappan, M., Gleick, P.H., "Peak water. Worlds Water", *The World's Water*, **6**:1-5, (2009).

Pan, W., Ma, Z., Liu, J., Liu, Q., Wang, J., "Effect of heating rate on morphology and structure of $CoFe_2O_4$ nanofibers", *Materials Letters*, **65(21)**, 3269-3271, (2011).

Pandey, B.K., Shahi, A.K., Swarnkar, R.K., Gopal, R., "Magnetic Property of novel cobalt sulfate nanoparticles synthesized by pulsed laser ablation", *Science of Advanced Materials*, **4(3-4)**, 537-543, (2012).

Pang, S.C., Wee, B.H., Chin, S.F., "The capacitive behaviors of manganese dioxide thin-film electrochemical capacitor prototypes", *International Journal of Electrochemistry*, (2011).

Papis, E., Rossi, F., Raspanti, M., Dalle-Donne, I., Colombo, G., Milzani, A., Bernardini, G., Gornati, R., "Engineered cobalt oxide nanoparticles readily enter cells”, *Toxicology l letters*, **189(3)**, 253-259, (2009).

Patrusheva, T.N., Podorojnyak, S.A., Polyakova, K.P., Kirik, S.D., Menshikov, V.V., Levchenko, S.I., Patrushev, V.V., Adrianova, M.A., Gerasimova, G.E., “Manufacturing Solution for Producing Cobalt-ferriteFilms. *Chemical and Materials Engineering*, **2(2)**, 33-36, 2014.

Patrusheva, T.N., Podorojnyak, S.A., Polyakova, K.P., Kirik, S.D., Menshikov, V.V., Levchenko, S.I., Patrushev, V.V., Adrianova, M.A., Gerasimova, G.E., “Manufacturing Solution for Producing Cobalt-ferrite Films”, *Chemical and Materials Engineering*, **2(2)**, 33-36, (2014).

Pauline, S., Amaliya, A.P., “Synthesis and characterization of highly monodispersive $CoFe_2o_4$ magnetic nanoparticles by hydrothermal chemical route”, *Archives of Applied Science Research*, **3(5)**, 213-223, (2011).

Pileni, M. P., “Magnetic Fluids: Fabrication, Magnetic Properties, and Organization of Nanocrystals”, *Advanced Functional Materials*, **11(5)**, 1616-3028(2001).

Pillai, V., Shah, D.O., “Synthesis of high-coercivity cobalt ferrite particles using water-in-oil microemulsions”, *Journal of Magnetism and Magnetic Materials*, **163(1)**, 243-248, (1996).

Prabhakaran, T., Hemalatha, J., “Chemical control on the size and roperties of nano $NiFe_2O_4$ synthesized by sol–gel utocombustion method”, *Ceramics International,* **40(2)**, 3315-324, (2014).

Pradhan, S.K., Bid, S., Gateshki, M., Petkov, V., “Microstructure characterization and cation distribution of nanocrystalline magnesium ferrite prepared by ball milling”, *Materials Chemistry and Physics*, **93(1)**, 224-230, (2005).

Prasad, K.R., Miura, N., “Electrochemically synthesized MnO^{2-} based mixed oxides for high performance redox supercapacitors", *Electrochemistry Communications*, **6(10)**, 1004-1008, (2004).

Prasad, S., Gajbhiye, N.S., "Magnetic studies of nanosized nickel ferrite particles synthesized by the citrate precursor technique", *Journal of Alloys and Compounds*, **265(1)**, 87-92, (1998).

Qin Runhua., Li Fengsheng., Jiang Wei., Chen Mingyue., "Synthesis and characterization of diethylenetriaminepentaacetic acid-chitosan-coated cobalt ferrite core/shell nanostructures", *Materials Chemistry and Physics*, **122,** 498–501, (2010).

Qu, Y., Yang, H., Yang, N., Fan, Y., Zhu, H., Zou, G., "The effect of reaction temperature on the particle size, structure and magnetic properties of coprecipitated $CoFe_2O_4$ nanoparticles", *Materials Letters*, **60(29)**, 3548-3552, (2006).

Raj, K., Moskowitz, B., Casciari, R., "Advances in ferrofluid echnology", *J. Magn. Magn. Mater*, **149(1–2)**, 174-180, (1995).

Ramankutty, C.G., Sugunan, S., "Surface properties and catalytic activity of ferrospinels of nickel, cobalt and copper, prepared by soft chemical methods", *Applied Catalysis A: General*, **218(1)**, 39-51, (2001).

Rao, C.N., Muller, A., Cheetham, A.K., "Nanomaterials chemistry: recent developments and new directions, John Wiley & Sons" (2007).

Rao, K.S., Choudary, G.S., Rao, K.H., Sujatha, C., "Structural and Magnetic Properties of Ultrafine $CoFe_2O_4$ Nanoparticles", *Procedia Materials Science*, **10**, 19-27, (2015).

Reddy, M.P., Madhuri, W., Sadhana, K., Kim, I.G,. Hui, K.N., Hui, K.S., Kumar, K.S., Reddy, R.R., "Microwave sintering of nickel ferrite nanoparticles processed via sol–gel method", *Journal of Sol-Gel Science and Technology*, **70(3)**, 400-404, (2014).

Rezlescu, N., Rezlescu, E., Tudorache, F., Popa, P.D., "MgCu nanocrystalline ceramic with La3+ and Y3+ ionic ubstitutions used as humidity sensor", *J. Opt. Adv. Mater*, 695-698, (2004).

Sajjia, M., Oubaha, M., Hasanuzzaman, M., Olabi, A.G., "Developments of cobalt ferrite nanoparticles prepared by the sol–gel process", *Ceramics International,* **40(1)**, 1147–1154, (2014).

Salavati-Niasari, M., Davar, F., Mahmoudi, T., "A simple route to synthesize nanocrystalline nickel ferrite ($NiFe_2O_4$) in the presence of octanoic acid as a surfactant", *Polyhedron*, **28(8)**, 1455-1458, (2009).

Salem, M.A., El-Okr, M.M., Salem, M.S., El-Okr, R.M., Ashoush, M., Talaat, H.M., "Synthesis of cobalt ferrite nano-particles and their magnetic characterization", *Journal of Magnetism and Magnetic Materials*, **323** 920–926, (2011).

Saliger, R., Fischer, U., Herta, C., Fricke, J., "High surface area carbon aerogels for supercapacitors", *Journal of Non-Crystalline Solids*, **225** 81-85, (1998).

Salunkhe, A.B., Khot, V.M., Phadatare, M.R., Pawar, S.H., "Combustion synthesis of cobalt ferrite nanoparticles—influence of fuel to oxidizer ratio", *Journal of alloys and compounds*, **514**, 91-96, (2012).

Sathishkumar, K., Shanmugam, N., Kannadasan, N., Cholan, S., Viruthagiri, G., "Opto, magnetic and electrochemical characterization of $Ni_{1-x}Co_xO$ nanocrystals", *Journal of Materials Science: Materials in Electronics*, **26(3)**, 1881-1889, (2015).

Sathitwitayakul, T., Kuznetsov, M.V., Parkin, I.P., Binions, R., "The gas sensing properties of some complex metal oxides prepared by self-propagating high-temperature synthesis", *Materials Letters,* **75**, 36-38, (2012).

Sen, P., De, A., "Electrochemical performances of poly (3, 4-ethylenedioxythiophene)–$NiFe_2O_4$ nanocomposite as electrode for supercapacitor", *Electrochimica Acta.*, **55(16)**, 4677-4684, (2010).

Senthilkumar, B., Selvan, R.K., Vinothbabu, P., Perelshtein, I., Gedanken, A., "Structural, magnetic, electrical and electrochemical properties of $NiFe_2O_4$ synthesized by the molten salt technique", *Materials Chemistry and Physics*, **130(1)**, 285-292, (2011).

Shafi, K.V.P.M., Gediankem,A., Prozorov, R., "Synthesis and magnetic behavior of silica-coated cobalt ferrite hollow spheres", *J. Balogh. Chem. Mater,* **10** 3445- 3450, (1998).

Shanmugavani, A., Kalpana, D., Selvan, R.K., "Electrochemical properties of $CoFe_2O_4$ nanoparticles as negative and $Co(OH)_2$ and $Co_2Fe(CN)_6$ as positive electrodes for supercapacitors", *Materials Research Bulletin,* **71**, 133-141, (2015).

Sharifi, I., Shokrollahi, H., Doroodmand, M.M., Safi, R., "Magnetic and structural studies on $CoFe_2O_4$ nanoparticles synthesized by co-precipitation, normal micelles and reverse micelles methods", *Journal of Magnetism and Magnetic Materials*.**324(10)**, 1854-1861, (2012).

Silva, J.B., De Brito, W., Mohallem, N.D., "Influence of heat treatment on cobalt ferrite ceramic powders", *Materials Science and Engineering: B*, **112(2)**, 182-187, (2004).

Singh, C., Goyal, A., Singhal, S., "Nickel-doped cobalt ferrite nanoparticles: efficient catalysts for the reduction of nitroaromatic compounds and photo-oxidative degradation of toxic dyes", *Nanoscale*, **6(14)**, 7959-7970, (2014).

Singhal, S., Singh, J., Barthwal, S.K., Chandra, K., "Preparation and characterization of nanosize nickel-substituted cobalt ferrites ($Co_{1-x}Ni_xFe_2O_4$)", *Journal of Solid State Chemistry,* **178(10)**, 3183-3189, (2005).

Sinko, K., Manek, E., Meiszterics, A., Havancsak, K., Vainio, U., Peterlik, H., "Liquid-phase syntheses of cobalt ferrite nanoparticles, *Journal of Nanoparticle Research*, **14(6)**, 1-4, (2012).

Smit, J., Wijn, H.P., "Ferrites (Philips Technical Library, Eindhoven)", *The Netherlands*, 139-142, (1959).

Sontu, U.B., Yelasani, V., Musugu, V.R., "Structural, electrical and magnetic characteristics of nickel substituted cobalt ferrite nano particles, synthesized by self combustion method", *Journal of Magnetism and Magnetic Materials*, **374**, 376-380, (2015).

Sousa, M.H., Hasmonay, E., Depeyrot, J., Tourinho, F.A., Bacri, J.C., Dubois, E., Perzynski, R., Raikher, Y.L., "$NiFe_2O_4$ nanoparticles in ferrofluids: evidence of spin disorder in the surface layer", *Journal of Magnetism and Magnetic Materials*, **242**, 572-574, (2002).

Spaldin, N.A., Fiebig, M., "The renaissance of magneto electricmultiferroics", *Science*, **309(5733)**, 391-392, (2005).

Srivastava, A.K., Patni, M.J., "Ferromagnetic resonance of gadolinium doped calcium vanadium garnets", *Journal of applied physics*, **81(4)**, 1863-1867, (1997).

Srivastava, M., Chaubey, S., Ojha, A.K., "Investigation on size dependent structural and magnetic behavior of nickel ferrite nanoparticles prepared by sol–gel and hydrothermal methods", *Materials Chemistry and Physics*, **118(1)**, 174-180, (2009).

Srivastava, M., Ojha, A.K., Chaubey, S., Materny, A., "Synthesis and optical characterization of nanocrystalline $NiFe_2O_4$ tructures", *Journal of Alloys and Compounds*, **481(1)**, 515-519, (2009).

Sugimoto, T., "Preparation of monodispersed colloidal particles", *Advances in Colloid and Interface Science*, **28**, 65-108, (1987).

Surendra, M.K., Kannan, D., Rao, M.R., "Magnetic and dielectric properties study of cobalt ferrite nanoparticles synthesized by co-precipitation method", *Cambridge University Press, InMRS proceedings* **1368,** 11-1368, (2011)

Tailhades, P.H., Villette, C., Rousset, A., Kulkarni, G.U., Kannan, K.R., Rao, C.N.R., Lenglet, M., "Cation Migration and Coercivity in Mixed Copper–Cobalt Spinel Ferrite Powders", *Journal of Solid State Chemistry*, **141(1)**, 56-63, (1998).

Tan, B.J., Klabunde, K,J., Sherwood, P.M., "XPS studies of solvated metal atom dispersed (SMAD) catalysts. Evidence for layered cobalt-manganese particles on alumina and silica", *Journal of the American Chemical Society*, **113(3)**, 855-861, (1991).

Tang, Y., Wang, X., Zhang, Q., Li, Y., Wang, H., "Solvothermal synthesis of $Co_{1-x}Ni_xFe_2O_4$ nanoparticles and its application in ammonia vapors detection", *Progress in Natural Science: Materials Internationa,*. **22(1),** 53-58, (2012).

Thakur, A., Mathur, P., Singh, M., "Study of dielectric behaviour of Mn–Zn nano ferrites", *Journal of Physics and Chemistry of solids,* **68(3)**, 378-381, (2007).

Thakur, S., Rai, R., Sharma, S., "Structural characterization and magnetic study of $NiFe_xO4$ synthesized by co-precipitation method", *Materials Letters*, **139**, 368-372, (2015).

Toksha, B.G., Shirsath, S.E., Patange, S.M., Jadhav, K.M., "Structural investigations and magnetic properties of cobalt ferrite nanoparticles prepared by sol–gel auto combustion method", *Solid State Communications*, **147(11)**, 479-483, (2008).

Toupin, M., Belanger, D., Hill, I.R., Quinn, D., "Performance of experimental carbon blacks in aqueous supercapacitors", *Journal of power sources*, **140(1)**, 203-210, (2005).

Tudorache, F., Popa, P.D., Dobromir, M., Iacomi, F., "Studies on the structure and gas sensing properties of nickel–cobalt ferrite thin films prepared by spin coating", *Materials Science and Engineering: B.* **178(19)**, 1334-1338, (2013).

Umare, S.S., Ningthoujam, R.S., Sharma, S.J., Shrivastava, S., Kurian, S., Gajbhiye, N.S., “Mossbauer and magnetic studies on nanocrystalline $NiFe_2O_4$ particles prepared by ethylene glycol route”, *Hyperfine Interactions*, **184(1-3)**, 235-243, (2008).

Velhal, N.B., Patil, N.D., Shelke, A.R., Deshpande, N.G., Puri, V.R., “Structural, dielectric and magnetic properties of nickel substituted cobalt ferrite nanoparticles”, *Effect of nickel concentration. AIP Advances*. **5(9)**, 097166, (2015).

Velhal, N.B., Patil, N.D., Shelke, A.R., Deshpande, N.G., Puri, V.R., “Structural, dielectric and magnetic properties of nickel substituted cobalt ferrite nanoparticles: Effect of nickel concentration”, *AIP Advances*, **5(9)**, 097166, (2015).

Velho-Pereira, S., Noronha, A., Mathias, A., Zakane, R., Naik, V., Naik, P., Salker, A.V., Naik, S.R., “Antibacterial action of doped $CoFe_2O_4$ nanocrystals on multidrug resistant bacterial strains”, *Materials Science and Engineering: C*, **52**, 282-287, (2015).

Verma, A., Goel, T.C., Mendiratta, R.G., Kishan, P., “Magnetic Properties of nickel–zinc ferrites prepared by the citrate Precursor method”, *Journal of Magnetism and Magnetic materials*, **208(1)**, 13-19, (2000).

Vijayakumar, S., Nagamuthu, S., Muralidharan, G., “Supercapacitor studies on NiO nanoflakes synthesized through a microwave route”, *ACS applied materials & interfaces*, **5(6)**, 2188-2196 (2013).

Wagner, C., “Theorie der alterung von niederschlägen durch umlösen (Ostwald-reifung)”, *Zeitschrift fur Elektrochemie, Berichte der Bunsengesellschaft für physikalische Chemie.* **65(7-8)**, 581-591, (1961).

Wang, H., Zhang, F., Zhang, W., Wang, X., Lu, Z., Qian, Z., Sui, Y., Dong, D., Su, W., “The effect of surface modification on the morphology and magnetic properties of $NiFe_2O_4$

nanoparticles", *Journal of crystal growth,* **293(1)**, 169-174, (2006).

Wang, J., Deng, T., Lin, Y., Yang, C., Zhan, W., "Synthesis and characterization of $CoFe_2O_4$ magnetic particles prepared by co-precipitation method: effect of mixture procedures of initial solution", *Journal of Alloys and Compounds,* **450(1)**, 532-539, (2008).

Wang, Y.C., Gunasekaran, S., "Spectroscopic and microscopic investigation of gold nanoparticle nucleation and growth mechanisms using gelatin as a stabilizer", *Journal of Nanoparticle Research*, **14(10),** 1-11, (2012).

Waqas, H., Qureshi, A. H., "Influence of pH on nanosized Mn–Zn ferrite synthesized by sol–gel auto combustion process", *J. Therm. Anal. Calorim.,* **98,** 355, (2009).

Warsi, M.F., Shakir, I., Shahid, M., Sarfraz, M., Nadeem, M., Gilani, Z.A., "Conformal coating of cobalt-nickel layered double hydroxides nanoflakes on carbon fibers for high-performance electrochemical energy storage supercapacitor devices", *Electrochimica Acta.*, **135,** 513-518, (2014).

Watawe, S.C., Ladgaonkar, B.P., "Chemical Synthesis and Functionalization of Cobalt Ferrite Nanoparticles with Oleic Acid and Citric Acid Encapsulation", *In MATEC Web of Conferences, EDP Sciences*, **30** (2015).

Willard, M.A., Kurihara, L.K., "Carpenter EE, Calvin S, Harris VG. Chemically prepared magnetic nanoparticles", *International Materials Reviews,* **49(3-4)**, 125-170, (2004).

Xiao, S.H., Jiang, W.F., Li, L.Y., Li, X.J., "Low-temperature auto-combustion synthesis and magnetic properties of cobalt ferrite nanopowder", *Materials Chemistry and Physics,* **106(1)**, 82-87, (2007).

Xing., Liu., Bin Cheng., Jifan Hu., Hongwei Qin., Minhua Jiang., "Semiconducting gas sensor for ethanol based on

$LaMg_xFe_{1-x}O_3$ nanocrystals.Sensors", *Actuat. B Chemical,* **129(1)**, 53–58, (2008).

Xu, C., Li, B., Du, H., Kang, F., Zeng, Y., "Electrochemical properties of nanosized hydrous manganese dioxide synthesized by a self-reacting microemulsion method" *Journal of Power Sources*, **180(1)**, 664-670, (2008).

Xu, Z., Shen, C., Tian, Y., Shi, X., Gao, H.J., "Organic phase synthesis of monodisperse iron oxide nanocrystals using iron chloride as precursor", *Nanoscale*, **2(6)**, 1027-1032, (2010).

Yan, H., Xie, X., Liu, K., Cao, H., Zhang, X., Luo, Y., "Facile preparation of Co_3O_4 nanoparticles via thermal decomposition of $Co(NO_3)_2$ loading on C_3N_4", *Powder Technology*, **221**, 199-202, (2012).

Yang, L., Xie, Y., Zhao, H., Wu, X., Wang, Y., "Preparation and gas-sensing properties of $NiFe_2O_4$ semiconductor materials", *Solid-state electronics*, **49(6)**, 1029-1033, (2005).

Yang, X., Wang, X., Zhang, Z., "Electrochemical properties of submicron cobalt ferrite spinel through a co-precipitation method", *Journal of crystal growth*, **277(1)**, 467-470, (2005).

Yu, Y., Mendoza-Garcia, A., Ning, B., Sun, S., "Cobalt-substituted magnetite nanoparticles and their assembly into ferrimagnetic nanoparticle arrays", *Advanced Materials,* **25(22),** 3090-3094, (2013).

Zaki, T., Saed, D., Aman, D., Younis, S.A., Moustafa, Y.M., "Synthesis and characterization of MFe_2O_4 sulfur nanoadsorbents", *Journal of sol-gel science and technology*, **65(2)**, 269-276, (2013).

Zhang Pan., lixinyong., Zhao Qidong., Liu Shaomin., "Synthesis and optical property of one-dimensional spinel $ZnMn_2O_4$nanorods", *Nanoscale Research Letters.* 316:323, (2011).

Zhang, D., Tong, Z., Xu, G., Li, S., Ma, J., “Templated fabrication of $NiFe_2O_4$ nanorods: characterization, magnetic and electrochemical properties”, *Solid State Sciences,* **11(1)**, 113-117, (2009).

Zhang, Q., Kang, J., Wang, Y., “Development of novel catalysts for Fischer–Tropsch synthesis: tuning the product selectivity”, *ChemCatChem.*, **2(9),** 1030-1058, (2010).

Zhang, Z., Liu, Y., Yao, G., Zu, G., Zhang, X., Ma. J., “Solid-state reaction synthesis of $NiFe_2O_4$ nanoparticles by optimizing the synthetic conditions”, *Physica E: Low-Dimensional Systems and Nanostructures*, **45**, 122-129, (2012).

Zhao, C., Li, J., Chen, W., Yang, Y., Chiang, K., Burke, N., “Synthesis and electrochemical properties of ordered mesoporous carbon supported well-dispersed cobalt oxide nanoparticles for supercapacitor”, *Materials Research Bulletin,* **64**, 55-60, (2015).

Zhao, H., Zheng, Z., Wong, K.W., Wang, S., Huang, B., Li, D., “Fabrication and electrochemical performance of nickel ferrite nanoparticles as anode material in lithium ion batteries”, *Electrochemistry Communications,* **9(10)**, 2606-2610, (2007).

Zhao, H., Zheng, Z., Wong, K.W., Wang, S., Huang, B., Li, D., “Fabrication and electrochemical performance of nickel ferrite nanoparticles as anode material in lithium ion batteries”, *Electrochemistry Communications*, **9(10),** 2606-2610, (2007).

Zhao, L., Cui, Y., Yang, H., Yu, L., Jin, W., Feng, S., “The magnetic properties of $Ni_{0.7}Mn_{0.3}\,Gd_x\,Fe_{2-x}O_4$ ferrite”, *Materials Letters,* **60(1)**, 104-108, (2006).

Cape Comorin Publisher
Kanyakumari, Tamilnadu, India
www.capecomorinpublisher.com

ISBN 978-93-88761-57-4